UNIVERSITAT POLITÈCNICA DE CATALUNYA
BARCELONATECH
Escola Superior d'Enginyeries Industrial,
Aeroespacial i Audiovisual de Terrassa

Institution

Escola Superior d'Enginyeries Industrial, Aeroespacial i Audiovisual de Terrassa

Degree

Bachelor's degree in Aerospace Vehicle Engineering

Student

Armen Baghdasaryan

Director

Luis Manuel Pérez Llera

Title of the Project

Design of an Unmanned Aerial Vehicle with a Mass-Actuated Control System

---

REPORT

Call: Autumn 2019 (Extraordinary)

Date: September 29

Abstract

This thesis presents the analysis, design and evaluation of a blended-wing-body unmanned aerial vehicle with an innovative control system, without any aerodynamic flight-control surfaces.
The aircraft has a system of movable masses which are the main component of the control system, since they can be actuated to alter the center of mass position on longitudinal and lateral axis. The main purpose of the control system is to provide static and dynamic stability throughout the flight envelope, maneuvers, and possible gusts. The main advantage of this implementation is an improvement on the performance, since drag can be considerably reduced during maneuvers. Also, maintenance cost can be reduced, since the mechanical components involved in the control system have less complexity and no expensive actuators are required.
An advanced aerodynamic design for a flying-wing configuration is proposed, where the use of diverse airfoils has been applied, providing high efficiency. From a structural point of view, the aircraft in overall is more robust, since only internal components are mobile. Throughout the thesis, both, analytic and numerical methods have been considered and applied for the design and verification. Regarding the testing of the control system implementation, different flight algorithms have been generated and a simulation for a dynamic case with a vertical gust has been done, with satisfying results.

Declaration

By submitting this thesis, I declare that the entirety of the content is my own, original work and that I have not previously submitted it for obtaining any qualifications.

Date: 29 September 2019

Acknowledgment

Firstly, I would like to express my sincere gratitude to my thesis director, Prof. Luis Manuel Pérez Llera, for the continuous support of my B.S. thesis, for his patience, motivation, and immense knowledge. His guidance helped me in all major subjects related to the thesis.

Additionally I would like to thank my family and my girlfriend, Olga, for the crucial support they have provided throughout all this time.

Dedications

This thesis is dedicated to my family.

Contents

Acronyms

BWB	Blended Wing Body
UAS	Unmanned Aerial System
UAV	Unmanned Aerial Vehicle
GUI	Graphical User Interface
CFD	Computational Flow Dynamics
CAD	Computer Aided Design
BEM	Blade Element Method
AR	Aspect Ratio
MTOW	Maximum Takeoff Weight
PL	Payload
AoA	Angle of attack
GPS	Global Positioning System
GLONASS	GLObal NAvigation Satellite System
PDB	Power Distribution Board
IMU	Inertial Measurement Unit
EASA	European Union Aviation Safety Agency
VLA	Very Light Aircraft

Nomenclature

α	Angle of attack
b	Wingspan
n	Load factor
c_l	Airfoil lift coefficient
c_d	Airfoil drag coefficient
c_m	Airfoil pitching moment coefficient
C_L	Lift coefficient
C_D	Drag coefficient
C_M	Pitching moment coefficient
X_{CG}	Aircraft Center of Mass Position over X-axis
Y_{CG}	Aircraft Center of Mass Position over Y-axis
I	Moment of Inertia Matrix
I_{ii}	Moment of Inertia about i-axis
I_{ij}	Product Moment of Inertia i-j plane
δ_i	Mass-actuator displacement over i-axis

List of Figures

List of Tables

Introduction

1.1 Aim of the Project

The aim of the project is to design an unmanned aerial vehicle with a mass-actuated control system without aerodynamic flight-control surfaces, and to study its viability.

1.2 Scope of the Project

According to the aim of the project and the established depth of analysis, the following tasks have been defined within the scope of the project.

Aerodynamics

- Analytic design of the frame geometry and airfoil selection.
- Design and analysis by XFLR5 software. Validation of the frame design and stability analysis.
- Numerical simulation by Computational Flow Dynamics (CFD) software for design improvement and validation.

Structures

- Analytic structural calculations, dimensioning and materials selection.
- Structural design of the airframe and the control system.
- Structural analysis of the critical parts by ANSYS software for the maximum load factor.

Computational Design

- Computer aided design of the whole structure by CATIA software.
- Preparation of the drawings.

Propulsion

- Required power, thrust and efficiency calculations.

- Selection of adequate propulsion and energy storage systems, according to power requirements and considering the compatibility for possible integration with the mass-actuated control system.

Business

- Potential markets study
- Determination of development cost, fabrication costs, post-sell services and the final price.

Performance and Flight Mechanics

- Analysis of the general equations of motion.
- Mass-actuated control system design and integration with all subsystems.
- Static longitudinal and lateral stability analysis. Determination of stability derivatives, control derivatives and their relationship.
- Design of the flight control algorithm flowchart.
- Development of the flight control algorithm for steady flight and basic maneuvers.
- Numerical analysis of dynamic modes affecting stability.

Systems

- Determination of system requirements.
- Research and selection of required systems for communication, navigation, launching and landing, power supply and control.
- Description of the selected components.
- Research and selection of optional cameras and sensors compatible with the determined Payload (PL).
- Provide the costumer with information regarding possible upgrades.
- Delivery of the technical data sheet

1.3 Requirements

The main requirements established for the project are:

- Design of an unmanned aerial vehicle with a mass-actuated control system, with no aerodynamic mobile control surfaces.
- Design of a control system for pitch and roll control.
- Maximum Takeoff Weight (MTOW) of 25 kg.

1.4 Justification

Unmanned aerial vehicles, also called drones, probably cover the most important part of any international aviation salon nowadays, and capture the interest of hundreds of people, being thus professionals or just ordinary people. The application range of an unmanned aerial vehicle is huge, and for almost each task in or out of the range of capabilities of a human, there can be found some type of UAV. This versatility is the main reason hundreds of companies have inverted on the investigation and production of improved and multitask drones. Considering that this market is in constant growth, it is a good idea to develop such a project, with an innovative control system. The main subject of the current project being the design of an unmanned aerial vehicle without aerodynamic control surfaces, may also offer some advantages in contrast to the traditional models. Some of these advantages could be the totally mechanical or electromechanical control system, which could provide more reliability, reduce maintenance costs, provide structurally simple and robust model, and more autonomy to the aircraft. To position the current project in the competitive market, it seems also reasonable to design a drone with versatile features, making it useful for applications such as mapping, scanning of fire-fighting zones, investigation, and recreational use. The national and European regulations applied to unmanned aerial systems are in constant change and they are more restrictive for heavier category of drones. For this reason, the limit of 25kg of maximum takeoff weight will be marked as a requirement for the project, as the tasks listed before can be achieved with this size of aircraft, and the legislation framework is less restrictive for drones under 25kg. Having a look on the changes for the last few years, it seems clear how unpredictable is the regulation for drones between 25kg and 150kg.

Development

2.1 Legislative Framework

The European Union Aviation Safety Agency (EASA) is still discussing a final regulation framework regarding the Unmanned Aerial Systems. There have been different drafts, such as the “Notice of Proposed Amendment 2017-05 (A)” and the“Notice of Proposed Amendment 2017-05 (B)”, which have not yet been assigned the final status [12]. The proposed drafts are forcing an operating height of less than 120 meters. However, this is a general rule for recreational activities and probably civil and military operations could, exceptionally, exceed these limits. Besides the flight altitude, there is an established maximum takeoff weight of 150 kg. Interestingly, some drone categories offer certain advantages, meaning, less restrictions on the operative conditions. Such is the case of the so called “small unmanned aerial systems”, which are designed to have a maximum takeoff weight of 4 kg. Therefore, it is reasonable to consider that option, provided the wide range of applications this type of drones can offer, combined with the less restrictive nature of EASA drafts for drones under 4 kg.

On the other hand, the normative CS-VLA (Very Light Aircraft (VLA)) and the normative CS-23 (Normal, Utility, Aerobatic and Commuter Airplanes) have been analyzed, since they provide detailed information regarding technical aspects and structural design criteria for the design of an aerial vehicle under 750 kg.

2.1.1 Structural Design

Some of the remarkable points regarding the structural design are:

- The positive limit maneuvering load factor may not be less than 3.8. It is considered to be 4.0.
- The negative limit maneuvering load factor absolute value may not be less than 1.5. It is considered to be -2.0.
- Positive (up) and negative (down) gusts of 15.24 m/s at cruise speed must be considered.
- Positive and negative gusts of 7.62 m/s at dive speed must be considered.

Gust load factors, gust shape, magnitude, load alleviation factor and other parameters have been considered for the structural design throughout next chapters, according to the CS-VLA normative [12].

2.1.2 Avionics

Current drafts, which are still being discussed by the European Aviation Safety Agency, only specify constraints regarding operating conditions. Hence, there are no certification requirements regarding avionics. Therefore, the normative only sets the maximum takeoff mass, the maximum flight altitude and the requirement of navigation lights.
However, the current project requires other systems, essential for a safe flight.

- At first, the aircraft should have launching and landing systems.
- There should be an electronic system, consisting of different subsystems. The electronic system itself should be defined as the global network between all on-board components, linking input and output data related to the aircraft dynamics.
- There should be a communication system, consisting of a receiver and a transmitter. This provides communication between the ground unit and the unmanned aerial vehicle.
- There should be a navigation system, providing the required information regarding the flight altitude, vehicle location, speed, acceleration and other parameters.
- There should be a robust control system, providing autonomy to the vehicle in terms of control, stability and maneuverability.

2.2 State of the Art

In the current market there are diverse unmanned aerial vehicles for almost any kind of application. Similar to conventional aviation unmanned aerial vehicles can be classified by typology, such as fixed-wing airplanes, helicopters, multi-rotor vehicles, etc. Also they can be classified by weight and size. While the big scale unmanned aerial vehicles are mainly targeting military and surveillance fields, the medium and small scale UAVs offer wider range of applications, including search and rescue, scanning of the landscape in agriculture, geography, fire fighting, surveillance, cargo transport in trouble zones, scientific research, and others.

Regarding the vehicle typology and weight, only fixed-wing airplanes under 25kg meet the project requirements. Therefore, a brief research has been done in the market to compare different models and to define a preliminary configuration. Regarding the vehicle purpose, civil and commercial uses have been set for the targeting market.

2.2.1 Conventional models

The following two tables contain basic characteristics of some medium size conventional unmanned aerial vehicles.

Model	**Nostromo Yarara (Argentina)**	**Krunk UAV (Armenia)**	**Primoco UAV (Czech Rep.)**	**Dozor 50 (Russia)**
Wingspan [m]	4.00	4.32	4.90	4.00
Length [m]	2.47	3.80	3.70	2.60
PL [kg]	5	20-30	10-50	8-15
MTOW [kg]	22.5	60	100	50
Max.Speed [km/h]	145	150	150	135
Cruise Speed [km/h]	115	120	100	110
Range [km]	50	580	200	600
Ceiling [km]	3.5	5.4	2.0	4.0
Endurance [h]	6	5	10	6
Take-off	Taxiing	Taxiing	Taxiing	Taxiing

Table 2.1: Conventional models (i)

Figure 2.1: Nostromo Yarara

Figure 2.2: Krunk UAV

Figure 2.3: Primoco UAV

Figure 2.4: Dozor 50

Model	**Orlan-10 (Russia)**	**BPM UAV-LHK (China)**	**Pegaz 011 (Serbia)**	**Selex ES Falco (Italy)**
Wingspan [m]	3.10	3.00	6.34	7.20
Length [m]	1.80	2.53	5.40	5.25
PL [kg]	5	10	40	70
MTOW [kg]	14	25	230	420
Max.Speed [km/h]	150	150	200	216
Cruise Speed [km/h]	90	110	130	140
Range [km]	120	150	100	200
Ceiling [km]	5.0	5.0	3.0	6.5
Endurance [h]	16	3.5	12	14
Take-off	Catapult / Parachute	Taxiing	Taxiing	Taxiing

Table 2.2: Conventional models (ii)

Figure 2.5: Orlan-10

Figure 2.6: BPM UAV-LHK

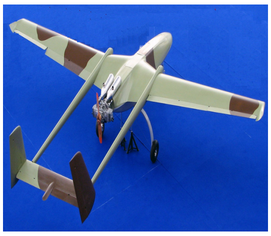

Figure 2.7: Pegaz 011

Figure 2.8: Selex ES Falco

2.2.2 Flying wing models

The following two tables contain basic characteristics of some small and medium scale flying wing unmanned aerial vehicles.

Model	**A.D. Orbiter I (Israel)**	**Conyca Geodrone (Spain)**	**Eleron-10SW (Russia)**	**Eleron-3SW (Russia)**
Wingspan [m]	2.20	1.55	2.20	1.47
Length [m]	1.00	0.90	0.88	0.64
PL [kg]	1.5	0.5	2.5	ND
MTOW [kg]	6.5	2.0	15.5	5.5
Max.Speed [km/h]	140	108	135	130
Cruise Speed [km/h]	45-120	72	75	70
Range [km]	50	45	50 LOS / 60 OFF	25 LOS / 50 OFF
Ceiling [km]	4.5	4.0	4.0	5.0
Endurance [h]	1.5	1.0	2.5	1.6
Take-off	Catapult / Parachute	Catapult / Parachute	Catapult / Parachute	Catapult / Parachute

Table 2.3: Flying wing models (i)

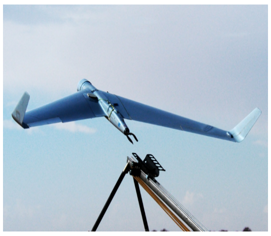

Figure 2.9:
A.D. Orbiter I

Figure 2.10:
Conyca Geodrone

Figure 2.11:
Eleron-10SW

Figure 2.12:
Eleron-3SW

Model	**C-Astral ATLAS (Slovenia)**	**C-Astral Bramor (Slovenia)**	**Feiyu Tech SkyCam (China)**	**Feiyu Tech X8 (China)**
Wingspan [m]	1.55	2.30	1.20	2.12
Length [m]	0.82	0.96	0.60	0.99
PL [kg]	0.3	0.6	0.4	0.6
MTOW [kg]	2.0	3.8	1.95	5.0
Max.Speed [km/h]	108	108	75	70
Cruise Speed [km/h]	58	58	65	65
Range [km]	30 LOS	30 LOS	20	5 LOS / 15 OFF
Ceiling [km]	5.0	5.0	1.5	1.0
Endurance [h]	1.2	3.0	0.6 - 0.9	0.6 - 0.9
Take-off	Catapult / Parachute	Catapult / Parachute	Catapult / Parachute	Catapult / Parachute

Table 2.4: Flying wing models (ii)

Figure 2.13:
C-Astral ATLAS

Figure 2.14:
C-Astral Bramor

Figure 2.15:
Feiyu Tech SkyCam

Figure 2.16:
Feiyu Tech X8

2.2.3 Materials

Considering weight limitations, it is important to study the current State-of-the-art regarding materials used in the Aerospace Industry, specially for small and medium size vehicle design.

For the same reason, some high performing metals, such as Steel and Titanium alloys, which offer excellent properties have been discarded due to their high specific weight. Aluminum alloys and some aluminum composites, on the other hand, are interesting to be considered, since they offer a mix of good mechanical properties and relatively lower specific weight.

- For instance, Aluminum 2024 T3 is widely used in the industry for airframe structural components, that by their nature, withstand less loads than the primary components and are less critical.
- Glass reinforced aluminum, also known as GLARE, is a fiber metal laminate. It is mostly used as a skin material for the fuselage. It is composed of the next elements:
    - Aluminum 2024T3 sheets
    - S2 Glass fibers
    - Cytec FM94 epoxy matrix

Regarding materials of low specific weight, composites and plastics stand out with their good mechanical properties. Fiberglass, for example, is a type of fiber-reinforced plastic using glass fiber. One of the main characteristics of the glass fibers is the high strength-to-weight ratio. Glass fibers usually have higher breaking point than carbon fibers. Also, glass fiber composites are cheaper than carbon fiber composites, and have similar resistance to corrosion. Commercially,the two most known types of fiberglass are:

- E-glass, mainly for electrical application, is alumino-borosilicate glass with less than 1% weight on weight alkali oxides.
- S-glass, which is meant to be “stiff”, is alumino-silicate glass without CaO but with high MgO content, offering high tensile strength.

Carbon fiber composites, considering their mechanical properties, are cutting edge lightweight materials, with excellent performance. They are approximately 70% lighter than steel and 40% lighter than aluminum. These composites have high stiffness-to-weight ratio.

Carbon fiber is about 3 times stiffer than steel and aluminum for a given weight. Carbon fibers are, generally, more expensive than glass fibers. However, carbon fibers have a very high fatigue resistance. They almost do not deteriorate over time, and offer similar mechanical properties under dynamical cyclic loads.

Acrylonitrile Butadiene Styrene (ABS plastic), is a common thermoplastic polymer. ABS plastics stand out with high impact resistance and toughness, and they are relatively easily machined. Combined with the current state of Injection Molding and 3D printing technologies, it is widely used in the industry.

Normally, medium and small size aircrafts are covered by a thin film. Depron foam, composite materials, plastics and sometimes metal sheets are the most common materials for the skin. Nowadays, light weight options include commercially known plastic film called MonoKote, which consits of light weight plastic shrink wrap film, with an adhesive on one side, used to cover and form the surfaces of the aircraft. Heat gun is used for the final application. [29]

Table 2.5 summarizes some of the most important properties of the materials listed above.

Material	**Density** [g/cm^3]	**Young Modulus** [GPa]	**Shear Modulus** [GPa]	**Yield Str.** [MPa]	**Ult. Tensile Str.** [MPa]	**Ult. Comp. Str.** [MPa]
Aluminium 2024	2.78	73.10	27.60	324	469	358
GLARE	2.50	58.10	17.60	284	620	NF
CFRP T800S	1.80	154.00	4.30	945	2950	1550
S-Glass	2.49	86.00	35.00	4085	4800	5000
ABS	0.90	2.14	0.083	42	52.70	52.70

Table 2.5: Materials properties [27]

2.3 Proposed solution

Fixed-wing unmanned aerial vehicles are classified into two groups based on the wing-body configuration. On one hand there are conventional airplanes, consisting of a fuselage, wing and tail, while on the other hand there are Blended Wing Body (BWB) airplanes. Conventional airplanes normally control the pitch motion about the lateral axis by the deflection of the elevator situated on the tail. Regarding the roll motion about the longitudinal axis, both configurations use asymmetrical deflection of the ailerons, and for the yaw motion about the vertical axis the vertical stabilizer is used. Since the main requirement of the project is to design an unmanned aerial vehicle with a mass-actuated control system with only pitch and roll motions, and without aerodynamic flight-control surfaces, it is reasonably admissible to get rid of the tail. Although a conventional model would allow a larger displacement for the mobile mass along the longitudinal axis, the extra weight and drag caused by the tail would not be compensated. Therefore, the flying wing configuration has been chosen, with a maximum takeoff mass of 4 kg.

Regarding flight control and based on the project requirements, the proposed solution consists in having a mass-actuated system which changes the center of gravity position of the aircraft on the longitudinal and lateral axis independently. Lateral displacement of the center of gravity should be used for lateral control and stability, therefore, it should control the rolling motion. On the other hand, longitudinal displacement of the center of gravity should impact the pitching moment and its derivative. Therefore, an adequate weight distribution has been considered crucial. Designing a robust airframe, enabling the motion of movable parts within the structure has been an important task.

The development of this solution will be discussed throughout the following chapters, including aerodynamic design, structural design, design of a propulsion system, research and selection of electronic components and design of a control system, implementation of the required flight control algorithms and simulation of dynamic cases.

2.4 Development of the chosen solution

2.4.1 Frames of Reference

Throughout the study of the aircraft performance and flight mechanics different frames of reference have been used. A brief description of those systems of reference has been done.

2.4.1.1 Earth frame

Earth frame of reference has its origin O_e at any point on the Earth surface, and the coordinates are given by the longitude τ_e and latitude λ_e.

- The z_e axis is positive towards the center of the Earth
- The x_e axis is positive in the direction of north
- The y_e axis is positive in the direction of east

It is mainly used for Navigation, specially for the representation of the aircraft trajectory.

2.4.1.2 Local-Horizon frame

Local-Horizon frame of reference follows almost the same principles as the Earth frame. The only difference is the origin, O_h, which normally is placed on the aircraft symmetry plane, but more precisely, on the center of gravity.

2.4.1.3 Body frame

Body frame of reference represents the aircraft as a rigid body. Therefore, its origin O_b is coincident with the aircraft center of gravity.

- The x_b axis corresponds to the longitudinal axis and it is contained in the symmetry plane. It is positive from the tail to the nose.
- The z_b axis also lies on the symmetry plane, point downwards.
- The y_b axis, perpendicular to the previous two axis, is positive pointing to the right wing.

It is important to note that according to the proposed solution the center of gravity is going to be continuously moved along x_b and y_b directions. Therefore, the origin of the Body frame, fixed to the center of gravity, is also going to move. The frame of reference orientation, however, is going to be conserved.

2.4.1.4 Wind frame

Wind frame of reference is linked to the aircraft instantaneous aerodynamic velocity. The origin O_w is fixed to the center of gravity.

- The x_w axis is positive in the direction of the instantaneous aerodynamic velocity vector.
- The z_w axis is perpendicular to the x_w, in the plane of symmetry, positive downwards.
- The y_w axis is perpendicular to the previous two axis, and generally, it is positive on the right wing direction.

2.4.1.5 Transformation matrices

Throughout the next chapters some transformation matrices will be used when some vectors are required to be calculated regarding another frame of reference.

2.4.1.6 Body frame orientation regarding Local-horizon frame

$$L_{bh} = \begin{bmatrix} \cos\theta\cos\psi & \cos\theta\sin\psi & -\sin\theta \\ \sin\phi\sin\theta\cos\psi - \cos\phi\sin\psi & \sin\phi\sin\theta\sin\psi + \cos\phi\cos\psi & \sin\phi\cos\theta \\ \cos\phi\sin\theta\cos\psi + \sin\phi\sin\psi & \cos\phi\sin\theta\sin\psi - \sin\phi\cos\psi & \cos\phi\cos\theta \end{bmatrix}$$

where ψ is the yaw angle, θ is the pitch angle and ϕ is the roll angle.

2.4.1.7 Body frame orientation regarding Wind frame

$$L_{bw} = \begin{bmatrix} \cos\alpha\cos\beta & -\cos\alpha\sin\beta & -\sin\alpha \\ \sin\beta & \cos\beta & 0 \\ \sin\alpha\cos\beta & -\sin\alpha\sin\beta & \cos\alpha \end{bmatrix}$$

where β is the sideslip angle and α is the angle of attack.

2.4.2 General Equations of Motion

A fundamental hypothesis for the study of the aircraft flight mechanics is to consider it as a solid body, with six degrees of freedom. The six degrees of freedom consist of three translations of the center of gravity regarding the earth system of reference, and three rotations affecting aircraft's body frame orientation regarding the local-horizon axis system.

Although the motion of the control system components inside the structure may not seem compatible with the definition of a rigid body, it will be neglected and considered quasi-static, since the movement is considerably slow and the CG variation is low in comparison to the aircraft wingspan and mean aerodynamic chord. This will be justified in detail in the following chapters.

However, the study of the aircraft mechanics will, obviously, be affected by the specific control system and the solution will differ from the traditional one. The reason is that once the center of gravity is moved from the aircraft symmetry plane ($x_b - z_b$), the Inertia Tensor terms can not be neglected or simplified. Additionally, control derivatives which generally are related to the deflection of the aircraft control surfaces, will be of a different nature.

The study will begin with the application of Momentum theorem

$$\vec{F} = \frac{d(m\vec{V})}{dt} \tag{2.1}$$

where V is the absolute velocity of the aircraft center of gravity in an inertial frame of reference, and $\vec{F}$ the sum of all the external forces. Considering the term $\dot{m}V$ negligible, the first equation can be rewritten as:

$$\vec{F} = m\frac{d\vec{V}}{dt} \tag{2.2}$$

According to the Angular momentum theorem:

$$\begin{aligned} \vec{G} &= \frac{d\vec{h}}{dt} \\ \vec{h} &= I\vec{\omega} \end{aligned} \tag{2.3}$$

where $\vec{G}$ is the sum of external moments, $\vec{h}$ is the angular momentum, and I is the aircraft inertia tensor.

$$I = \begin{bmatrix} I_x & -J_{xy} & -J_{xz} \\ -J_{xy} & I_y & -J_{yz} \\ -J_{xz} & -J_{yz} & I_z \end{bmatrix}$$

The aircraft absolute velocity, external forces, external moments and rotational velocity components are as follows:

$$\begin{aligned} \vec{V} &= (u, v, w)^T \\ \vec{\omega} &= (p, q, r)^T \\ \vec{F} &= (F_x, F_y, F_z)^T \\ \vec{G} &= (L,\ N,\ M\ )^T \end{aligned} \tag{2.4}$$

Since the Body frame of reference is a rotating system, the time-derivatives of its vectors have an extra term in any inertial frame. Therefore, previous equations can be written as:

$$\vec{F} = m\left(\frac{\partial \vec{V}}{\partial t} + \vec{\omega} \times \vec{V}\right) \tag{2.5}$$

and

$$\vec{G} = \frac{\partial \vec{h}}{\partial t} + \vec{\omega} \times \vec{h} \tag{2.6}$$

The previous equations, once developed, form the next system:

$$\begin{aligned} F_x &= m\left(\dot{u} - rv + qw\right) \\ F_y &= m\left(\dot{v} + ru - pw\right) \\ F_z &= m\left(\dot{w} - qu + pv\right) \end{aligned} \tag{2.7}$$

$$\begin{aligned} L &= I_x\dot{p} - J_{xz}(\dot{r} + pq) + (I_z - I_y)qr - \boldsymbol{J_{xy}(\dot{q} - pr) - J_{yz}(q^2 - r^2)} \\ M &= I_y\dot{q} + J_{xz}(p^2 - r^2) + (I_x - I_z)pr - \boldsymbol{J_{xy}(\dot{p} + qr) - J_{yz}(\dot{r} - pq)} \\ N &= I_z\dot{r} - J_{xz}(\dot{p} - qr) + (I_y - I_x)pq - \boldsymbol{J_{xy}(p^2 - q^2) - J_{yz}(\dot{q} + pr)} \end{aligned} \tag{2.8}$$

The external forces and moments can be classified as propulsive, aerodynamic and gravitational.

$$\begin{aligned} \vec{F} &= \vec{F_T} + \vec{F_A} + \vec{F_G} \\ \vec{G} &= \vec{G_T} + \vec{G_A} \end{aligned} \tag{2.9}$$

The gravitational force, represented on the local-horizon system is:

$$(\vec{F}_G)_h = \begin{bmatrix} 0 \\ 0 \\ mg \end{bmatrix} \tag{2.10}$$

The gravitational force can be projected on the body-frame using the transformation matrix:

$$(\vec{F}_G)_b = L_{bh}(\vec{F}_G)_h = \begin{bmatrix} -mg\sin\theta \\ mg\cos\theta\sin\phi \\ mg\cos\theta\cos\phi \end{bmatrix} \tag{2.11}$$

where θ is the aircraft pitching angle and ϕ is the roll angle. The six equations regarding the aircraft dynamics can be written as:

$$\begin{aligned} -mg\sin\theta + F_{Tx} + F_{Ax} &= m\left(\dot{u} - rv + qw\right) \\ mg\cos\theta\sin\phi + F_{Ty} + F_{Ay} &= m\left(\dot{v} + ru - pw\right) \\ mg\cos\theta\cos\phi + F_{Tz} + F_{Az} &= m\left(\dot{w} - qu + pv\right) \end{aligned} \tag{2.12}$$

$$\begin{aligned} L &= I_x\dot{p} - J_{xz}(\dot{r} + pq) + (I_z - I_y)qr - \boldsymbol{J_{xy}(\dot{q} - pr) - J_{yz}(q^2 - r^2)} \\ M &= I_y\dot{q} + J_{xz}(p^2 - r^2) + (I_x - I_z)pr - \boldsymbol{J_{xy}(\dot{p} + qr) - J_{yz}(\dot{r} - pq)} \\ N &= I_z\dot{r} - J_{xz}(\dot{p} - qr) + (I_y - I_x)pq - \boldsymbol{J_{xy}(p^2 - q^2) - J_{yz}(\dot{q} + pr)} \end{aligned} \tag{2.13}$$

Furthermore, the hypothesis of Flat-Earth approximation is applied, according to which the Earth-frame is considered inertial. Therefore, the centripetal and Coriolis accelerations are neglected in the calculation of the aircraft's acceleration regarding the Earth frame. Another approximation which simplifies the study of the aircraft dynamics is to despise the angular velocity of the local-horizon frame regarding the Earth-frame. Therefore, aircraft's angular velocity can be linked with the Body frame orientation angles regarding the local-horizon frame.

$$\begin{aligned} p &= \dot{\phi} - \dot{\psi}\sin\theta \\ q &= \dot{\theta}\cos\phi + \dot{\psi}\cos\theta\sin\phi \\ r &= -\dot{\theta}\sin\phi + \dot{\psi}\cos\theta\cos\phi \end{aligned} \tag{2.14}$$

The previous equations can be inverted, resulting:

$$\begin{aligned} \dot{\phi} &= p + (q\ \sin\phi + r\ \cos\phi)\tan\theta \\ \dot{\theta} &= q\ \cos\phi - r\ \sin\phi \\ \dot{\psi} &= (q\ \sin\phi + r\ \cos\phi)\sec\theta \end{aligned} \tag{2.15}$$

The first two equations combined with the dynamics system of six equation form a complete system of first order nonlinear ordinary differential equations, where the parameters u, v, w, p, q, r, θ and ϕ can be calculated as time-functions, if the aerodynamic and propulsive forces and moments are introduced.

Aircraft's absolute velocity regarding the Earth frame can be written as:

$$\vec{V}_e = \begin{bmatrix} \dot{x}_e \\ \dot{y}_e \\ \dot{z}_e \end{bmatrix} = L_{hb}\vec{V}_b = L_{hb} \begin{bmatrix} u \\ v \\ w \end{bmatrix} = {L_{bh}}^T \begin{bmatrix} u \\ v \\ w \end{bmatrix} \tag{2.16}$$

and using the transformation matrix L_{bh}, the next linear kinematic equations are obtained:

$$\begin{gathered} \dot{x}_e = (\cos\theta\cos\psi)u + (\sin\phi\sin\theta\cos\psi - \cos\phi\sin\psi)v + (\cos\phi\sin\theta\cos\psi + \sin\phi\sin\psi)w \\ \dot{y}_e = (\cos\theta\sin\psi)u + (\sin\phi\sin\theta\sin\psi + \cos\phi\cos\psi)v + (\cos\phi\sin\theta\sin\psi - \sin\phi\cos\psi)w \\ \dot{z}_e = (-\sin\theta)u + (\sin\phi\cos\theta)v + (\cos\phi\cos\theta)w \end{gathered} \tag{2.17}$$

Substituting in the previous system the values of u, v, w, ψ, θ and ϕ as a time-function (obtained after the integration of the dynamic and angular kinematic systems), aircraft's center of gravity law of motion can be found. The integration of the law of motion will provide the equation of the aircraft trajectory.

2.4.3 Airfoil Characteristics

Generally, flying wings can be equipped with any airfoil if combined with the appropriate wing sweep and twist. These two usually cause a performance loss, specially if the twist value is high. However, it can be minimized by choosing airfoils with zero or positive pitching moment coefficients. Over the past decades, a huge number of airfoils have been created with the objective of:

- Reducing drag in comparison to existing airfoils
- Reducing torsional moment (smaller pitching moment coefficients)
- Increasing lift coefficient versus angle of attack, in comparison to existing low C_m airfoils

The importance of the pitching moment coefficient for the flying wings is due to its impact on the longitudinal stability. While a conventional airplane can compensate the pitching moment with tail horizontal stabilizer, a flying wing has no backup.

Regarding airfoils, their shape is composed of two parts: a camber distribution (camber line) and a thickness distribution. The only way to achieve a positive pitching moment coefficient and the required amount of lift is to use S-shaped camber line, which is also called a reflexed camber line [3]. Flying wings and, in general, tailless airplanes can be divided into three groups, depending on how they achieve longitudinal stability.

- Plank wing (without sweep): the longitudinal stability is achieved solely by the airfoil. A plank requires an airfoil with a positive moment coefficient. A twist does not help for stability for this configuration, but can improve the stall characteristics of the wing.

- Swept wing: the combination of sweep and twist provides more flexibility for airfoils selection. However, airfoils with positive pitching moment coefficient still provide better performance. Low and positive moment coefficient and a small amount of twist can be achieved by airfoils with little camber and a neutral or slightly reflexed camber line.

- Para-foil (wing with a low position of the center of gravity): the moment coefficient is less important and normally traditional airfoils with negative moment coefficients can be used. The center of gravity can be chosen to guarantee stability but also airfoils can be chosen to provide higher penetration speeds. The pitching moment coefficient possess no strong restriction on the airfoil shape.

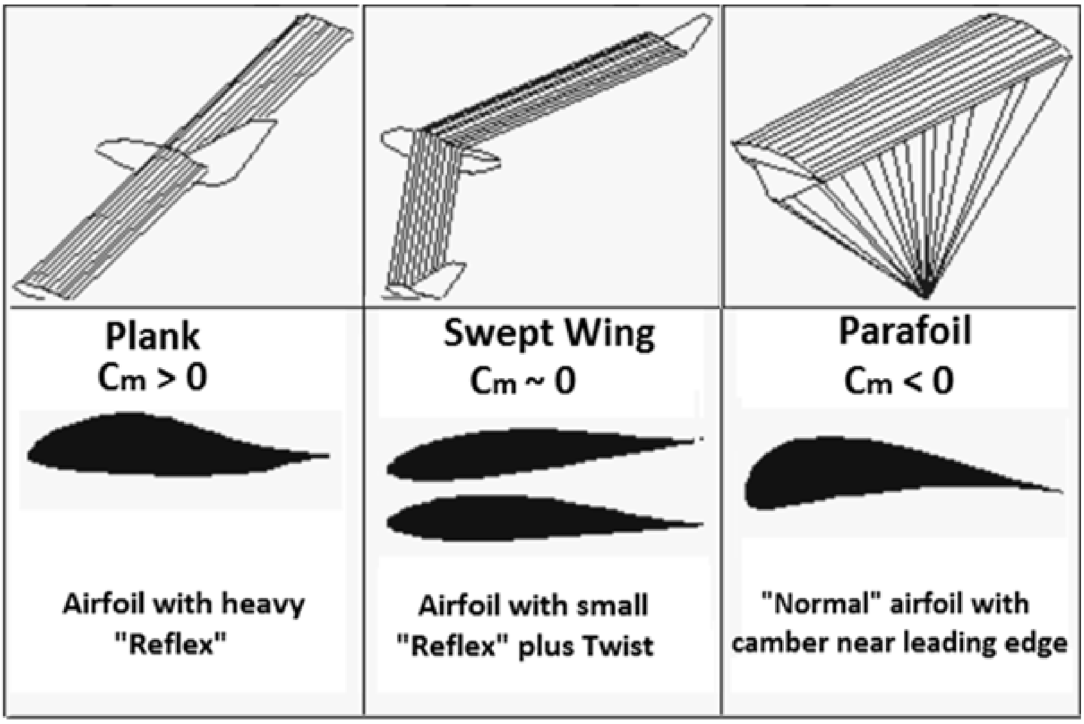

Figure 2.17: Tailless aircraft configurations and required moment coefficient [14]

For conventional airplanes the usage of airfoils with reflex camber line is rare to find as they are unique to tailless airplanes. The analysis of reflex airfoils has always been an interesting and difficult task for aerodynamicists, as those airfoils are very sensitive with respect to changes in Reynolds Number [4].

2.4.3.1 Airfoil characteristics for Flying Wings

According to *Theory of wing sections*[5], and other sources, pitching moment coefficient C_m and the shape of the camber line are directly related. Specially, the shape of the rear part of the camber line has the biggest influence on C_m. Therefore, reflexing the camber shape near the trailing edge it is possible to achieve C_m values close to the desired one. However, the objective is not only the achievement of the desired C_m, but also it is important to have an airplane with high penetration speed and good L/D ratio. Adding these last two conditions to the problem, it is possible to observe that while reflexing the camber line to get closer to the desired C_m value, the Lift vs Drag polar moves down. It also reduces the Lift at any angle of attack and what is even worse, it reduces the maximum lift coefficient. This means that stall speed gets into higher values, which is not desired.

On the other hand, it is known that to increase lift it is required to increase the maximum camber, with the downside of reducing the moment coefficient.

At this point, it seems impossible to achieve the desired C_m with an adequate L/D ratio and stall speed. However, there is still one parameter that helps to solve the problem, which is the location of the maximum camber. The maximum camber location has small influence on the Lift to Drag polar, but a strong impact on the moment coefficient. Pitching moment coefficient increases when the maximum camber location gets closer to the leading edge.

Therefore, the airfoil design process is based on the next steps:

- Reflex the camber to get positive C_m value.
- This affects the L/D ratio and the stall speed. Therefore, the camber length is increased.
- The previous step decreases the C_m, so the maximum camber location must be moved closer to the leading edge, increasing again C_m.

Reflex camber airfoils are designed based on this last phenomenon: moving the location of maximum camber to the first quarter of the chord length.

2.4.3.2 Airfoil comparison

Swept wing with twist configuration has been chosen since it offers better performance if the twist is kept at low values [3]. Based on a research of the current market, a preliminary prototype has been defined, which should operate at 16 m/s at cruise flight. The mean aerodynamic chord is set to 510 mm. Therefore, the range of Reynolds number is set from 200000 to 1000000 (at cruise speed $Re = 555000$).

Two groups of airfoils have been analyzed separately.

The first group, including Martin Hepperle airfoils (MH-45, MH-49 and MH-60) with lower average thickness, is meant to be used for the tip section.

The second group, including Eppler airfoils (E186, E193 and E226), is supposed to be used at the core section where higher thickness is required.

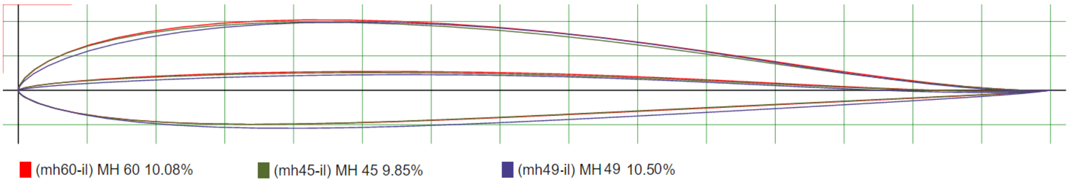

Figure 2.18: First group: MH-45, MH-49 and MH-60 airfoils [16]

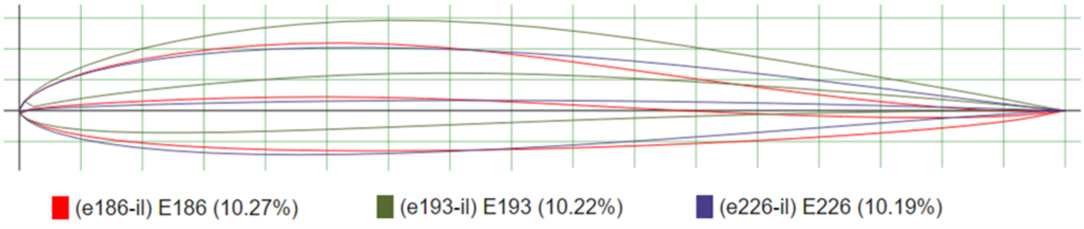

Figure 2.19: Second group: E186, E193 and E226 airfoils [16]

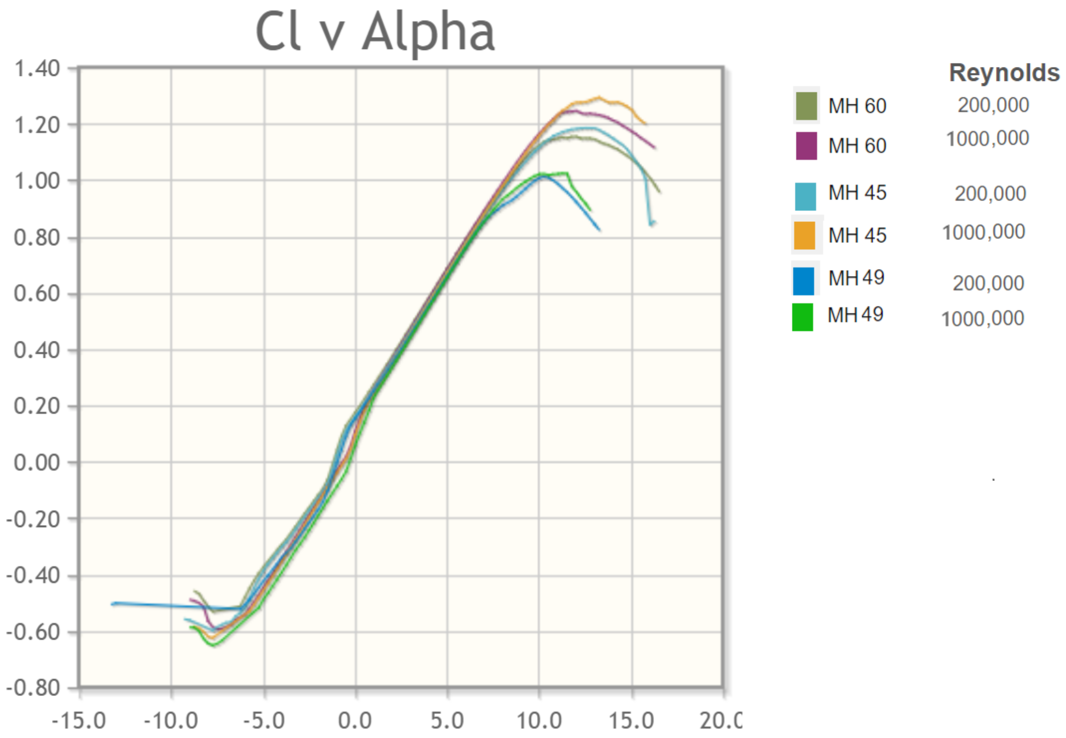

Figure 2.20: First group: Lift coefficient versus angle of attack [16]

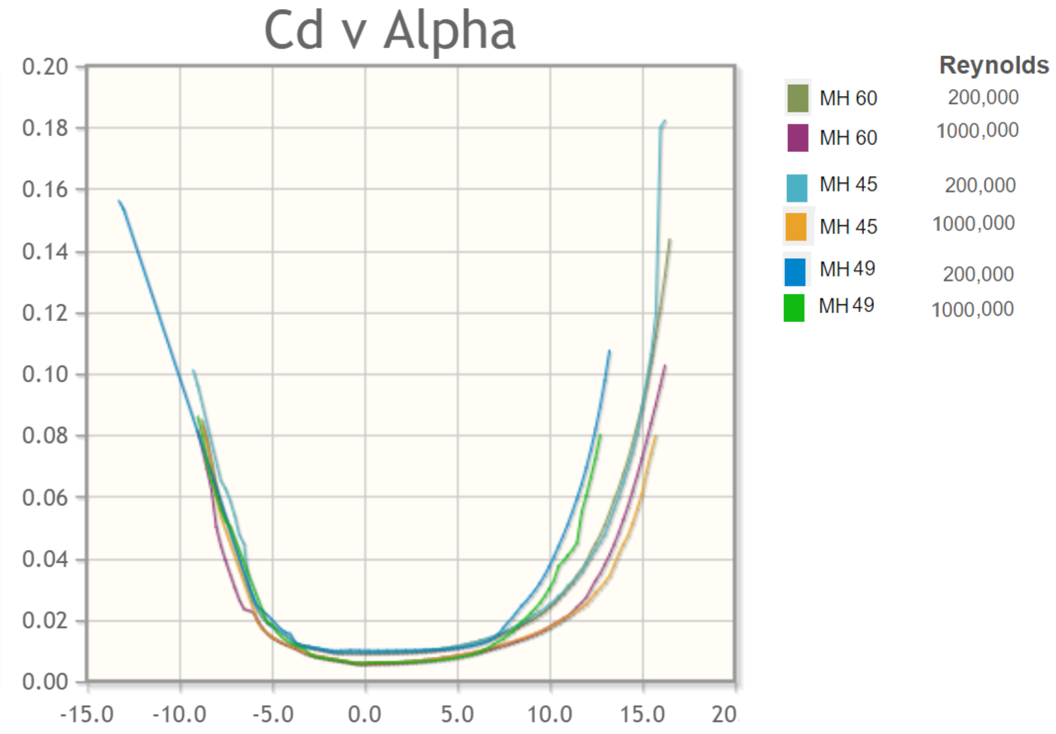

Figure 2.21: First group: Drag coefficient versus angle of attack [16]

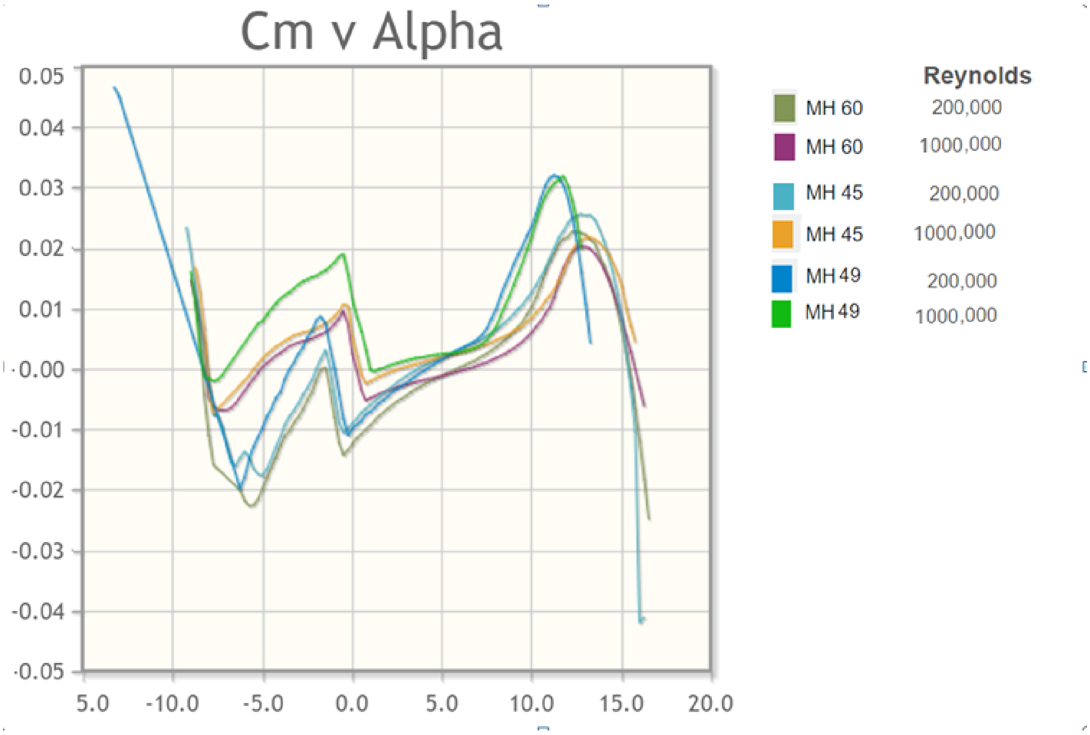

Figure 2.22: First group: Moment coefficient versus angle of attack [16]

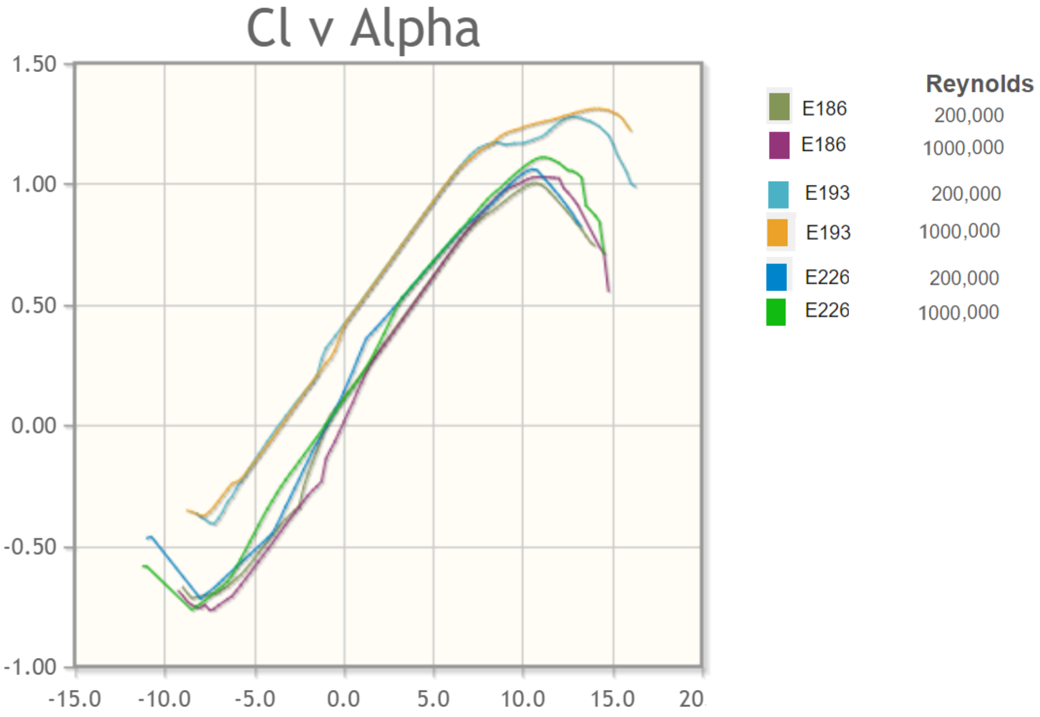

Figure 2.23: Second group: Lift coefficient versus angle of attack [16]

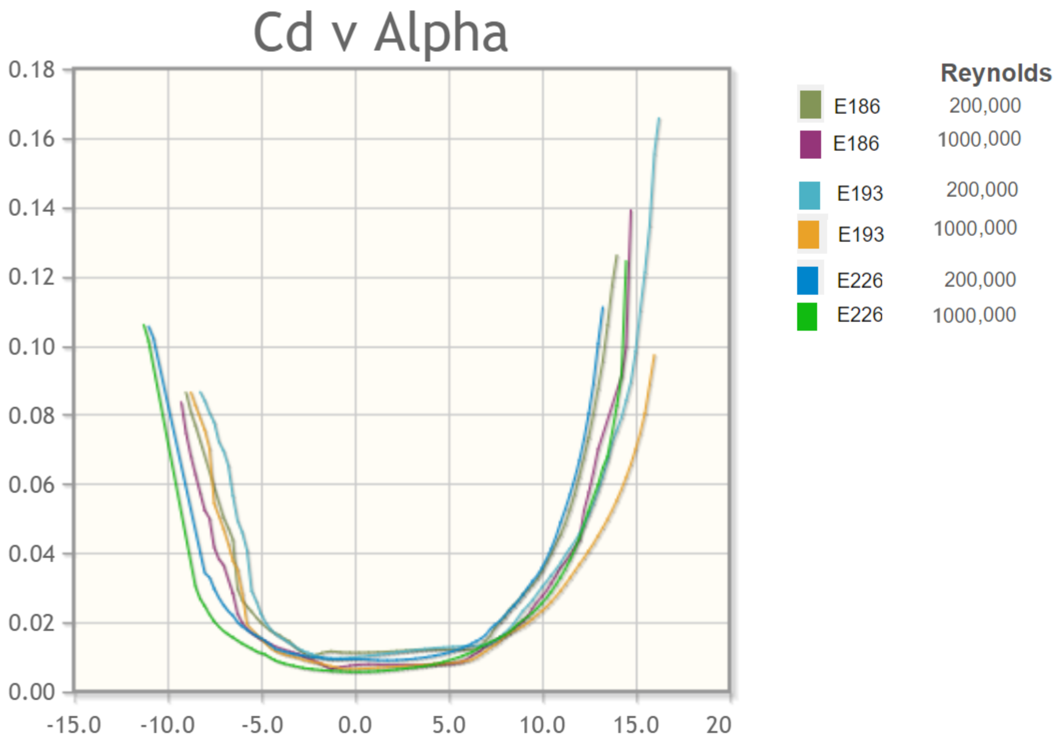

Figure 2.24: Second group: Drag coefficient versus angle of attack [16]

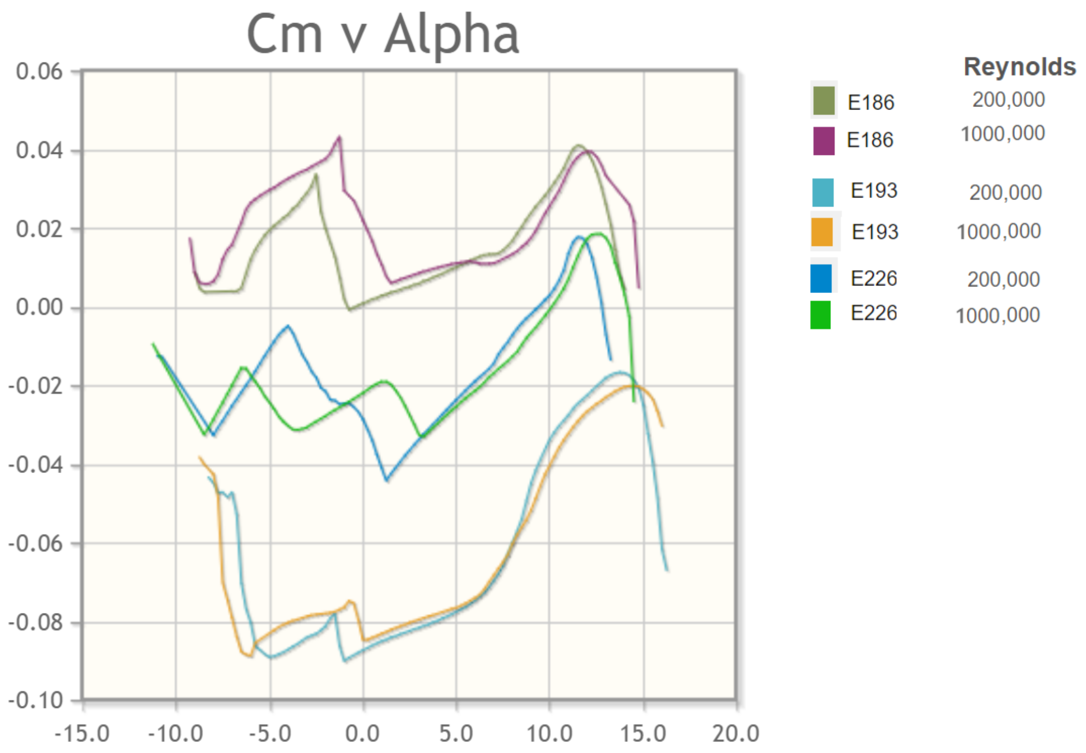

Figure 2.25: Second group: Moment coefficient versus angle of attack [16]

	MH45		MH49		MH60	
	Value	Weighted Value	Value	Weighted Value	Value	Weighted Value
$C_{l\,max}$	1.3		1.02		1.25	
$\frac{C_{l\,max}}{Max(C_{l\,max})}$	1.00	0.400	0.785	0.314	0.962	0.3848
$C_{d\,max}$	0.08		0.08		0.10	
$\frac{C_{d\,max}}{Max(C_{d\,max})}$	0.8	-0.258	0.8	-0.258	1	-0.300
$C_{m\,c/4}$	0.0145		0.01		0.0140	
$\frac{C_{m\,c/4}}{Max(C_{m\,c/4})}$	1	0.300	0.690	0.207	0.966	0.290
Total		0.442		0.263		0.3748

Table 2.6: First group: Ordered weighted averaging for MH45, MH49 and MH60

	E186		E193		E226	
	Value	Weighted Value	Value	Weighted Value	Value	Weighted Value
$C_{l\,max}$	1.05		1.30		1.10	
$\frac{C_{l\,max}}{Max(C_{l\,max})}$	0.808	0.323	1.00	0.400	0.846	0.338
$C_{d\,max}$	0.12		0.16		0.11	
$\frac{C_{d\,max}}{Max(C_{d\,max})}$	0.75	-0.225	1	-0.3	0.69	-0.206
$C_{m\,c/4}$	0.0174		-0.0642		-0.0140	
$\frac{C_{m\,c/4}}{Max(C_{m\,c/4})}$	0.271	0.0813	-1.00	-0.300	-0.218	-0.0654
Total		0.1793		-0.200		-0.2428

Table 2.7: Second group: Ordered weighted averaging for E186, E193 and E226 [16]

In the previous tables, $C_{l_{max}}$, $C_{d_{max}}$ and $C_{m_{c/4}}$ is populated for each airfoil. Then, each value is normalized by the maximum value of the group. Ordered weighted averaging criteria is as follows:

- Maximum lift coefficient is evaluated as the 40% of the total score.
- Maximum drag coefficient is evaluated as the 30%, and subtracted from the total score, since it has a negative effect.
- The absolute value of the pitching moment coefficient is the 30% of the total score.

From the first group of airfoils, MH45 has been selected. This airfoil offers the highest coefficients of pitching moment and lift. From the airfoil C_l vs α graph it is possible to observe that it also has higher stall angle. This characteristic is specially important for airfoils at tip section, since the twist distribution may cause higher angle of incidence. For the core section E186 airfoil has been chosen. It is the only airfoil from the second group with a positive pitching moment coefficient. Even if in head to head comparison E186 has lower $C_{l_{max}}$ than E193 and E226, and also higher $C_{d_{max}}$ than E226, the requirement of null or positive pitching moment is only fulfilled with the E186.

2.4.4 Flying Wing design

The geometric design of the wing has been divided into three parts:

- At first, the importance of some basic concepts has been analyzed, such as the neutral point, sweep and twist distribution, followed by some analytic calculations.
- Then, the preliminary model is recreated in XFLR5 software for validation and stability evaluation.
- At the final stage, and in order to get more convincing and precise results, the prototype has been analyzed by more advanced software, Ansys Fluent.

2.4.4.1 Frame design

Based on the State of the Art analysis, a preliminary concept has been defined with the following geometric parameters.

Parameter		**Symbol**	**Magnitude**
Wingspan		b	2.40 m
Chord length at root		l_r	0.74 m
Chord length at tip		l_t	0.18 m
Sweep angle at c/4 line		$\varphi_{0.25}$	25.11°
Design lift coefficient		C_L	0.5
Root section E 186	Pitching Moment Coef.	$C_{m,r}$	0.0150
	Zero Lift AoA	$\alpha_{0,r}$	$-1.04°$
Tip section MH 45	Pitching Moment Coef.	$C_{m,t}$	0.0145
	Zero Lift AoA	$\alpha_{0,t}$	0.5°
Desired stability coefficient		σ	0.05

Table 2.8: Parameters for the required twist calculation

First of all the mean aerodynamic chord has been calculated, where λ is the taper ratio of the wing.

$$\lambda = \frac{l_t}{l_r} = \frac{180}{740} = 0.243 \tag{2.18}$$

$$l_\mu = \frac{2}{3} \cdot \frac{1+\lambda+\lambda^2}{1+\lambda} \cdot l_r = 510mm \tag{2.19}$$

The spanwise location of the mean aerodynamic chord has been calculated as follows:

$$y = \frac{b}{2} \cdot \frac{l_r - l_\mu}{l_r - l_t} = \frac{2400}{2} \cdot \frac{740-510}{740-180} = 493mm \tag{2.20}$$

Then the neutral point (n.p.) has been determined as shown in the Figure 2.26, by a geometrical method. First of all a line parallel to the fuselage center line is traced at the spanwise station y, where the chord is equal to l_μ. The neutral point is approximately located at the $c/4$ point of that chord line.

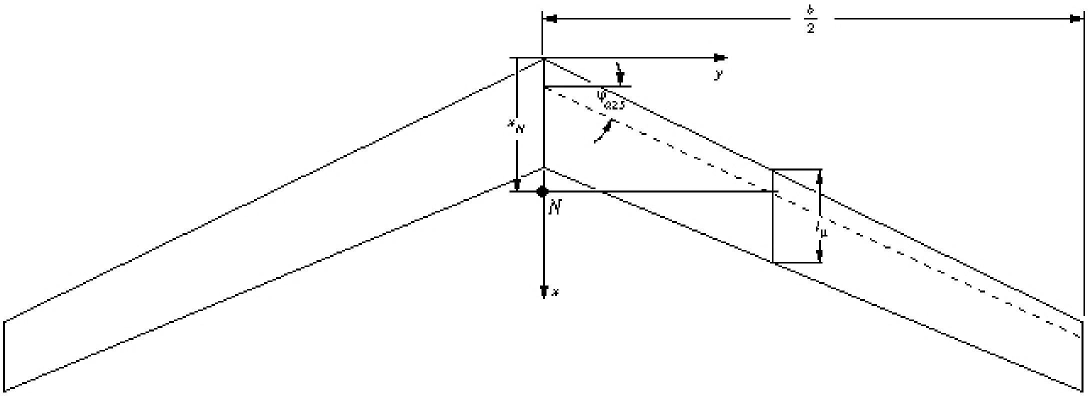

Figure 2.26: Geometrical determination of the Neutral point [3]

Neutral point coordinates have been calculated with the next formulas:

$$X_N = \frac{l_r}{4} + \frac{b(1+2\lambda)}{6(1+\lambda)} \cdot \tan\varphi_{0.25} \qquad \text{if taper ratio} < 0.375 \tag{2.21}$$

$$X_N = \frac{740}{4} + \frac{2400 \cdot (1+20.243)}{6 \cdot (1+0.243)} \cdot \tan 25.11^\circ \;\approx\; 409mm$$

The location of the center of gravity should be in front of the neutral point, as a requirement for the longitudinal stability. However, it does not guarantee equilibrium. It is possible to achieve equilibrium of moments only by a combination of arifoils and twist distribution[3]. For conventional airplanes the process of setting up a trimmed condition is straightforward due to the possibility of adjusting the incidence angles of the wing and the tail during the first flight tests. However, flying wings come with a built in twist, and any alteration is restricted after the construction. Therefore, it is very important to get a theoretically accurate combination of airfoils, frame and twist before the construction of a prototype.

2.4.4.2 Twist calculation

Since the wing has no flaps, twist distribution can be calculated for a singular trimmed lift coefficient, which usually lies somewhere between the best glide and the best climb performance of the airfoil [3].

Coefficients of pitching moment and lift are determined by averaging the corresponding values of each airfoil.

The required twist of the wing can be divided into two categories:

- Geometric Twist: it is built into the wing as the difference between the $X - axis$ of the root and the tip sections. For conventional airplanes it corresponds to the angle between the wing plane and the tail plane. A positive twist means a smaller angle of incidence at the tip section (washout). Normally large geometric twist is used to stabilize wings with small sweep, but the main drawback is the large amount of induced drag [3].

- Aerodynamic Twist: it is the difference between the zero lift AoA of root and tip section airfoils. It reduces the amount of geometric twist. The zero lift AoA is determined from each airfoil polar plots. Furthermore, a positive pitching moment coefficient also reduces the required amount of geometric twist.

According to [3], the required twist is calculated in two steps. The first one is based on using the graph illustrated in Figure 2.27, [3]. Previously determined prototype parameters shoul be used, with the trimmed C_L and a selected stability coefficient influence. The second step consists in using the graph illustrated in Figure 2.28, [3], with the influence of the pitching moment. First of all, the wing Aspect Ratio (AR) has been calculated:

$$AR = \frac{b^2}{S} = \frac{2.4^2}{1.05} \approx 5.5 \tag{2.22}$$

where S is the surface of the wing obtained from the Computer Aided Design (CAD) software (CATIA), based on the frame parameters.

As explained before, for the first part of the required twist calculation only the trimmed C_L and the stability coefficient will be considered. Therefore the value of the required twist will be valid for a wing which is trimmed at $(C_L)^* = 1.0$ with a stability coefficient of $\sigma^* = 10\%$, which airfoils have null pitching moment coefficient.

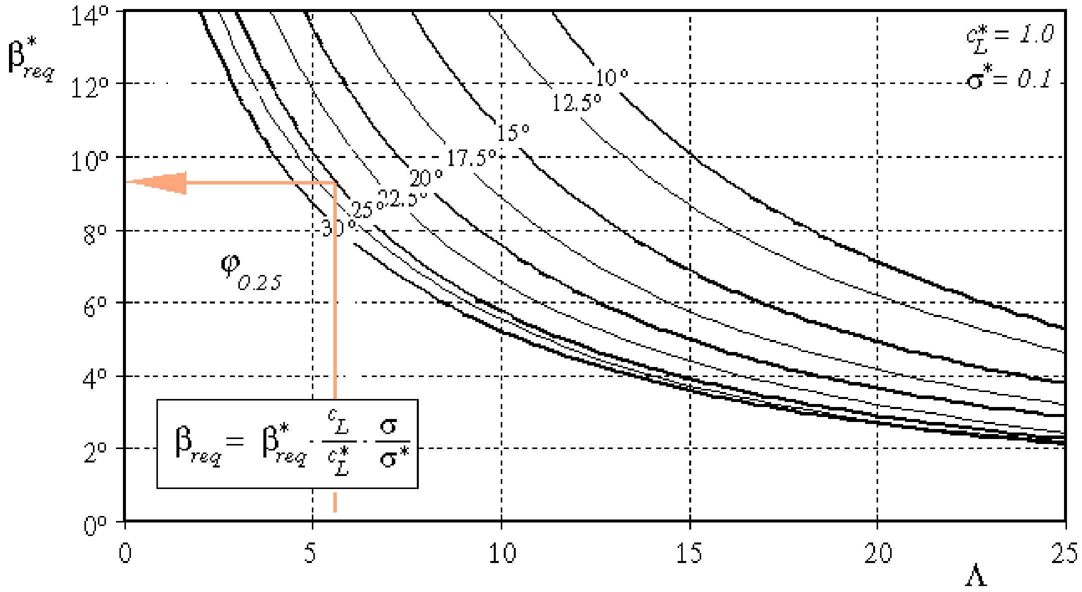

Figure 2.27: Required twist vs Aspect ratio graph with CL and stability coefficient influence [3]

From the Figure 2.27, β^*_{req} has been obtained, considering previously calculated values of Aspect Ratio and Sweep Angle.

$$\beta^*_{req} = 9.25° \tag{2.23}$$

Since the design lift coefficient and stability margin are different, this value should be corrected.

$$\beta_{req} = \beta^*_{req} \cdot \frac{C_L}{C^*_L} \cdot \frac{\sigma}{\sigma^*} = 2.31° \tag{2.24}$$

The positive required twist means a washout from the root to the tip section of 2.31°. At this point the Aerodynamic twist must be calculated, which is the difference between the zero lift angle of attack for tip and root section airfoils:

$$\beta_{\alpha 0} = \alpha_{0,t} - \alpha_{0,r} = 0.5° - (-1.04°) = 1.54° \tag{2.25}$$

Then, the mean pitching moment coefficient is calculated, since different airfoils have been used for the root and tip sections.

$$C_m = \frac{C_{m,r} + C_{m,t}}{2} = \frac{0.015 + 0.0145}{2} = 0.0148 \tag{2.26}$$

Then the twist vs aspect ratio graph is plotted, with a positive moment coefficient influence. Since C_m is between 0 and 0.015, the plot for trimmed ${C_m}^* = 0.05$ has been considered as the closest approximation. Similar to the previous graph, entering the value of aspect ratio, the required twist for the trimmed moment coefficient has been found.

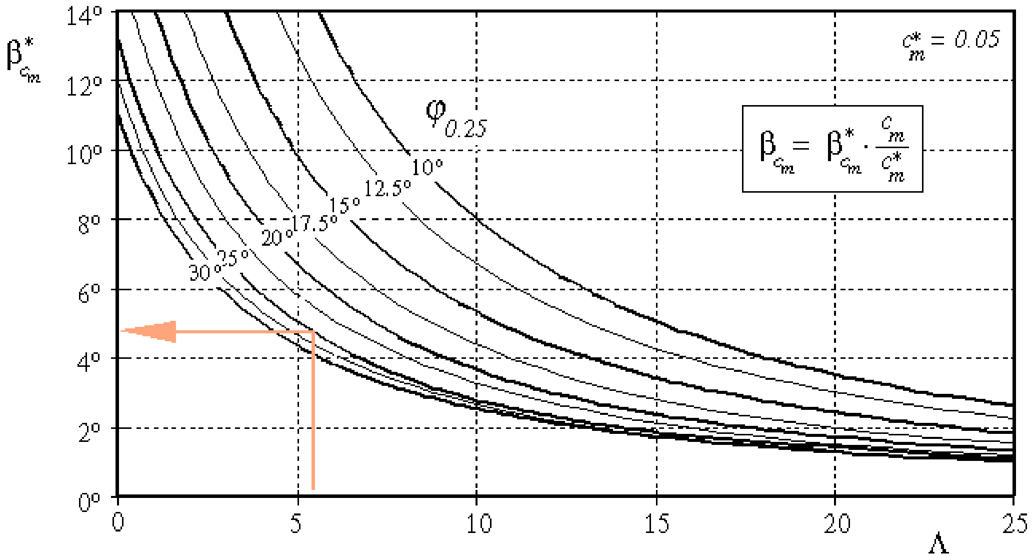

Figure 2.28: Required twist vs Aspect ratio graph with pitch moment coefficient influence [3]

$$\beta^*_{cm} = 4.75° \tag{2.27}$$

It has been corrected with the average pitching moment coefficient:

$$\beta_{cm} = \beta^*_{cm} \cdot \frac{C_m}{C^*_m} = 1.41 \tag{2.28}$$

Finally, the geometric twist which must be built between the root and the tip sections has been calculated:

$$\beta_{geo} = \beta_{req} - \beta_{\alpha 0} - \beta_{cm} = 2.31° - 1.54° - 1.41° = -0.64° \tag{2.29}$$

The negative value of the geometric twist indicates wash-in, which means that the angle of incidence must be increased from the root to the tip. The reason is that the selected airfoils already provide enough positive pitching moment, and to counter that and achieve equilibrium for the trimmed condition, the angle of incidence should be higher at the tip, providing less pitching moment and higher lift coefficient behind the neutral point.

2.4.4.3 Final design with XFLR5 software

XFLR5 software, which is dedicated to airfoil and wing analysis, has been used to check the accuracy of the analytical design and also to calibrate the center of mass, based on pitching moment plots obtained through simulations.

Since all the selected airfoils are not common ones, their corresponding aerodynamic data was missing in the XFLR5 database. Therefore, at first place Eppler186 and MH45 airfoils have been imported and analyzed (Bach Analysis), generating the missing data.

Eppler186 airfoil, which covers mainly the core of the UAV, was analyzed for Reynolds number between 200.000 and 700.000, and for Angle of attack (AoA) between -3 and 15 degrees.

MH45 airfoil was analyzed for smaller values of Reynolds, between 30.000 and 600.000, as it covers mostly the tip module where chord length is significantly reduced. The AoA values were the same as for the previous analysis.

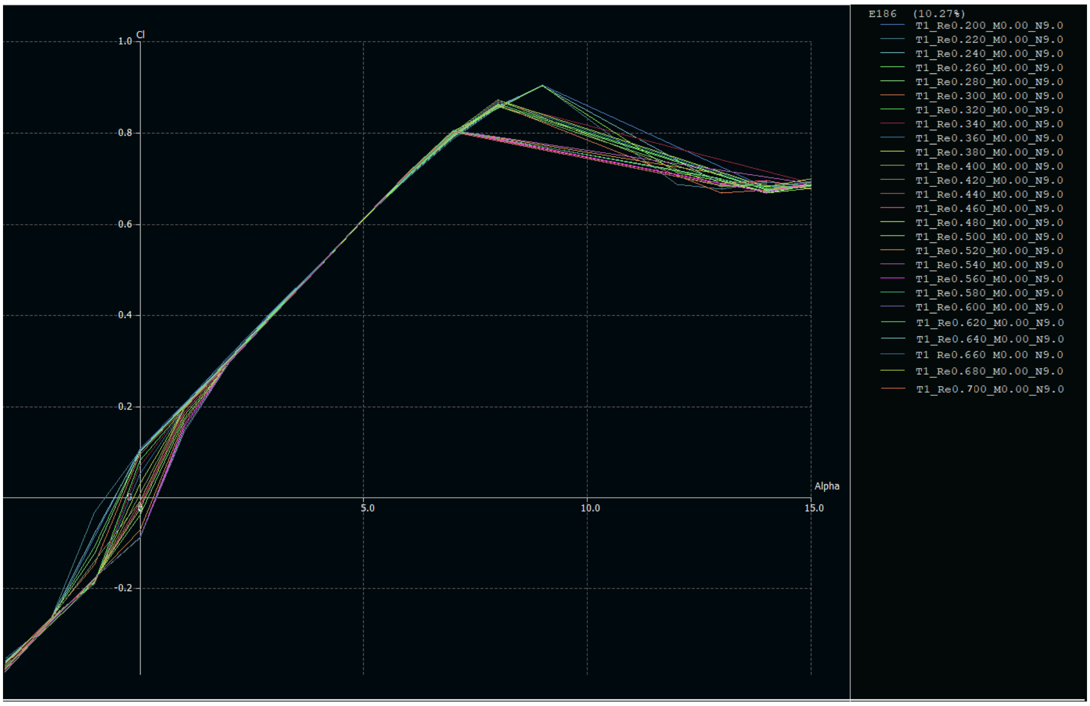

Figure 2.29: Eppler186 Cl Alpha graph for different Reynolds values, obtained from XFLR5

To validate the generated data, XFLR5 polar plots have been compared to the onesobtained from an Online Airfoil Database [16] (see Report Attachment [1]).

Then, the aircraft geometry has been defined and meshed, according to the analytical design.

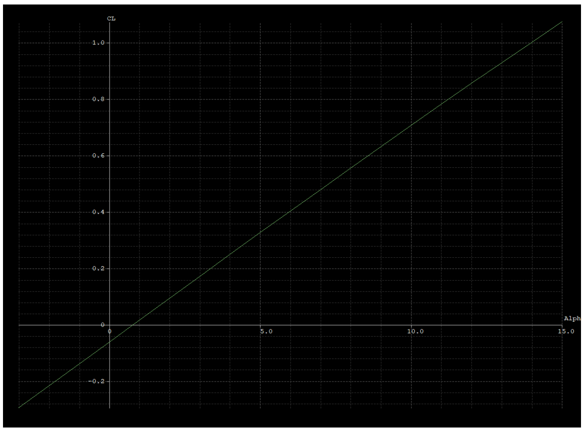

Figure 2.30: Flying wing: C_L vs α

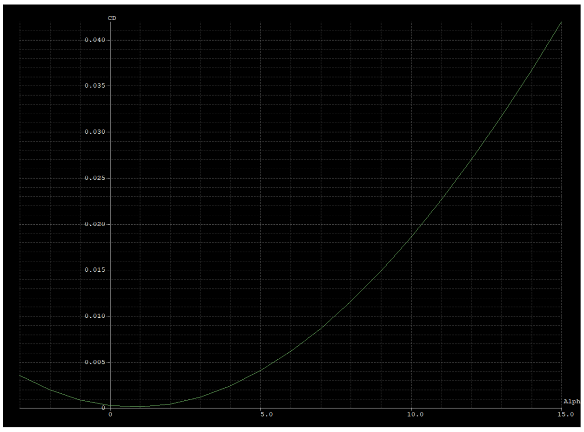

Figure 2.31: Flying wing: C_D vs α

The flying wing has been simulated for AoA between $-3°$ and $15°$, with increments of 1 °, cruise speed of 16 m/s, at an altitude of 110 m (according to the EASA UAV Draft), air density of 1.212 kg/m^3 and kinematic viscosity $\nu = 0,000014734$ m^2/s. It is important to note that the 3D panel method has been used, with Dirichlet boundary conditions. The simulation results are illustrated in the next figures:

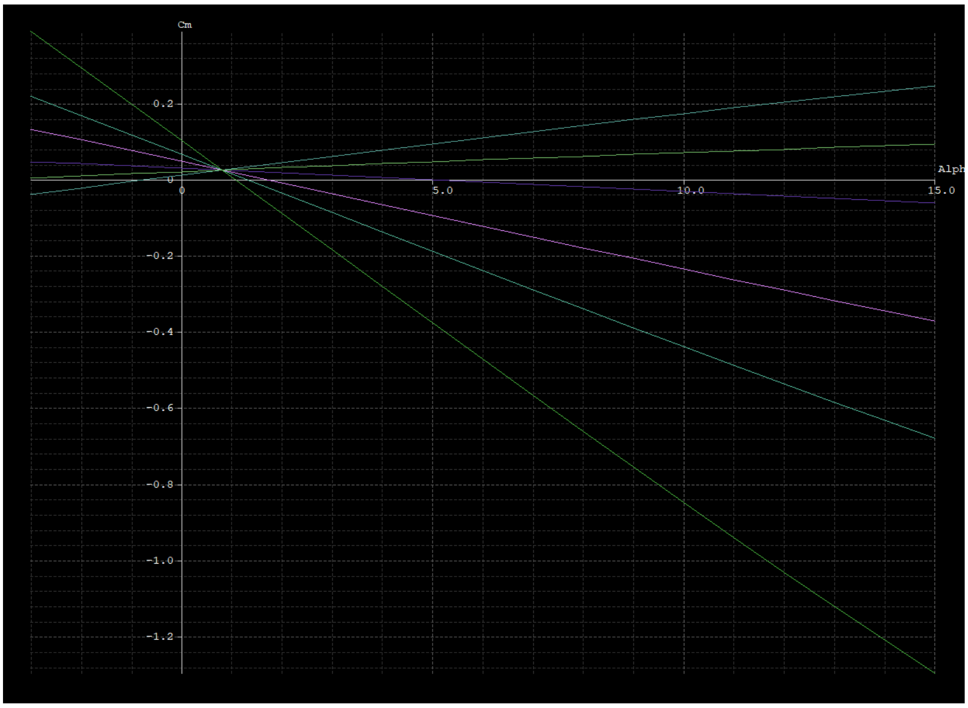

Figure 2.32: Flying wing: C_M vs α

From the previous polar plots the conclusions are:

- C_L vs α gradient is similar to the gradient of individual airfoils, and due to the finite wingspan effect, it is lower than the theoretical value of 2π.

- C_L vs α graph is accurate based on the selected airfoils. To determine the cruise flight angle of attack, next equation has been used:

$$L = W = mg = \frac{1}{2}\rho V^2 S C_{Lcruise} \tag{2.30}$$

$$C_{Lcruise} = \frac{mg}{\frac{1}{2}\rho V^2 S} = \frac{4 \cdot 9.81}{0.5 \cdot 1.212 \cdot 16^2 \cdot 1.05} = 0.2409 \tag{2.31}$$

  This means that it is possible to have a cruise flight at an angle of attack of approximately 4°, which is reasonably acceptable.

- The C_D vs α graph is not accurate, as it only accounts the induced drag (inviscid flow simulation). However, the simulation was not oriented to find exact values of aerodynamic parameters, but to verify the preliminary design. As the Ansys Fluent is going to be used for the next simulation, all these values will be corrected.

- Figure 2.32 illustrates C_M vs α plots for different positions of the center of gravity (from the nose till 0.520m). While the center of gravity is between the nose and the neutral point, the gradient of the pitching moment is negative ($\frac{dC_M}{d\alpha} < 0$), which means that the flying wing is statically stable. When the center of gravity is placed behind the neutral point, the slope is positive and the flying wing is statically unstable.

  Based on the analytical design, the neutral point was $X_N = 0.409m$, which is quite close to the simulation result (approximately 0.410 m). Also, for AoA between 0° and 5° the pitching moment coefficient is positive, which helps to "nose-up", until reaching stability.

  Another important point is to select a configuration where the pitching moment gradient is negative, but not pronounced. From the pitching moment plot, the dark violet series (for $X_{CG} = 0.4\ m$) seems to be the most adequate one for a flying wing.

The lift distribution along the wingspan for an angle of attack of 4° is illustrated in Figure 2.33. It is important to note the relatively high values of lift coefficients at the root module, achieved by the smooth transition of airfoils from root to tip and also due to the blended wing-body design. This has a positive impact from structural point of view.

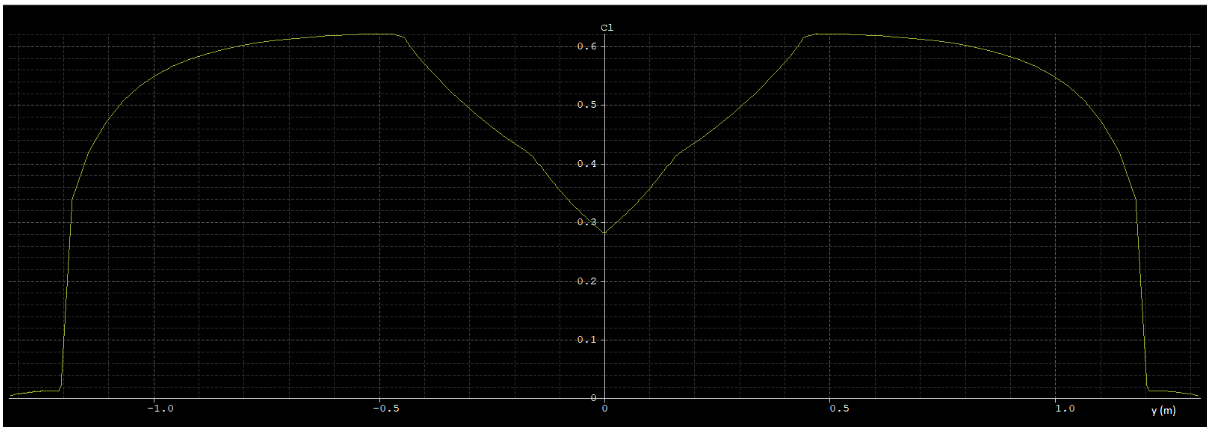

Figure 2.33: CL distribution for Alpha = 4

2.4.5 Numerical Simulation by CFD

The 3D model designed in CATIA has been imported to ANSYS Fluent Workbench, with the goal of obtaining C_L, C_D and C_M graphs versus a range of angles of attack.

2.4.5.1 Simulation method and parameters

To determine the correct set of meshing parameters, three different simulations have been launched, keeping the same angle of attack and changing the meshing parameters. Two main factors have been considered regarding those simulations:

- Simulation run-time.
- Results accuracy and variance.

Then, the best set of meshing parameters has been defined as a combination of less resource-consumption and similar results accuracy (see Report Attachment [1]). Then, the geometry has been meshed accordingly, and boundary conditions were set. Ansys Workbench offers a variety of viscous-laminar simulation models, such as Laminar, k-epsilon and k-omega. The first one has been chosen, as the Reynolds number is low.

2.4.5.2 Simulation results

A Fluent simulation provides a solution for a given inlet velocity and geometry. Therefore, to get aerodynamic polar plots, different simulations should be launched, varying the inlet velocity vector components, to create an effective angle of attack regarding the longitudinal axis of the fuselage. This method allows to keep the same geometry axis system throughout simulations, avoiding the need of meshing for each AoA. Thus, only the inlet velocity field is changed. After simulating for α between -10° *and* 17° (see Report Attachment [1]), Table 2.9 has been populated, based on which the following aerodynamic polar curves of Lift coefficient, Drag coefficient and Pitching moment coefficient have been obtained.

$\alpha (deg)$	C_L	C_D	C_M
-10	-0.5759	0.1054	0.8800
-9	-0.6128	0.0867	0.8211
-8	-0.6228	0.0703	0.7517
-7	-0.5668	0.0560	0.6814
-6	-0.4905	0.0455	0.6351
-5	-0.4077	0.0345	0.6015
-4	-0.3271	0.0204	0.5662
-3	-0.2430	0.0130	0.5155
-2	-0.1623	0.0111	0.4814
-1	-0.0680	0.0082	0.4164
0	0.0215	0.0079	0.3458
1	0.1068	0.0084	0.2998
2	0.1872	0.0088	0.2598
3	0.2697	0.0108	0.1998
4	0.3691	0.0145	0.1401
5	0.4501	0.0191	0.0818
6	0.5382	0.0257	0.0350
7	0.6181	0.0357	-0.0006
8	0.6988	0.0441	-0.0256
9	0.7777	0.0529	-0.0506
10	0.8577	0.0621	-0.0756
11	0.9298	0.0702	-0.1006
12	0.9981	0.0800	-0.1256
13	1.0577	0.0930	-0.1506
14	1.0930	0.1101	-0.1756
15	1.0658	0.1307	-0.1986
16	1.0010	0.1475	-0.2304
17	0.9260	0.1671	-0.2669

Table 2.9: Aerodynamic coefficients obtained from Fluent Simulation

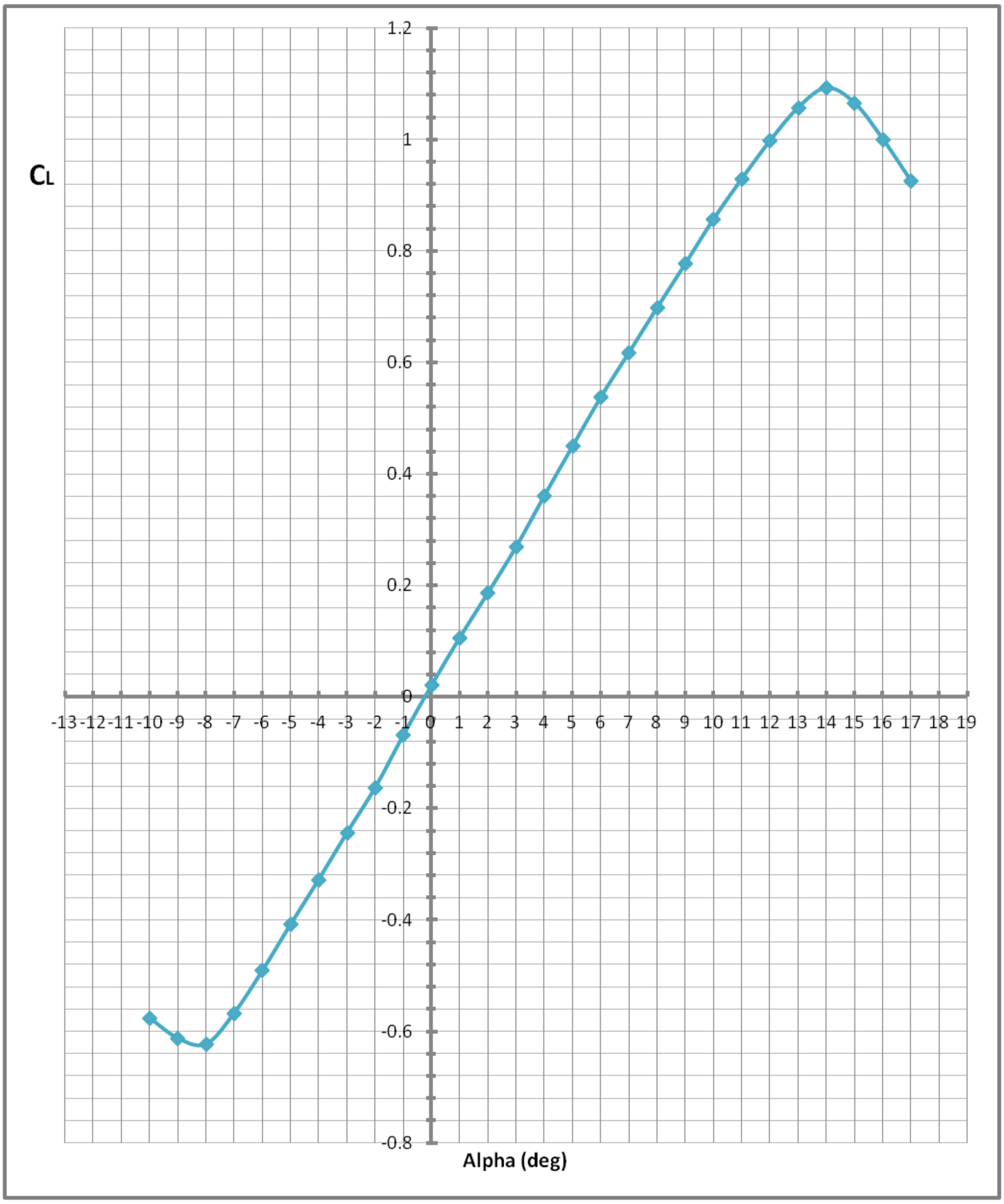

Figure 2.34: Lift coefficient vs AoA

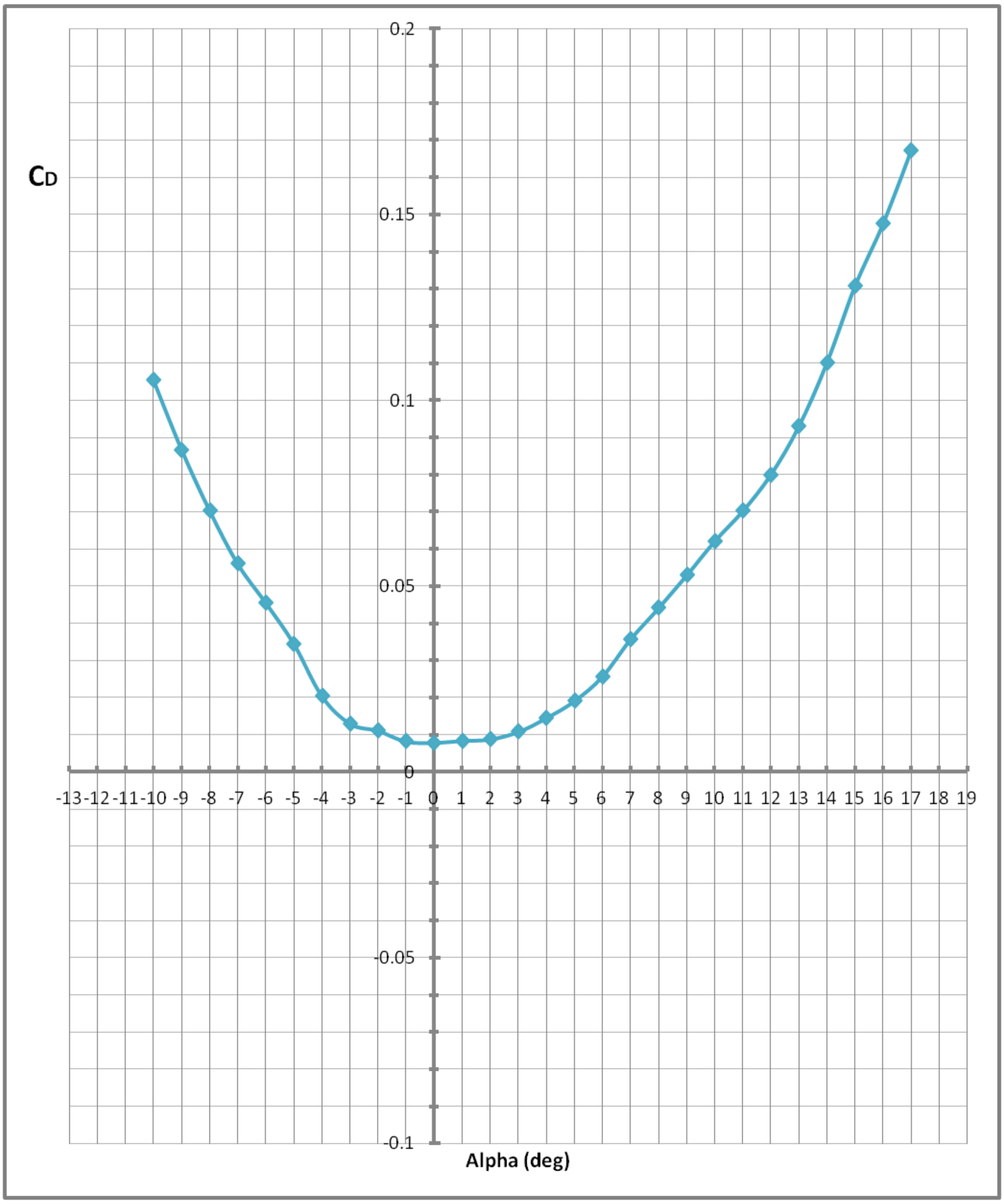

Figure 2.35: Drag coefficient vs AoA

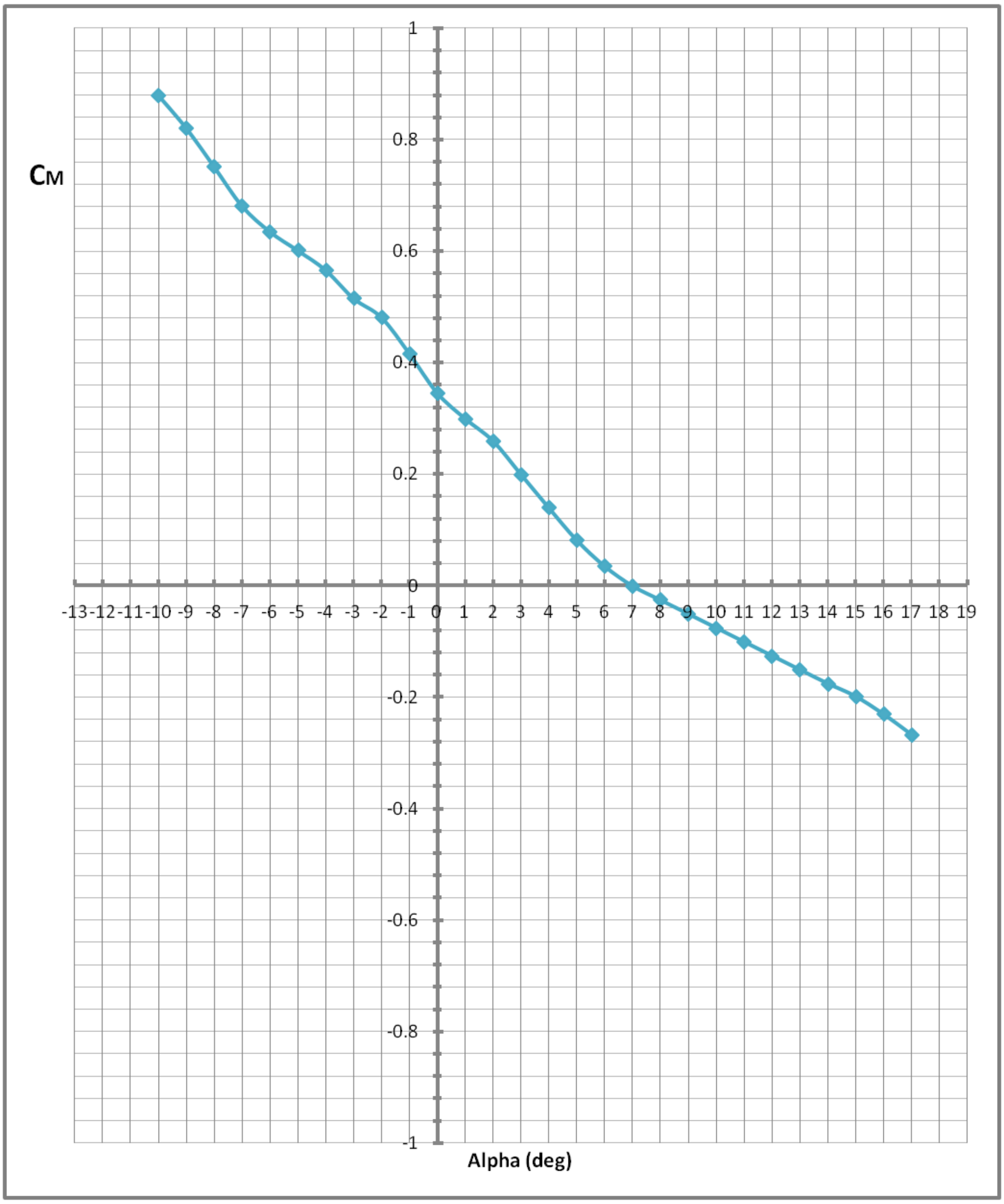

Figure 2.36: Pitch moment coefficient vs AoA

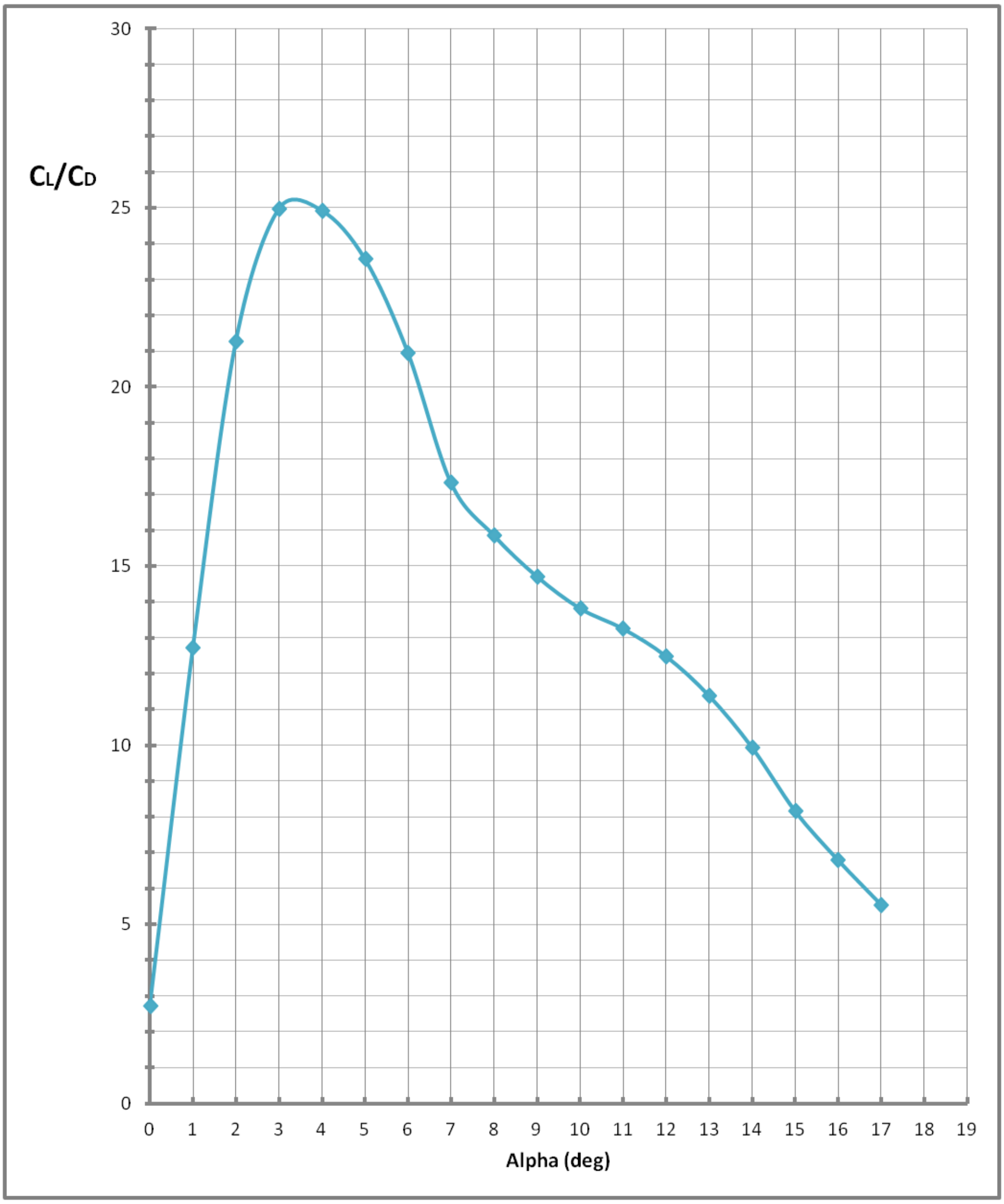

Figure 2.37: Lift to Drag ratio vs AoA

2.4.5.3 XFLR5 versus CFD comparison

At this point, it is interesting to compare simulation results obtained by XFLR5 and CFD software.

Regarding C_L versus α, CFD provides reasonably more precise results, given the fact that the simulation was done with laminar flow model, while the XFLR5 simulation involved inviscid flow model (due to convergence problems). However, C_L versus α gradient is similar between -5°and 10°. As expected, XFLR5 is not precise beyond 10° since it ignores flow separation and stall.

Regarding C_D versus α, CFD also offers a complete analysis in contrast with XFLR5, which only provides the induced drag component.

XFLR5 software, however, offers valuable information regarding pitching moment coefficient. As the CFD simulation is more time-consuming, it is less straightforward to do multiple simulations varying aircraft's center of gravity position. Hence, only one case has been simulated with Ansys CFD (for $X_{CG} = 0.4\ m$). On the other hand, XFLR5 C_M versus α plots for different positions of center of gravity are accurate source to be discretized and used numerically for the flight controller.

The main conclusion is, that both software provide useful information, depending on depth of analysis and goal.

2.4.6 Flight Envelope Diagram

The definition of the flight envelope diagram is an important process which determines the operational conditions based on the aircraft properties and the legislation framework. There are two main applications of the flight envelope:

- It can be used as a guideline for structural design, since it determines speed limits and load factors.
- It can be used as a guideline for the operator (pilot, controller, etc.), since it provides information regarding operational limits.

The combined V - n diagram is constructed in three steps:

- Basic V – n diagram
- Gust V – n diagram
- Combined V – n diagram

The Figure 2.38 illustrates the general form of a V–n diagram. The following table summarizes flight conditions used for the definition of the flight envelope.

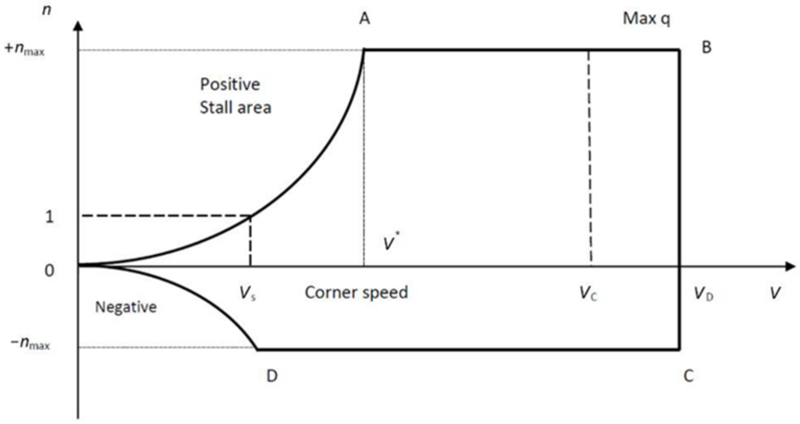

Figure 2.38: Flight envelope V–n diagram general shape [12]

Parameter name	Symbology	Parameter value
Vehicle Mas	m	4 kg
Wing Gross Area (recalculated)	S_{wga}	1.05 m^2
Maximum Lift Coefficient (positive)	C_{Lmax+}	1.093
Maximum Lift Coefficient (inverted flight)	C_{Lmax-}	0.623
Aspect Ratio	AR	5.5
Lift-curve slope $\frac{dc_L}{d\alpha}$	a	4.7746 rad^{-1}
Design Stall Speed	V_s	9.63 m/s
Cruise Speed	V_c	16 m/s
Maximum Speed at Sea level	V_{maxSL}	21.0 m/s
Sea level Gravitational Acceleration	g_0	9.81 m/s^2
Cruise Gravitational Acceleration	g_c	9.81 m/s^2
Sea level air density	ρ_o	1.225 kg/m^3
Cruise level air density	ρ_c	1.212 kg/m^3

Table 2.10: Flight conditions

2.4.6.1 Basic V–n Diagram

The load factor is given by the next equation:

$$n = \frac{L}{W} \tag{2.32}$$

According to the Legislation framework analysis [12], the cruise speed minimal value should be:

$$V_c = 2.4 \cdot \sqrt{\frac{mg}{S}} = 2.4 \cdot \sqrt{\frac{4 \cdot 9.81}{1.05}} = 14.67m/s \tag{2.33}$$

Since the design cruise speed of 16 m/s meets this requirement, it will be considered as the final cruise speed for the following calculations. The maximum speed is given by the next equation:

$$V_{maxSL} = 1.3 \cdot V_c = 20.8m/s \tag{2.34}$$

The aircraft dive speed is:

$$V_D = 1.4 \cdot V_c = 22.4m/s \tag{2.35}$$

According to the Legislation framework, the load limits are:

$$n_{max+} = 4.0$$

$$n_{max-} = -2.0$$

Therefore, the coordinates for the points B and C are:

$$B(V_D,\ n_{max+}) = (22.4,\ 4.0)$$

$$C(V_D,\ n_{max-}) = (22.4,\ -2.0)$$

For steady flight, where the load factor n is 1, the general equation for the stall speed is:

$$V_s = \sqrt{\frac{2mg}{\rho S C_{Lmax+}}} = \sqrt{\frac{2 \cdot 4 \cdot 9.81}{1.212 \cdot 1.05 \cdot 1.093}} = 7.51 m/s \tag{2.36}$$

This determines the point $F(7.51,\ 1.0)$

For steady inverted flight, where the load factor n is -1, the stall speed is:

$$V_{sinv} = \sqrt{\frac{-2mg}{\rho S C_{Lmax-}}} = \sqrt{\frac{-2 \cdot 4 \cdot 9.81}{1.212 \cdot 1.05 \cdot (-0.623)}} = 9.95 m/s \tag{2.37}$$

This determines the point $E(13.24,\ -1.0)$

The upper curve for positive load factor versus speed can be defined as:

$$n = \frac{L}{W} = \frac{0.5 \rho {V_s}^2 S C_{Lmax+}}{W} = \frac{0.5 \cdot 1.212 \cdot {V_s}^2 \cdot 1.05 \cdot 1.093}{4 \cdot 9.81} = 0.017724 \cdot {V_s}^2 \tag{2.38}$$

The intersection of the upper curve with a horizontal line at load factor equal to 4 gives the point A x-coordinate, which is also called the maneuvering speed:

$$V_s = \sqrt{\frac{n}{0.017724}} = \sqrt{\frac{4}{0.017724}} = 15.02 m/s \tag{2.39}$$

The coordinates of the point A are $(15.02,\ 4.0)$

In a similar way, the equation for the lower curve is calculated:

$$n = \frac{L_{inv}}{W} = \frac{0.5 \rho {V_{s\,inv}}^2 S C_{Lmax-}}{W} = \frac{0.5 \cdot 1.212 \cdot {V_{s\,inv}}^2 \cdot 1.05 \cdot (-0.623)}{4 \cdot 9.81} = -0.010102 {V_{s\,inv}}^2 \tag{2.40}$$

$$V_{s\,inv} = \sqrt{\frac{n}{-0.005706}} = \sqrt{\frac{-2}{-0.010102}} = 14.07\ m/s \tag{2.41}$$

The coordinates of the point D are $(14.07,\ -2.0)$

Since the points A, B, C, D, E, F and the upper and lower curves are known, the basic V–n diagram can be traced (Figure 2.39).

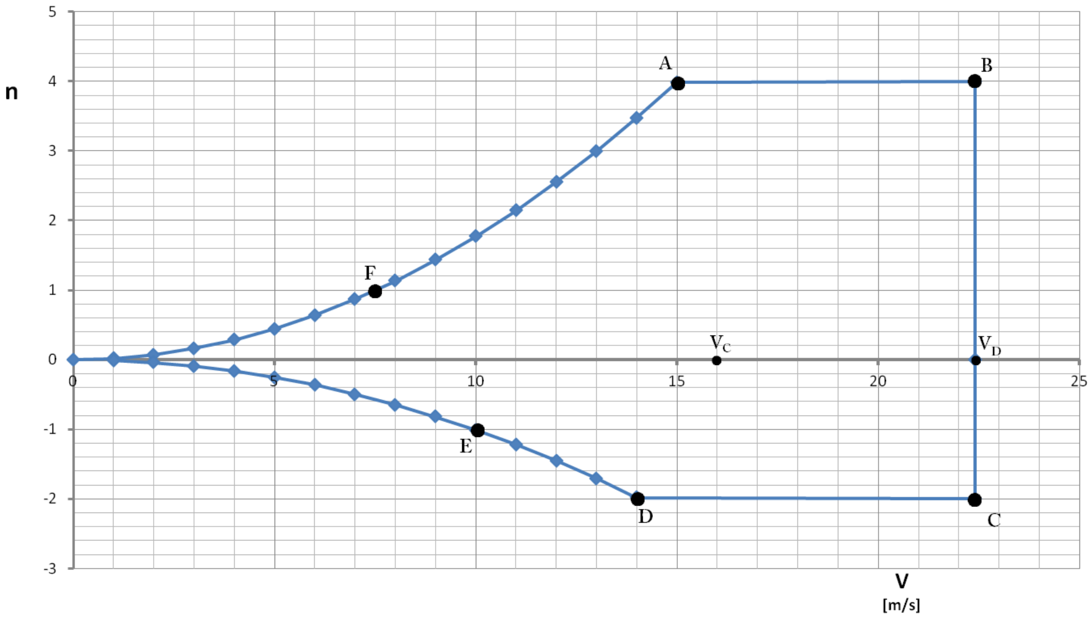

Figure 2.39: Basic V–n flight envelope diagram

2.4.6.2 Gust V–n Diagram

According to the normative [12], the equation of the load factor variation as a function of the airspeed is:

$$n = 1 + \frac{K_g \cdot V_{ge} \cdot V_e \cdot a \cdot \rho \cdot S_{wga}}{2W} \tag{2.42}$$

According to CS-VLA 333, the gust diagram is calculated for positive upward gusts and negative downward gusts for the cruise speed V_c and dive speed V_D. The gust speed is statistically measured. For the dive speed it is considered equal to 7.62 m/s and for the cruise speed: 15.24 m/s.

At first place, the load factor for gusts has been calculated at 110 m. The wing mean geometric chord is given by the next expression:

$$C_{mgc} = \frac{S_{wga}}{b} = 0.4375\ m \tag{2.43}$$

The vehicle mass aspect ratio, according to the normative [12], is given by:

$$\mu_g = \frac{2 \cdot m}{\rho \cdot C_{mgc} \cdot a \cdot S_{wga}} = \frac{2 \cdot 4}{1.212 \cdot 0.4375 \cdot 4.7746 \cdot 1.05} = 3.01 \tag{2.44}$$

The gust alleviation factor is:

$$K_g = \frac{0.88\mu_g}{5.3 + \mu_g} = 0.3187 \tag{2.45}$$

Then, the gust load factor has been calculated:

$$n = 1 + \frac{0.3187 \cdot (\pm 15.24) \cdot V_c \cdot 4.7746 \cdot 1.212 \cdot 1.05}{2 \cdot 4 \cdot 9.81} = 1 \pm 0.3760 V_c$$

From the equation above:

$$n_{g+} = 1 + 0.3760 \cdot 16.00 = 7.02$$

$$n_{g-} = 1 - 0.3760 \cdot 16.00 = -5.02$$

Proceeding the same way for the dive speed:

$$n = 1 + \frac{0.3187 \cdot (\pm 7.62) \cdot V_D \cdot 4.7746 \cdot 1.212 \cdot 1.05}{2 \cdot 4 \cdot 9.81} = 1 \pm 0.1880 V_D$$

The gust load factors for dive speed are:

$$n_{g+} = 1 + 0.1880 \cdot 22.40 = 5.21$$

$$n_{g-} = 1 - 0.1880 \cdot 22.40 = -3.21$$

Then, the load factor has been recalculated for sea level conditions. The gust load factor for the cruise speed at sea level is:

$$n = 1 + \frac{0.3167 \cdot (\pm 15.24) \cdot V_c \cdot 4.7746 \cdot 1.225 \cdot 1.05}{2 \cdot 4 \cdot 9.81} = 1 \pm 0.3777 V_c$$

$$n_{g+} = 1 + 0.3777 \cdot 16.00 = 7.04$$

$$n_{g-} = 1 - 0.3777 \cdot 16.00 = -5.04$$

The gust load factor for the dive speed at sea level is:

$$n = 1 + \frac{0.3167 \cdot (\pm 7.62) \cdot V_D \cdot 4.7746 \cdot 1.225 \cdot 1.05}{2 \cdot 4 \cdot 9.81} = 1 \pm 0.1889 V_D$$

$$n_{g+} = 1 + 0.1889 \cdot 22.40 = 5.23$$

$$n_{g-} = 1 - 0.1889 \cdot 22.40 = -3.23$$

Gust load factors are higher at sea level than at 110 m. The Figure 2.40 represents gust load factor versus velocity graphs.

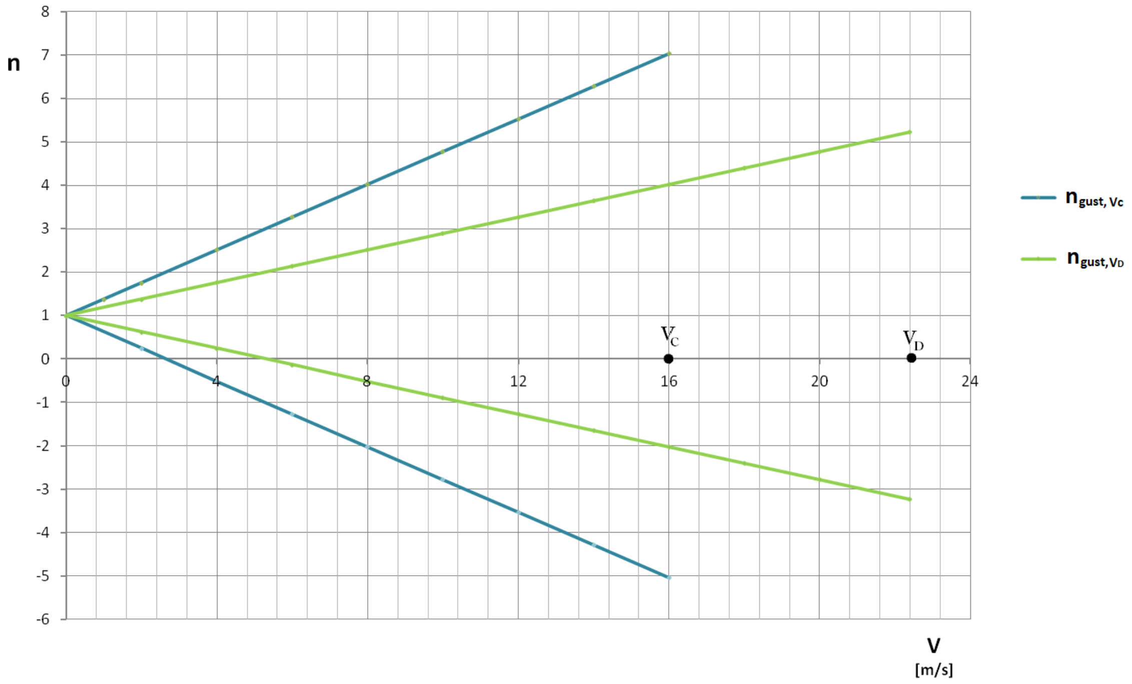

Figure 2.40: Gust load factor vs speed diagram

2.4.6.3 Combined V–n Diagram

The combined V-n diagram has been obtained from the basic diagram and gust line intersection points, according to the CS-VLA guide (see Figure 2.41). The analysis of the flight envelope shows that gust loads should be considered for the structural design, since they are higher than the basic maneuver loads. It is important to note that some small scale aircraft of low mass aspect ratio are simply transferred by the gusts and they rather get any noticeable load change on the structure. This can be seen as an advantage when it comes to the structural design, but the drawback lies in loss of control. The current model however, has enough mass aspect ratio to withstand the gusts. Therefore, more emphasis has been done on the structural design, considering load factors of 7.04 and -5.04.

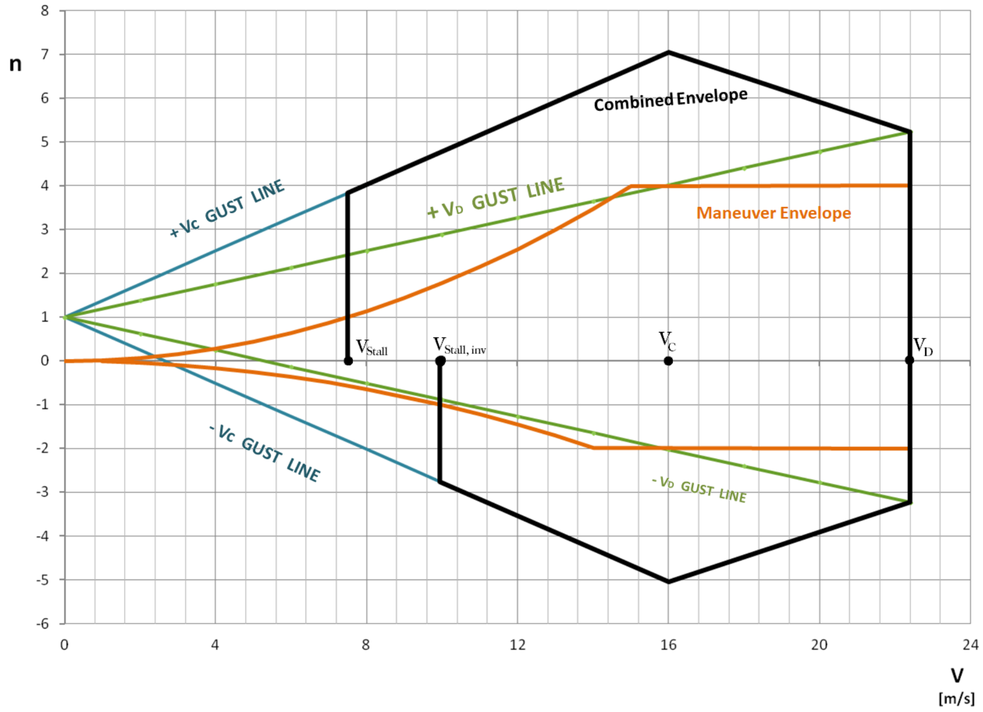

Figure 2.41: Flight Envelope, the combined V–n diagram

2.4.7 Loads

The maximum take off weight of the flying wing is set to 4 kg, from which only 1.3 kg are dedicated to the airframe. From the total weight, 0.65 kg correspond to the systems components, and 1.8 kg are dedicated to the drive, including the motor, the batteries and the speed controller. The payload, which normally consists of additional sensors and cameras (depending on the mission), is around 0.25 kg.

The loads diagram is represented for the cruise flight condition, where the load factor is 1. The weight distribution is divided into four groups:

- The Structural weight (1.3 kg) includes all the airframe weight. Since the thickness and the chord distributions have higher values close to the root section, the structural weight also changes along the wingspan. Also, the location of the Roll Control System and the Pitch Control System affect on the airframe weight distribution, since they include rails and boxes, as described at the Control System Report Attachment. Simplifying the airframe weight distribution, it can be divided into three parts:
  - For the wing tips, $-1200mm < y < 450mm$ and $450mm < y < 1200mm$, the weight distribution is $w_S(y) = w_1 = -3.5425N/m$.

  - For the wing center, $-450mm < y < -150mm$ and $150mm < y < 450mm$, the weight distribution is $w_s(y) = 2 \cdot w_1 = -7.085N/m$.
  - For the root, $-150mm < y < 150mm$, the weight distribution is $w_S(y) = 3 \cdot w_1 = -7.085N/m$.

- The Drive weight is divided into two parts: the weight of the batteries (1.5kg) w_{D1}, and the weight of the motor with the speed controller (0.3kg) w_{D2}.
  - For the Roll Control System, $-450mm < y < 450mm$, the weight distribution is $w_{D1} = -16.35N/m$. The total mass of the drive batteries is 1.5kg.
  - The motor and the speed controll are fixed inside a cilinder, centered at the symmetry plane of the aircraft. Therefore, for $-60mm < y < 60mm$ the weight distribution is $w_{D1} = -24.525N/m$.
- The System components weight, w_{sys}, is attached to the Pitch Control System. For $-150mm < y < 150mm$, the correspondent distributed weight is $w_{sys} = -21.26N/m$.
- The Payload is located between $y = -150mm$ and $y = 150mm$, and the correspondent distributed weight is $w_{PL} = -8.18N/m$.

The total weight distribution is represented in Figure 2.47. The lift distribution is obtained from the XFLR5 simulation, which is explained at the Aerodynamics Report Attachment.
The next figure represents the distribution of all the above mentioned forces.

Since the aircraft is at cruise conditions, the next equations can be used:

$$\sum F_x = 0 \tag{2.46}$$

$$\sum F_y = 0 \tag{2.47}$$

$$\sum F_z = 0 \tag{2.48}$$

$$\sum M_x = 0 \tag{2.49}$$

$$\sum M_y = 0 \tag{2.50}$$

$$\sum M_z = 0 \tag{2.51}$$

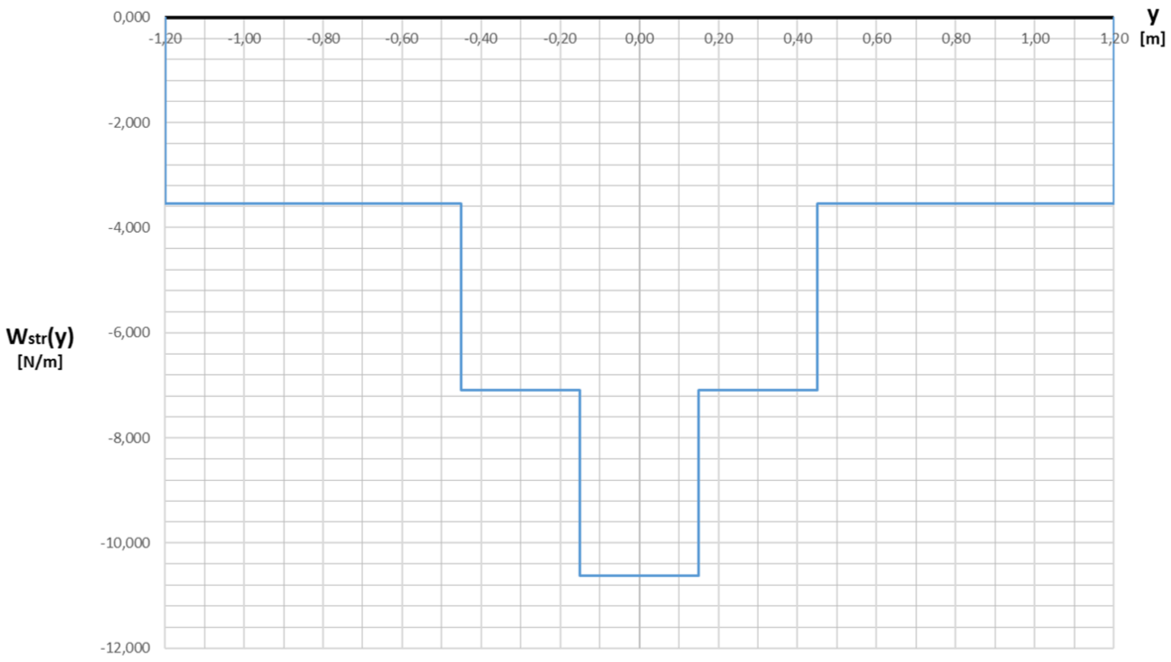

Figure 2.42: Structural Weight distribution along wingspan

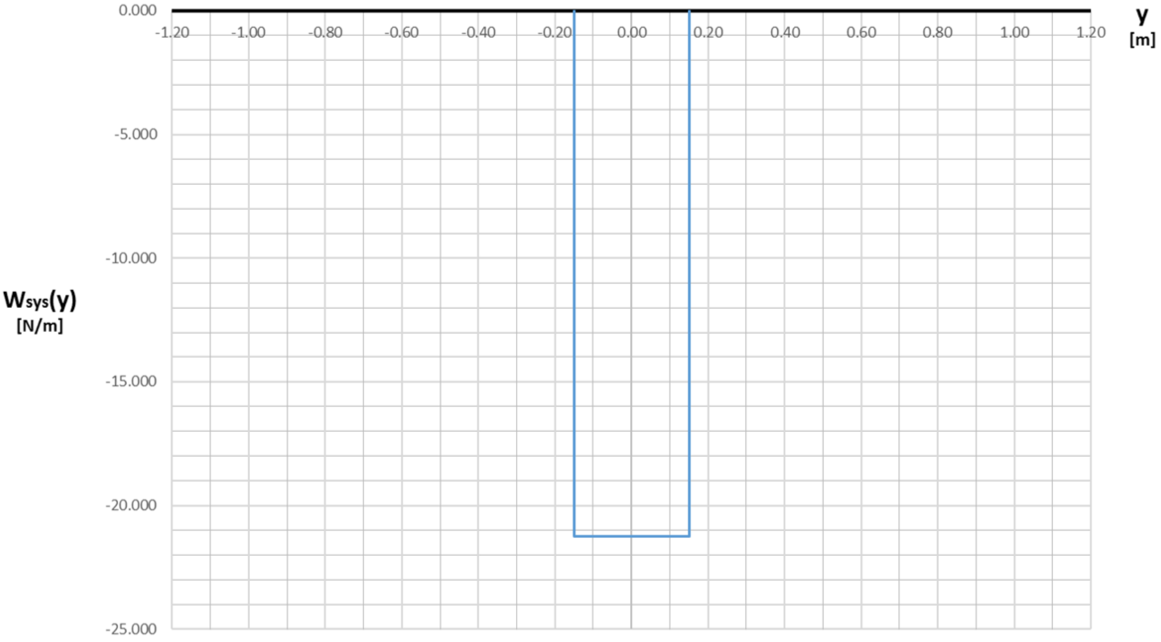

Figure 2.43: Systems Weight distribution along wingspan

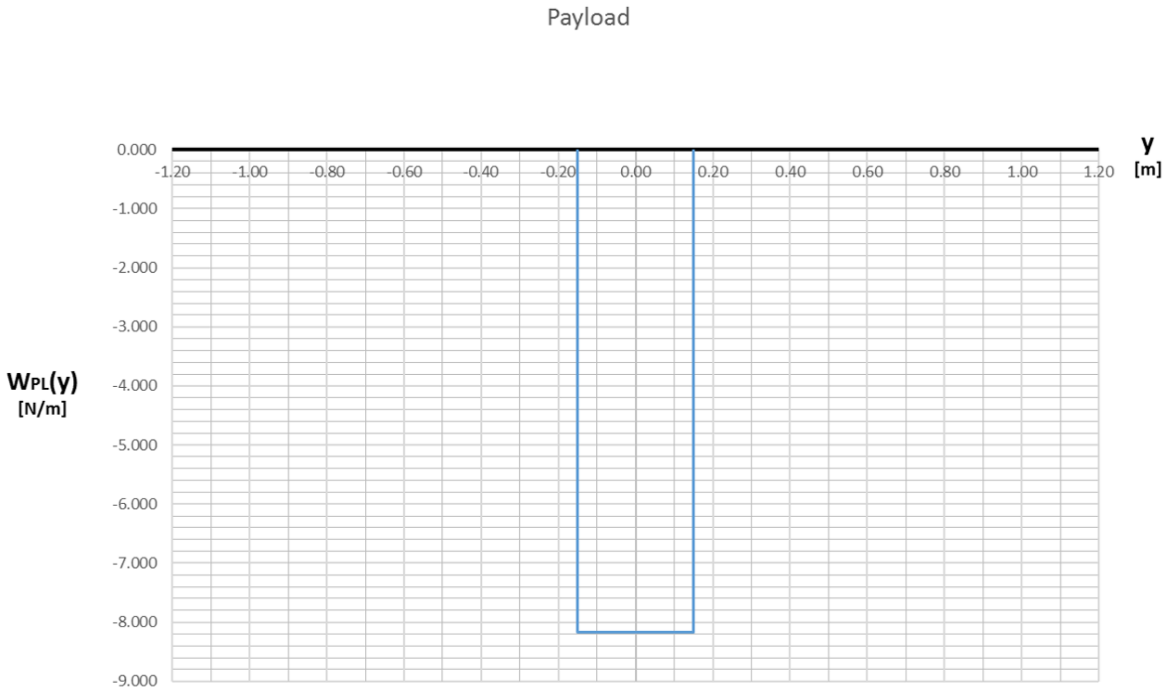

Figure 2.44: Payload distribution along wingspan

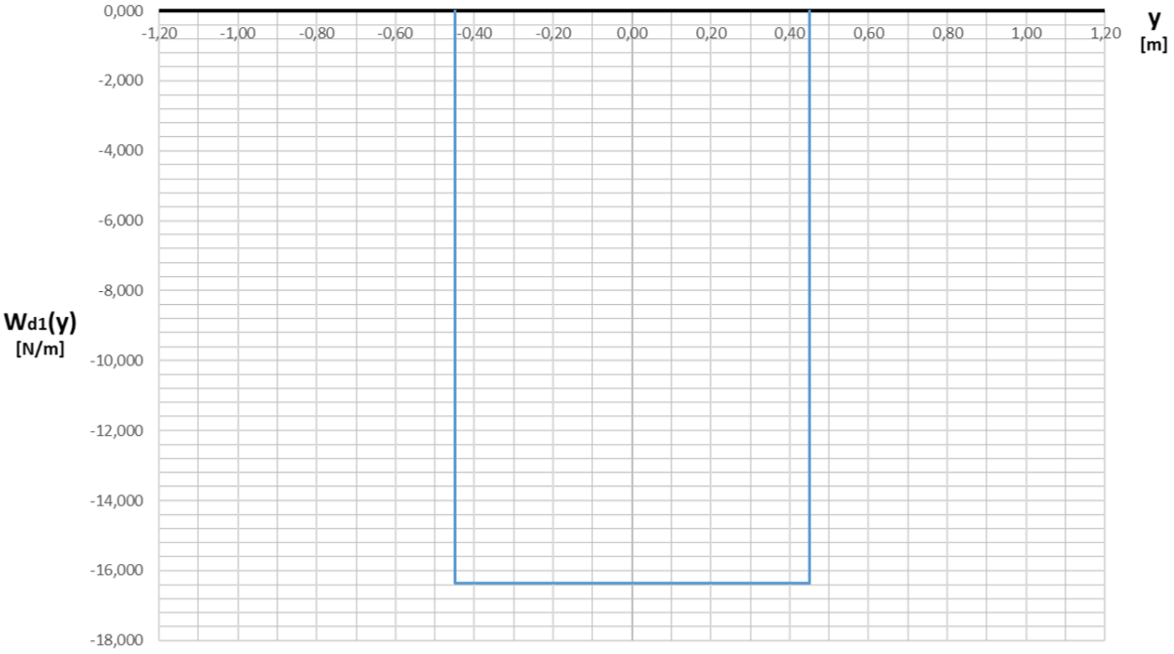

Figure 2.45: Drive - Battery weight distribution along wingspan

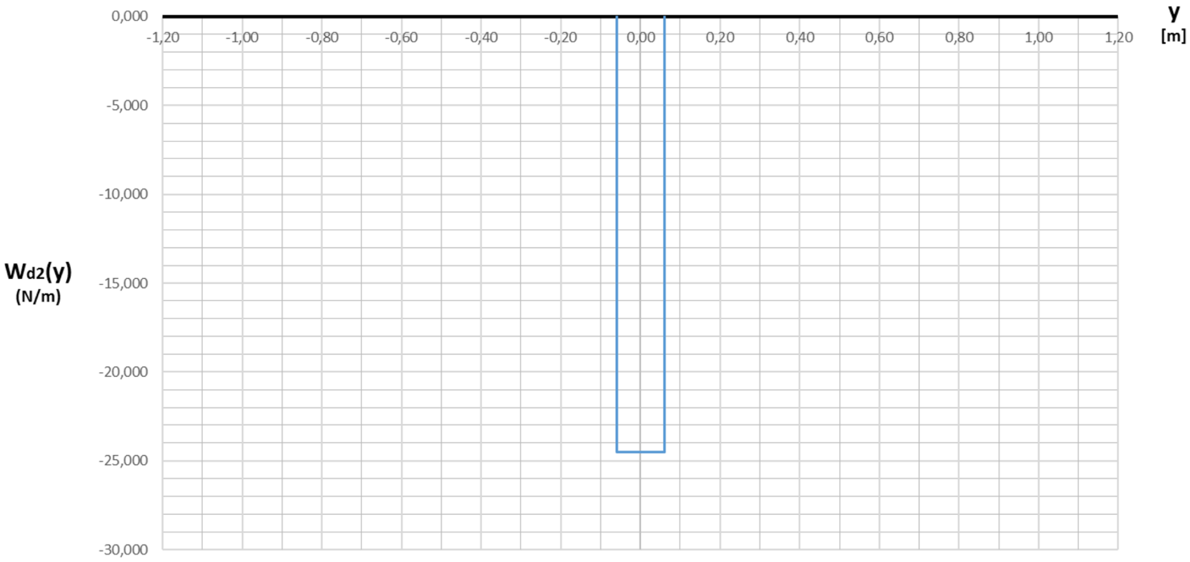

Figure 2.46: Drive - Motor weight distribution along wingspan

Combining load distribution with the previous equations the next table and graph are obtained.

From the previous study of the legislation framework, the maximum and minimum load factor values were obtained, which are 7.04 and -5.04 respectively. Applying the maximum load factor to the previous diagram gives the highest load distribution that the airframe should withstand.

This results are used in the next steps for the Shear and Moment diagrams calculation.

2.4.8 Shear and Moments Diagrams

Analyzing the final load diagram (including the load factor of 7.04), it is possible to obtain the Shear forces and moments that each section of the spars should withstand. The calculation has been done by numerical integration. The next figures represent the Shear and Moment Diagrams

According to the Shear Force Diagram, the maximum Shear force values are at the spanwise locations corresponding to $y = -0.450m$ and $y = 0.450m$. The maximum Shear Force at load factor of 7.04g is approximately:

$$Q_{z_{max}} = 78.8128\ N$$

From the Bending Moment Diagram,the most critical section is located at the center line

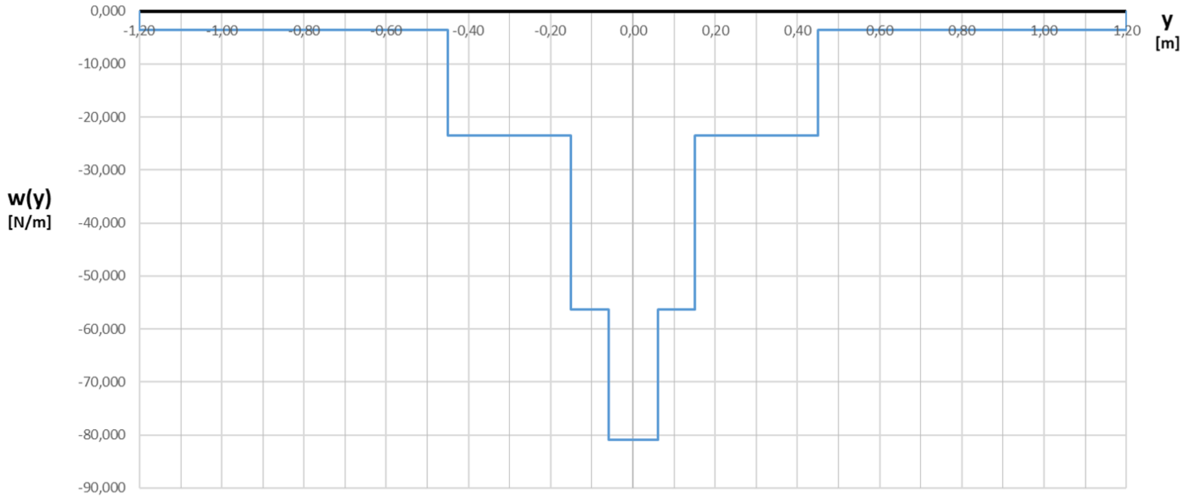

Figure 2.47: Total Weight distribution along wingspan

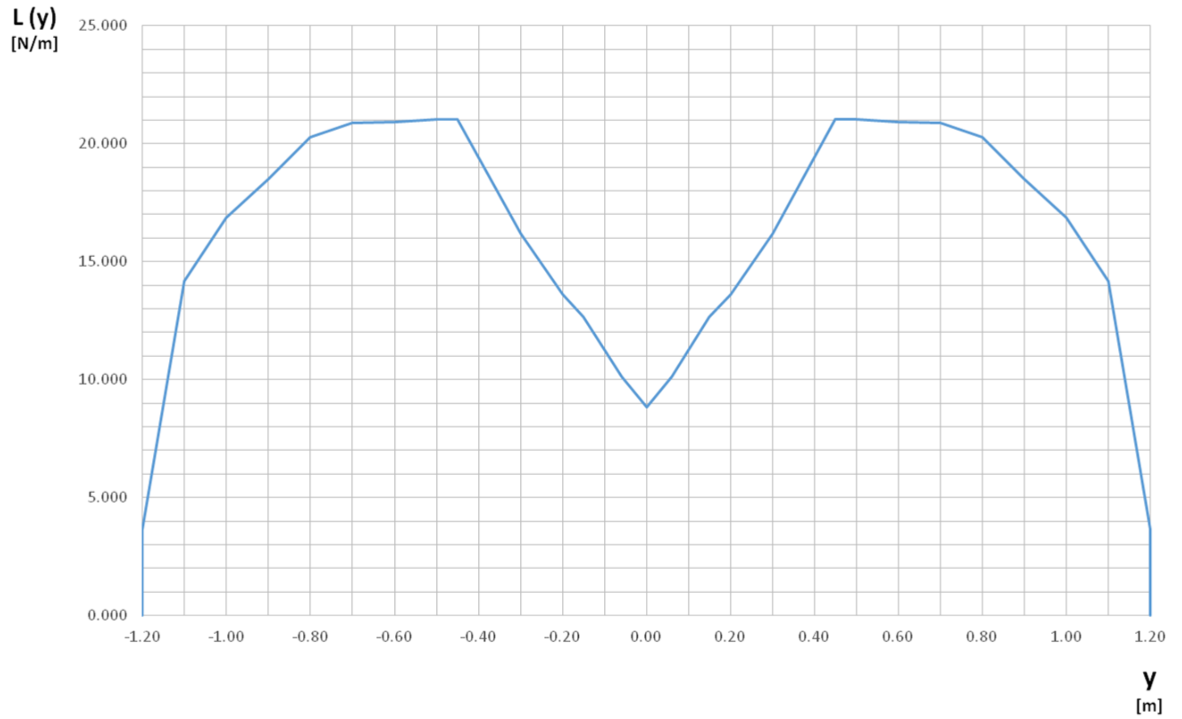

Figure 2.48: Lift distribution along wingspan

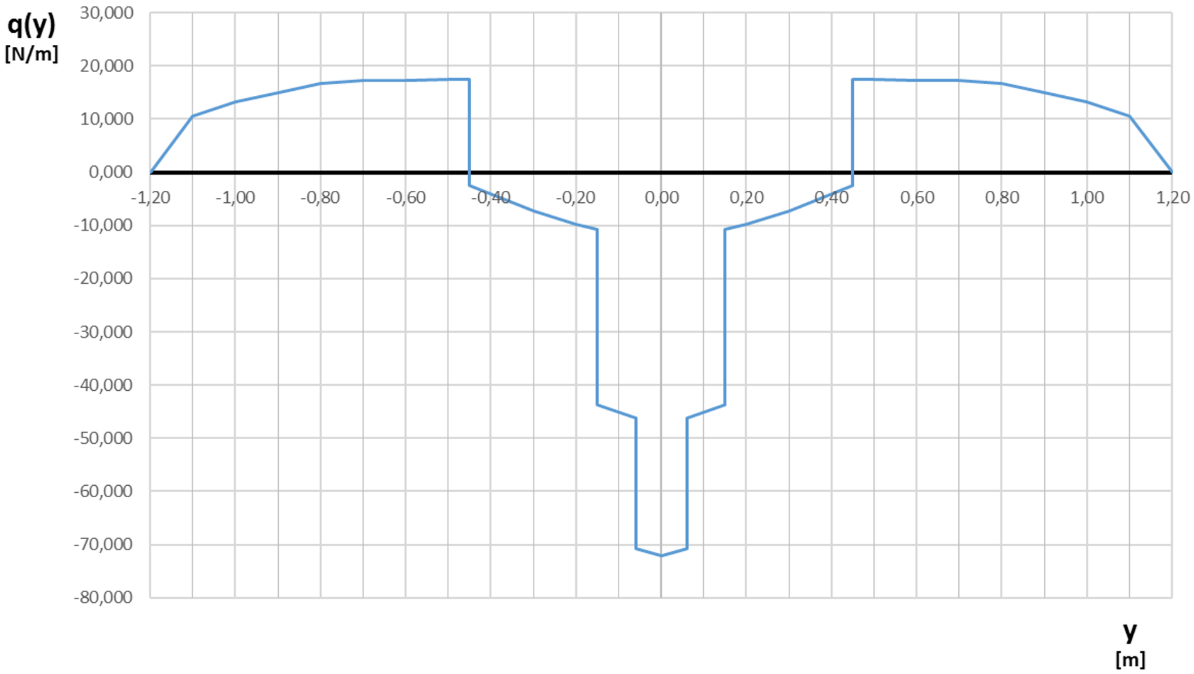

Figure 2.49: Total load distribution along wingspan for load factor 1g

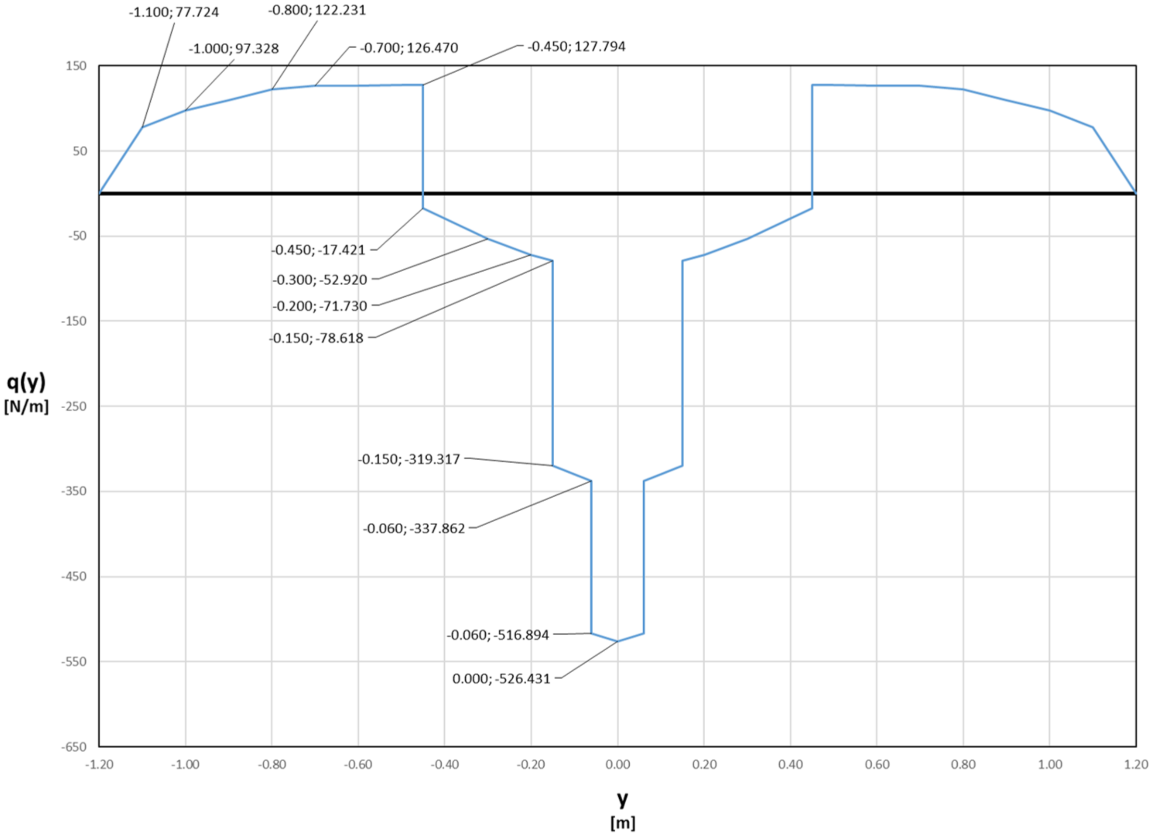

Figure 2.50: Total load distribution along wingspan for maximum load factor 7.04g

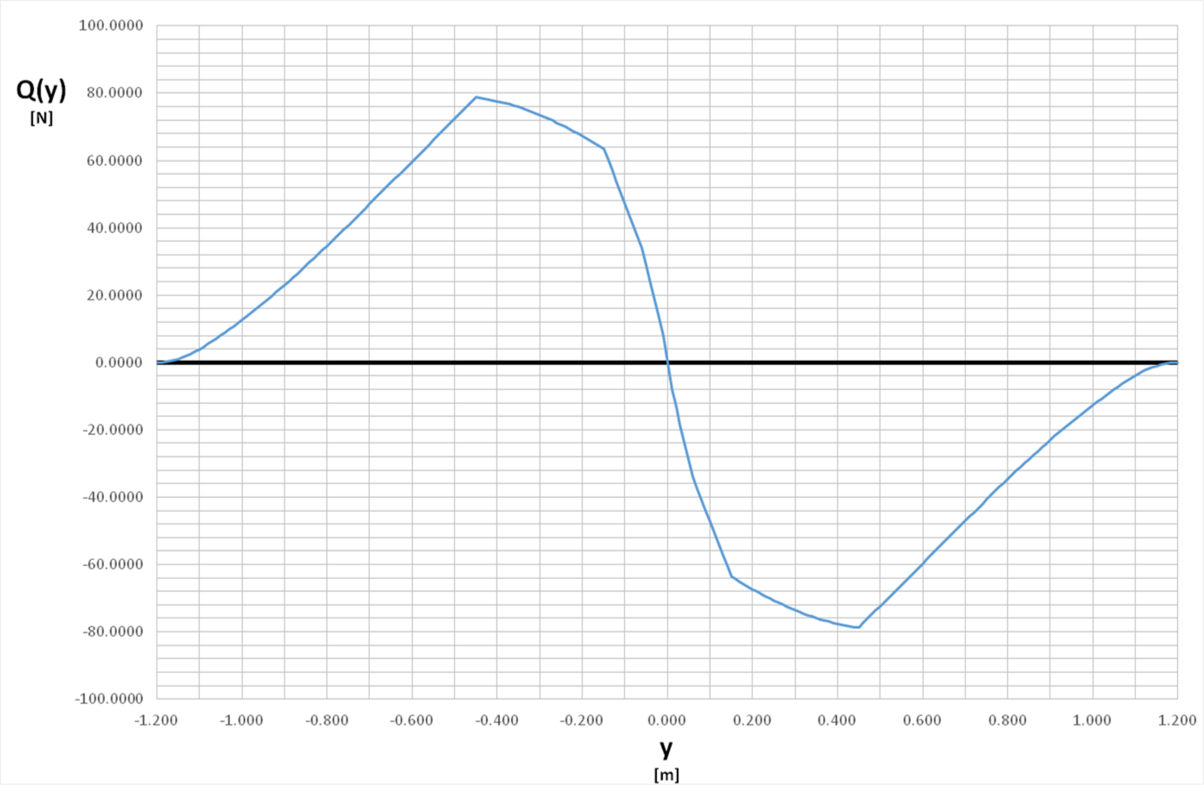

Figure 2.51: Shear Force Diagram

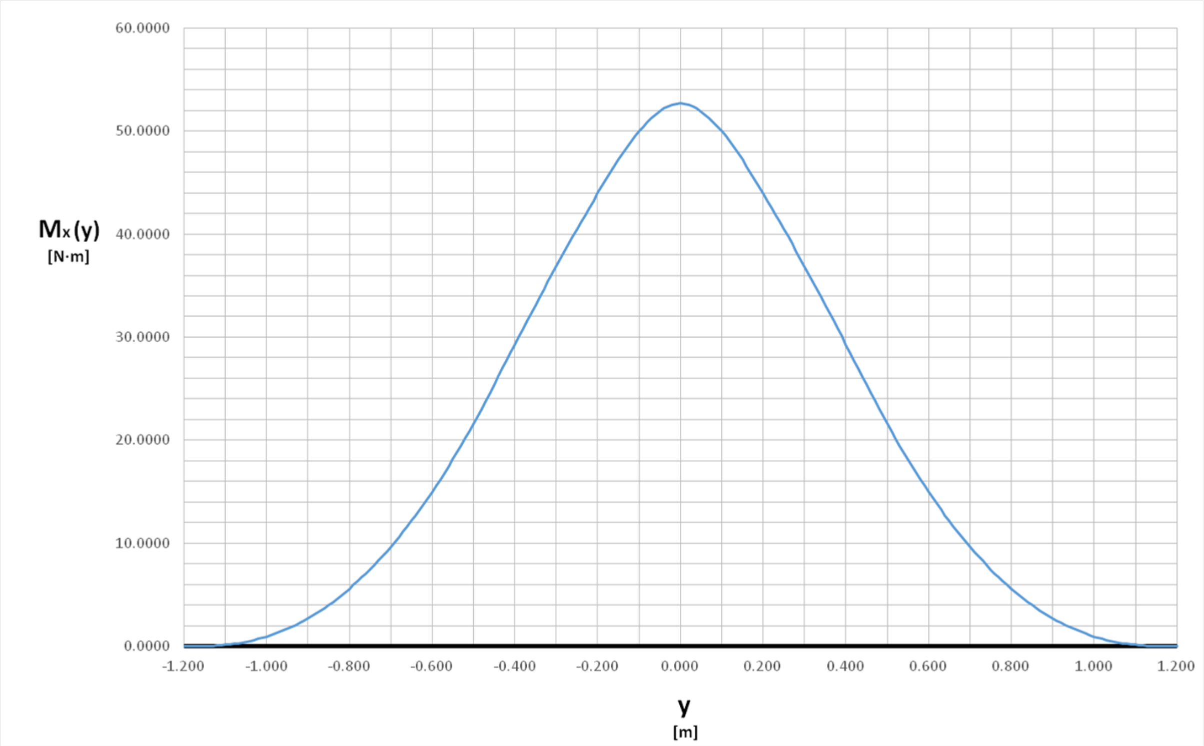

Figure 2.52: Bending Moment Diagram

of the aircraft. The maximum Bending moment at 7.04g is approximately:

$$M_{x\,max} = 52.69436\ N \cdot m$$

2.4.9 Airframe Structural Design

2.4.9.1 Cross section sizing

At this point the maximum shear force and bending moment values are obtained, and the cross section should be sized. The geometry of the cross section of the spars is chosen to be rectangular, in order to facilitate the integration of the control system components. The rear and front spars are the most critical elements, since they withstand the bending moment and the shear forces actuating on the whole airframe. Considering that the airframe can not surpass the fixed weight of 1.3 kg, CFRP T800S has been chosen as the material for the spars. From the previous section it is known that there are 3 important and critical points for the spars: the maximum bending moment point and the maximum shear force points.

For the first case, pure bending situation is considered, since the shear force is zero [6]. Therefore, on the center cross section of the spars the stress function is linear, where the maximum and minimum values of stress are respectively at the bottom and top points of the spar, as shown in the following figure.

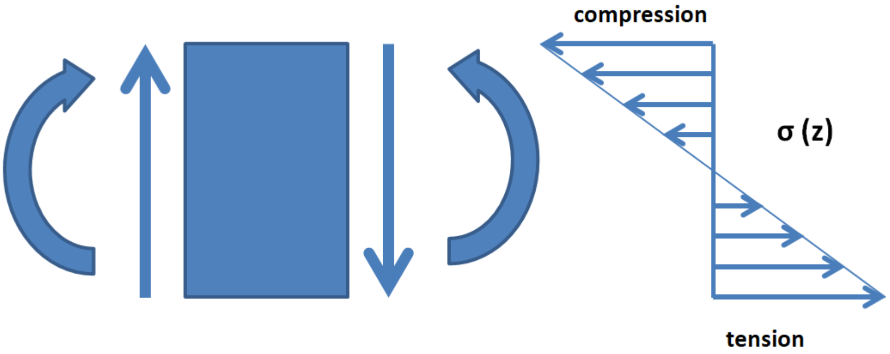

Figure 2.53: Pure bending. Stress linear distribution

The stress at a given point of the cross section can be calculated with the next equation [6]

$$\sigma(z) = -\frac{M_{x\,max}}{I_x} z \tag{2.52}$$

$$\sigma_{max} = \pm \frac{M_{x\,max}}{I_x} z_{max}$$

Since the cross section is rectangular, the moment of inertia is given by the next equation

$$I_x = \frac{1}{12} bh^3 \tag{2.53}$$

The symmetry plane of the aircraft crosses two spars. The height of the spars are determined by the airfoil at the center line:

- The height of the front spar at $y = 0\ m$ is $h_{0_{s1}} = 76mm$
- The height of the rear spar at $y = 0\ m$ is $h_{0_{s2}} = 24mm$

The geometry of both cross sections is described in the following figure.

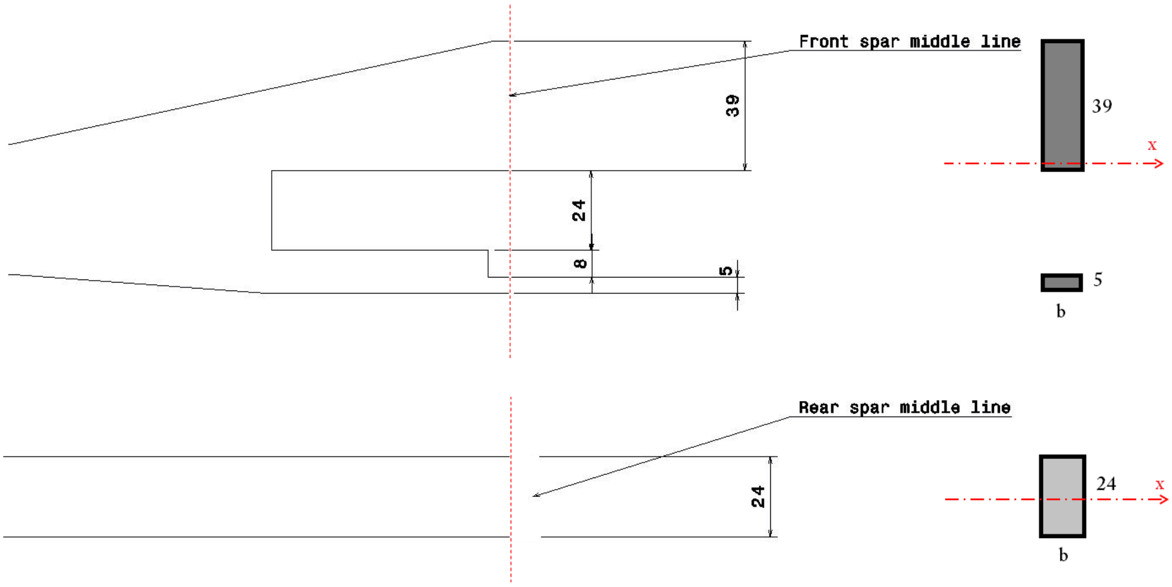

Figure 2.54: Front and rear spars geometry at the center line

At this point the moment of inertia of the spars cross sections must be calculated regarding the X–axis:

$$I_{x\,front} = \frac{1}{12} 76^3 \cdot b - I_{x\,missing} = \frac{109744}{3} \cdot b - I_{x\,missing}$$

The missing part moment of inertia can be calculated applying the Steiner theorem:

$$I_{x\,missing} = \frac{1}{12} 32^3 + 32 \cdot b \cdot (16+1)^2 = \frac{32936}{3} \cdot b$$

Therefore:

$$I_{x\,front} = \frac{73808}{3} \cdot b$$

$$I_{xrear} = \frac{1}{12}24^3 \cdot b = 1152 \cdot b$$

The total cross section resisting the bending moment has a moment of inertia of:

$$I_x = I_{xfront} + I_{xrear} = \frac{77264}{3} \cdot b$$

Since the front spar is higher, the maximum stress will be at its top and bottom point $z_{max} = \pm 38mm$. As the bending moment is positive, there is a compressing stress at the top point of the beam, and tensile stress at the bottom:

$$\sigma_{max} = \pm \frac{M_{xmax}}{I_x} z_{max} = \pm \frac{52.69436}{\dfrac{77264 \cdot 10^{-12} \cdot b}{3}} \cdot 0.038 = \pm \frac{77.7485}{b} \; MPa, \; b \; in \; mm \quad (2.54)$$

From the table 2, it is known that for CFRP T800S the Yield strength is 945 MPa. Applying a factor of safety of 2.0, the width b of the spars can be found:

$$\sigma_{max} \leq \frac{\sigma_{yield}}{SF} \leq \frac{945}{2}$$

$$\frac{77.7485}{b} \leq 472.5 \; MPa \longrightarrow b \; \geq \; 0.165 \; mm$$

This results show that the loads are quite small for a high performance material such as the CFRP T800S. The width of the spars is going to be considered 3mm, since the above mentioned material is available on sheets of 3mm and 5mm (Toray)[27]. This results in a tensile stress of $\sigma_{max} = 25.92MPa$. Although the cross sections seem to be over-sized, the CFRP lightweight enables to do so, and there are also two benefits:

- The control systems rails are going to be attached to the spars. Having over-sized spars results in negligible deflection at the central module of the aircraft, which provides a smooth motion to the control system.
- The commercially available smallest CFRP T800S sheet is of 3mm thickness, which is compatible with the required width of $b \geq 0.165 \; mm$ of the spars.

Regarding the points $y = -0.450m$ and $y = 0.450m$, where the Shear force has the maximum value, the general von Mises Equivalent Stress equation will be considered [8]

$$\sigma_{eq_{vM}} = \sqrt{\sigma^2 + 3\tau^2} \quad (2.55)$$

The tensile stress is calculated with the bending moment, as previously.

$$\sigma_{max} = \pm \frac{M_{x\,max}}{I_x} z_{max} \tag{2.56}$$

The shear stress is calculated by the Zhuravskii shear stress formula for beams [8]

$$\tau = \frac{Q_z \cdot m_x}{I_x \cdot e} \tag{2.57}$$

where Q_z is the total shear force at the cross section, the m_x is the first moment of area, the I_x is the second moment of area and e is the beam thickness.

- The front spar height at $y = \pm 0.450\ m$is $h_{1s1} = 26\ mm$
- The rear spar height at $y = \pm 0.450\ m$ is $h_{1s2} = 24\ mm$

The spars width is going to be considered the previously selected one of 3mm, and the goal is to proof if it can withstand the loads at $y = \pm 0.450\ m$.

$$I_x = \frac{1}{12} b {h_{1s1}}^3 + \frac{1}{12} b {h_{1s2}}^3 = \frac{1}{12} 26^3 \cdot 3 + \frac{1}{12} 24^3 \cdot 3 = 7850\ mm^4$$

The first moment of area of a rectangular cross section is:

$$m_{xtop} = m_{xbottom} = \frac{h}{2} \cdot b \cdot \frac{h}{4} = \frac{h^2 \cdot b}{8}$$

$$m_x = \frac{26^2 \cdot 3}{8} + \frac{24^2 \cdot 3}{8} = 469.5 mm^3$$

Using the shear force and bending moment diagrams and the previous equations, the tensile and shear stress are calculated:

$$\sigma_{max} = \pm \frac{M_{x\,max}}{I_x} z_{max} = \pm \frac{25.3821}{7.85 \cdot 10^{-9}} \cdot (\pm 0.013) = \pm 42\ MPa$$

As in the previous case, the top point of the beam is under compressing stress and the bottom point at tensile stress.

$$\tau = \frac{Q_z \cdot m_x}{I_x \cdot e} = \frac{78.8128 \cdot 4.695 \cdot 10^{-7}}{7.850 \cdot 10^{-9} \cdot 0.003} = 1.57 MPa$$

At this point the equivalent von Mises stress is calculated:

$$\sigma_{eq_{vM}} = \sqrt{\sigma^2 + 3\tau^2} = \sqrt{42^2 + 3 \cdot 1.57^2} = 42.1MPa$$

Comparing with the yield strength of the material and applying a factor of safety, there is still a huge margin:

$$\frac{\sigma_{yield}}{SF} = \frac{945}{2} = 472.5MPa \geq \sigma_{eq_{vM}} = 42.1MPa$$

The results show, again, that the front and rear spars are able to withstand the loads at load factor 7.04, with a factor of safety of 2.0.
Ribs are going to be placed every 10 % of the wingspan [7]. Additionally, S-glass stringers will be connecting the ribs perimeter, in order to avoid skin buckling [7], [8].

2.4.9.2 Motor mounting sizing

The mounting which holds the Brushless motor is one of the primary structural elements, since it supports a critical part and it is under a cycling load, which can change over time. The motor mounting is considered to be cylindrical, in order to fit with the blended wing-body structure. The outer diameter is the same as the motor fixed frame, which should be attached on the platform. At this point it is important to calculate the maximum shear force due to the motor Torque on the cross section of the mounting. The Torque is given by the next equation:

$$T = \frac{P}{\omega} \tag{2.58}$$

The shear force, which has the maximum value on the outer perimeter, is given by [8]

$$\tau_{max} = \frac{T \cdot r_o}{J_x} \tag{2.59}$$

The Torsion constant J_x which is the same as I_x in the case of a cylinder, is given by the next equation:

$$J_x = \frac{\pi}{2} \cdot ({r_o}^4 - {r_i}^4) \tag{2.60}$$

From the Hacker A40-12L motor specification list the angular frequency, the outer radius r_o and the power are obtained. The nominal power is 880 W, however the manufacturer marks the maximum power at 1100 W for 15 seconds use as maximum. The angular frequency is:

$$\omega = 6250RPM = 654.5\ rad/s$$

The material chosen for the mounting is the Aluminum 2024 alloy, since it has good fatigue resistance properties, relatively low density and it is less expensive.

The motor diameter is 41.7 mm, and the base diameter of the fixed frame is considered 60.0 mm. The Aluminum 2024 Shear Strength is

$$\tau_{yield} = 283\ MPa$$

A factor of safety of 2.0 has been applied and the maximum torque has been calculated:

$$T_{max} = \frac{1100}{654.5} = 1.68\ N \cdot m$$

From the previous equations it is possible to determine the inner radius r_i.

$$\tau_{max} = \frac{\tau_{yield}}{FS} = \frac{283 \cdot 10^6}{2.0} = \frac{T \cdot r_o}{J_x} = \frac{1.68 \cdot 0.03}{1.272\ 10^{-6} - 1.571 \cdot {r_i}^4}$$

$$r_i = 0.0299m = 29.9mm$$

The previous result means, that theoretically the inner radius of the mounting can be 29.9 mm, since the loads are relatively low. However, in order to attach the motor frame, the mounting should have more thickness. Therefore, the thickness is considered to be 2.5 mm. Also, the Aluminum 2024 sheets normally are available with 2.0 mm, 2.5 mm and 5.0 mm thickness. Therefore, the inner radius $r_i = 27.5mm$.

2.4.9.3 Airframe characteristics

At this section the list of all the structural elements are summarized, including the material and the weight:

Component name	**Material**	**Density** $[g/cm^3]$	**Volume** $[cm^3]$	**U. Weight** $[g]$	**Total Units**	**Total Weight** $[g]$
Front Spar	CFRP	1.55	156.910	243.21	1.00	243.21
Rear Spar	CFRP	1.55	87.465	135.57	1.00	135.57
Nose Spar	CFRP	1.55	39.610	61.40	1.00	61.40
Leading Edge Stringers	S-glass	2.53	1.785	4.52	4.00	18.06
Trailing Edge Stringers	S-glass	2.53	1.530	3.87	4.00	15.48
Lateral stability rail-front	ABS	0.90	68.510	61.66	1.00	61.66
Lateral stability rail-rear	ABS	0.90	68.510	61.66	1.00	61.66
Lateral Stability Box	ABS	0.90	35.955	32.36	1.00	32.36
Lateral Stability Wheels	ABS	0.90	2.617	2.36	6.00	14.13
Lateral Stability right wall and servo holder	ABS	0.90	33.320	29.99	1.00	29.99
Lateral Stability left wall and servo holder	ABS	0.90	33.320	29.99	1.00	29.99
Longitudinal stability rail-right	ABS	0.90	47.158	42.44	1.00	42.44
Longitudinal stability rail-left	ABS	0.90	47.158	42.44	1.00	42.44
Longitudinal Stability Box	ABS	0.90	14.144	12.73	1.00	12.73
Longitudinal Stability Wheels	ABS	0.90	1.335	1.20	4.00	4.80
Longitudinal Stability -Rack	ABS	0.90	31.875	28.69	1.00	28.69
Longitudinal Stability -Pinion	ABS	0.90	73.440	66.10	1.00	66.10
front wall	ABS	0.90	11.934	10.74	1.00	10.74
back wall	ABS	0.90	11.934	10.74	1.00	10.74
Rib N1 (y=0)	ABS	0.90	33.660	30.29	1.00	30.29
Rib N2 (y=71)	ABS	0.90	20.995	18.90	2.00	37.79
Rib N3 (y=150)	ABS	0.90	20.825	18.74	2.00	37.49
Rib N4 (y=450)	ABS	0.90	6.885	6.20	2.00	12.39
Rib N5 (y=1200)	ABS	0.90	3.400	3.06	2.00	6.12
Diagonal Ribs Upper (average)	ABS	0.90	2.210	1.99	20.00	39.78
Diagonal Ribs Lower (average)	ABS	0.90	1.615	1.45	20.00	29.07
Parachute mounting	ABS	0.90	12.240	11.02	1.00	11.02
Camera and gimbal mounting	ABS	0.90	33.091	29.78	1.00	29.78
Motor mounting	Aluminum	2.70	30.651	82.76	1.00	82.76
Skin compartment(removable)	ABS	0.90	65.008	58.51	1.00	58.51
Total weight						**1297.19**

Table 2.11: Structural elements characteristics

2.4.10 Numerical simulation by ANSYS

2.4.10.1 Simulation method and parameters

Aircraft's spars structure has been imported and meshed in the Ansys Workbench with the objective of finding the most critical points regarding stress and deformation. The discretized lift and weight distributions have been considered. The gravitational acceleration has been set to 7.04 times **g**. The fixed support for the airframe analysis has been considered the symmetry plane of the structure.

The same methodology has been applied to the motor mounting. The front wall of the mounting has been fixed (contact with the rear spar). The rear wall of the mounting (where the motor is attached) has been considered as the surface for the torque application. A torque of $3.36 N \cdot m$ has been applied including a factor of safety of 2.0.

2.4.10.2 Simulation results

Airframe simulation results have been illustrated in the Figure 2.55 and Figure 2.56, where the first one shows the equivalent von Mises stress distribution and the second one - the total deformation. The maximum stress value, unexpectedly, is on the rear spar middle section. When designing spars analytically, the front spar middle section has been supposed to be the location of maximum stress. However, it was a simplified unidirectional beam solution. The assigned lift and weight distribution, combining with the wing sweep create an additional component (torsional moment), which causes the rear spar to be under higher load. The maximum stress value (290 MPa) is still under the yield strength by a huge margin. Regarding the total deformation, it is possible to observe that the maximum value is at the wing tips, as expected. The maximum deflection is under 3 cm, which is reasonably acceptable. The most important thing regarding the spars deflection is probably the impact it could have on the lateral control system rails. However, the deformation from the root until $\pm 450 mm$ is null.

Motor mounting simulation results are as expected. The maximum stress values are on the outer perimeter, near the screws (see Figure 2.57). As explained in the analytic design, the cross section was over-sized for the given structural loads in order to have enough thickness for the screws. For this reason the maximum stress is about 4 orders of magnitude under the yield strength of Aluminum 2024. Consequently, the deformation is almost negligible (see Figure 2.58).

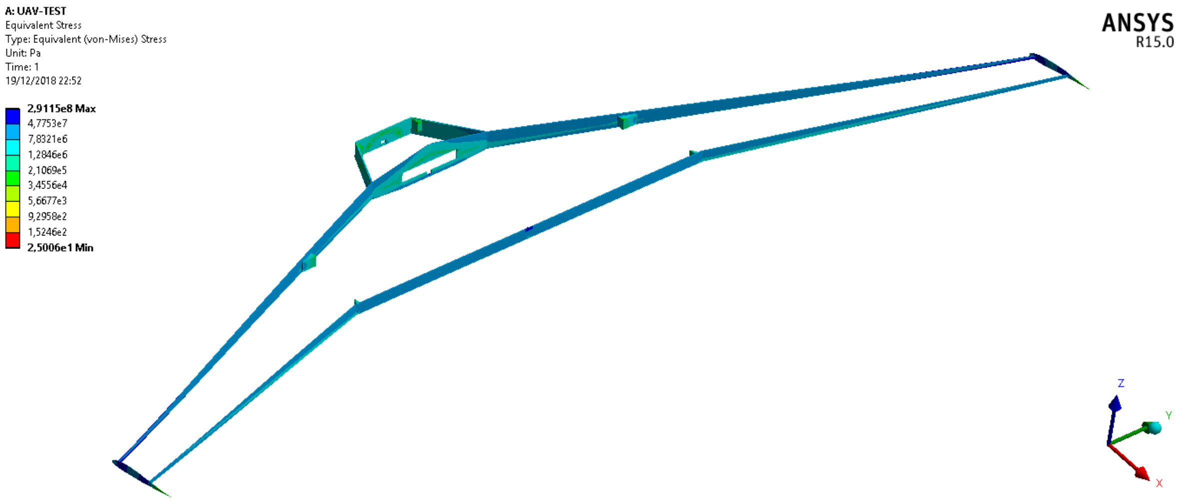

Figure 2.55: Equivalent von Mises Stress on spars

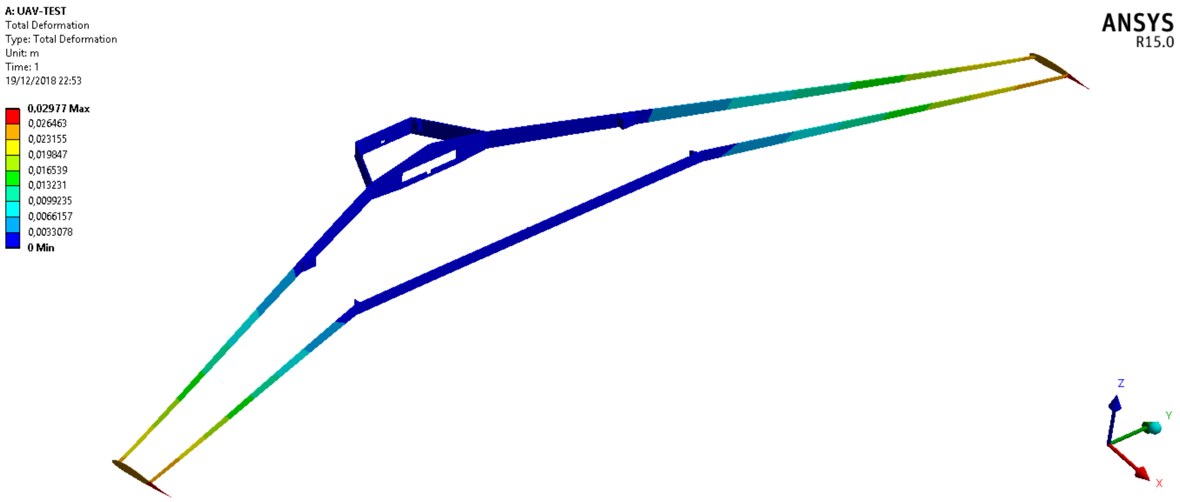

Figure 2.56: Total deformation of the spars

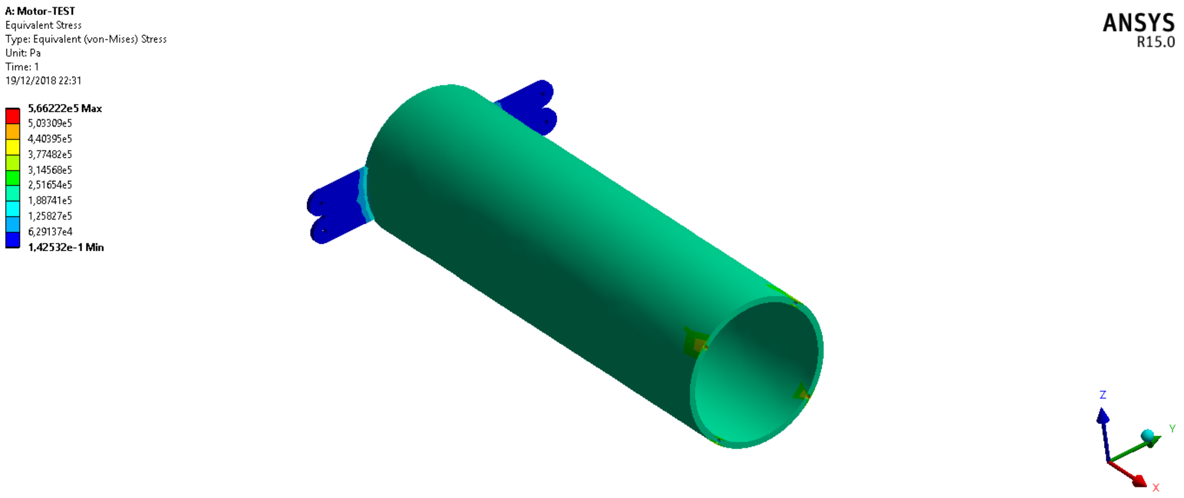

Figure 2.57: Equivalent von Mises Stress on the mounting

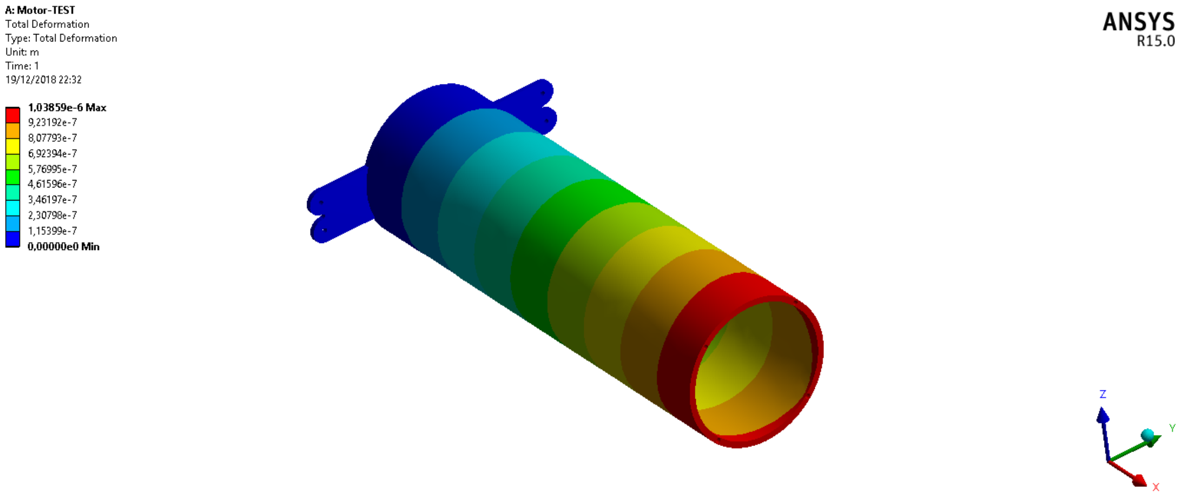

Figure 2.58: Total deformation of the motor mounting

2.4.11 Power Requirements

2.4.11.1 Required Power for Cruise Flight

Steady air temperature, pressure and density have been calculated for troposphere (under 11000m) and cruise flight conditions:

$$T(h) = T_o + \lambda \cdot h \tag{2.61}$$

$$p(h) = p_o \cdot \left(1 + \frac{\lambda \cdot h}{T_o}\right)^{-\dfrac{g_o}{R \cdot \lambda}} \tag{2.62}$$

$$\rho(h) = \rho_o \left(1 + \frac{\lambda \cdot h}{T_o}\right)^{-\dfrac{g_o}{R \cdot \lambda}-1} \tag{2.63}$$

Where $p_o = 1013.25\ hPa$; $T_o = 288.15\ K$; $R = 287\ J \cdot kg^{-1} \cdot K^{-1}$; $\lambda = -6.5 \cdot 10^{-3} K \cdot m^{-1}$; $\rho_o = 1.225\ kg \cdot m^{-3}$

For the flight altitude of 110 m the resulting steady air temperature, pressure and density are:

$$T = 287.435\ [K]$$

$$p = 1000.11\ [hPa]$$

$$\rho = 1.212\ [kg \cdot m^{-3}]$$

For the cruise flight the next equations have been considered:

$$T_{req} = D \tag{2.64}$$

$$L = W \tag{2.65}$$

$$P_{req} = T_{req} \cdot V = D \cdot V \tag{2.66}$$

$$C_D = C_{Do} + C_{Di} = C_{Do} + \frac{{C_L}^2}{\pi A e} \tag{2.67}$$

$$D = \frac{1}{2}\rho V^2 S C_{Do} + \frac{L^2}{\frac{1}{2}\rho V^2 \pi b^2 e} \tag{2.68}$$

$$P_{req} = \frac{1}{2}\rho V^3 S C_{Do} + \frac{L^2}{\frac{1}{2}\rho V \pi b^2 e}$$

The velocity for minimum power can be obtained by taking the derivative of the previous equation with respect to V and setting it equal to zero.

$$\frac{dP_{req}}{dV} = \frac{3}{2}\rho V^2 S C_{Do} - \frac{L^2}{\frac{1}{2}\rho V^2 \pi b^2 e} = 0 \tag{2.69}$$

$$V_{min,Power} = \left[\frac{4}{3}\left(\frac{W}{S}\right)^2 \frac{1}{\rho^2 C_{Do}} \frac{S}{\pi e b^2}\right]^{\frac{1}{4}}$$

According to Glauert and Weissingber studies regarding the induced drag and the Oswald span efficiency factor, as well as "Aircraft Design: A Conceptual Approach ", by Daniel P. Raymer, which are based on empirical methods using wind tunnels, the typical values of the Oswald factor are between 0.75 and 0.85. Since the scope of the project does not cover analysis in a wind tunnel, the lower statistical value has been chosen, which also leaves an improvement margin.

Introducing the geometrical and aerodynamic parameters, the velocity for minimum Power is calculated:

$$V_{min,Power} = \left[\frac{4}{3}\left(\frac{4 \cdot 9.8}{1.05}\right)^2 \frac{1}{1.212^2 \cdot 0.0081} \cdot \frac{1.05}{0.75 \cdot 2.4^2 \cdot \pi}\right]^{\frac{1}{4}} = 13.05\ [m/s]$$

At this point the Minimum Required Power can be calculated:

$$P_{req,min} = \frac{1}{2} \cdot 1.212 \cdot 13.05^3 \cdot 1.05 \cdot 0.0081 + \frac{(4 \cdot 9.81)^2}{\frac{1}{2} \cdot 1.212 \cdot 13.05\pi \cdot 2.4^2 \cdot 0.75} = 25.8\ [W]$$

The Required Power for the cruise flight at 16 m/s would be:

$$P_{req,cr} = 32.8\ [W]$$

2.4.11.2 Required Thrust and Power for Takeoff

The catapult launching angle α_c has been set to 11°, as shown on the next figure.

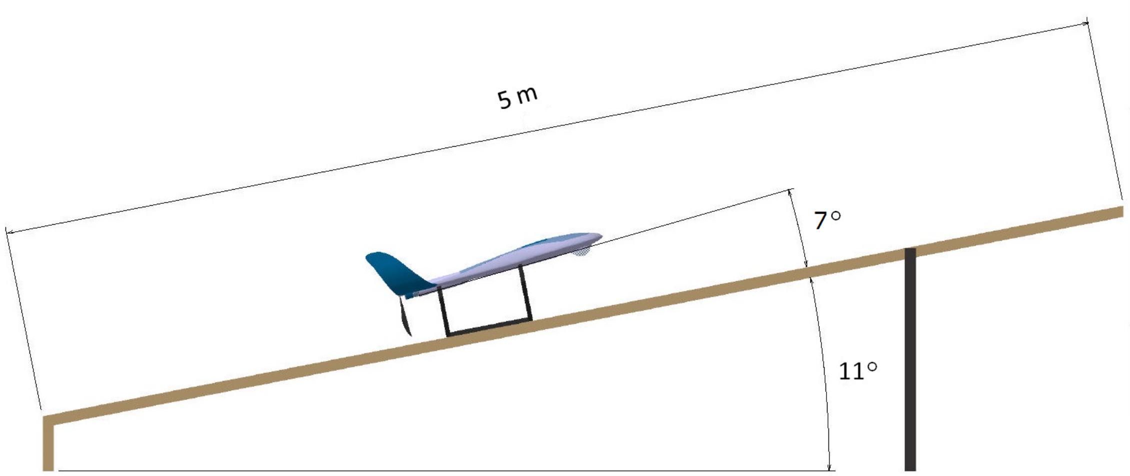

Figure 2.59: Launching platform setup

The components of the forces acting on the aircraft on the perpendicular axis to the platform are:

$$L = W \cdot cos\alpha_c = m \cdot g \cdot cos\alpha_c \tag{2.70}$$

$$\frac{1}{2}\rho S C_{LT-O} \cdot {V_{T-O}}^2 = m \cdot g \cdot cos\alpha_c$$

$$V_{T-O} = \sqrt{\frac{m \cdot g \cdot cos\alpha_c}{\frac{1}{2}\rho S C_{LT-O}}} \tag{2.71}$$

The mounting which glides on the catapult rail and holds the aircraft should be adjusted to the takeoff angle α_{T-O} equal to 7°. At an angle of attack equal to α_{T-O} the lift coefficient is 0.6181, and the drag coefficient is 0.0357. Therefore, the takeoff speed can be calculated:

$$V_{T-O} = 9.84\ [m/s]$$

Since the catapult rail has a length of 5 m, it is important to calculate the required takeoff thrust and acceleration. The next equations have been used for this purpose, considering the X-Axis parallel to the catapult rail:

$$x(t) = x_o + v_o t + \frac{1}{2}at^2 \tag{2.72}$$

$$v(t) = v_o + at \tag{2.73}$$

$$T_{req,T-O} - D - W \cdot \sin\alpha_c = F_{T-O} - D - m \cdot g \cdot \sin\alpha_c = ma \tag{2.74}$$

Considering that:

$$x_o = 0\ m, \quad x(t = t_{T-O}) = 5\ m, \quad v_o = 0\ m/s, \quad v(t = t_{T-O}) = V_{T-O} = 9.84\ m/s,$$

$$\frac{1}{2}a \cdot {t_{T-O}}^2 = 5\ [m]$$

$$V_{T-O} = a \cdot t_{T-O} = 9.84\ [m/s]$$

Therefore, the launching time should be:

$$t_{T-O} = 1.02\ [s]$$

and the required acceleration is:

$$a = 9.65\ [m/s^{-2}]$$

The launching force that the catapult should transfer to the aircraft or the required thrust for takeoff can be calculated by the next equation:

$$F_{T-O} - D - W \cdot \sin\alpha_c = F_{T-O} - \frac{1}{2}\rho S C_{DT-O} \cdot {V_{T-O}}^2 - m \cdot g \cdot \sin\alpha_c = m \cdot a$$

$$F_{T-O} = 48.2\ [N]$$

At this point, when the required Power for cruise flight and the required launching force are calculated, there are two options to consider regarding the brushless motor.

- The first one is relying on the launching catapult functionality and choosing a motor according to the cruise flight conditions. This solution leads to a much less powerful motor, with force-major risk limitations, which means that in case that the launching catapult pneumatic system is not working, the vehicle can not be launched. Although this option would allow the selection of a motor under 100 W, which also means a much lighter drive system, it also would lack the safety margin for higher speed maneuvers, which could cause overheating, since the required power would be very close to the design limits.

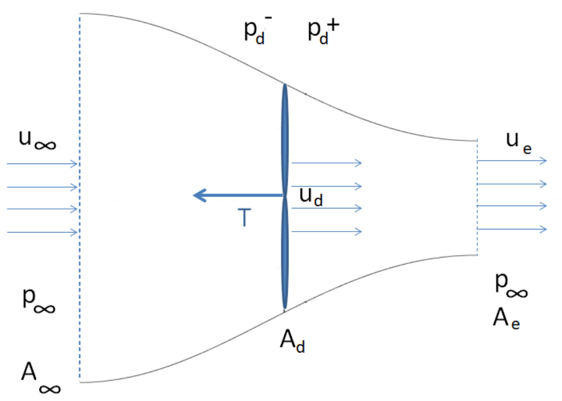

Figure 2.60: Disk actuator theory diagram

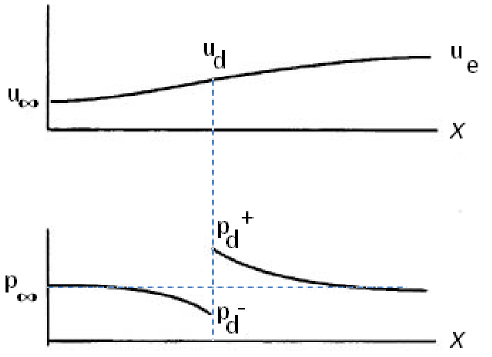

Figure 2.61: Speed and pressure according to Momentum theory

- The second option, though less optimal from the weight perspective, provides operational benefits and flexibility. The solution consists in a more powerful motor according to takeoff requirements, considering that only the catapult rail is available, and the pneumatic system is damaged, out of battery or can not be transported to the launching place.

The second option has been chosen, since according to the State of the Art there have been found brushless motors under 300 g for both options. Therefore, the required power for the takeoff has been determined as:

$$P_{req,T-O} = F_{T-O} \cdot v_{T-O} = 474.54 \approx 475\ [W] \tag{2.75}$$

2.4.12 Propeller design and efficiency

2.4.12.1 Momentum Theory

Since the required power and thrust have been determined, it is important to find or design a suitable propeller and then, to choose a motor according to the propeller efficiency.

Considering the Principle of mass conservation and constant density:

$$G_\infty - G_e = \rho u_\infty A_\infty - \rho u_e A_e = 0 \tag{2.76}$$

which leads to:

$$u_\infty \cdot A_\infty = u_e \cdot A_e = u_d \cdot A_d$$

Since $G_\infty = G_e = G_d$, from here on it will be denoted as G.

Considering the Principle of Momentum conservation:

$$G_e \cdot u_e - G_\infty \cdot u_\infty = T \tag{2.77}$$

or simply:

$$G \cdot (u_e - u_\infty) = T$$

Adding the Principle of Energy conservation:

$$\frac{1}{2} G({u_e}^2 - {u_\infty}^2) = P \tag{2.78}$$

and since the energy that the propeller transfers to the fluid is:

$$P = T \cdot u_d \tag{2.79}$$

The next results is obtained:

$$u_d = \frac{u_e + u_\infty}{2} \tag{2.80}$$

Then the following equation has been obtained:

$$T = 2G(u_d - u_\infty) = 2\rho A_d u_d (u_d - u_\infty) \tag{2.81}$$

At this point it is possible to compare the power generated by the propeller, which is transferred to the fluid, and the net power for the propulsion.

$$P_{net} = T \cdot u_\infty \qquad P_{prop} = T \cdot u_d$$

The propulsive efficiency, therefore, is:

$$\eta_p = \frac{T \cdot u_\infty}{T \cdot u_d} = \frac{u_\infty}{u_d} \tag{2.82}$$

The speed on the disk plane can be written as:

$$u_d = \frac{u_\infty + \sqrt{{u_\infty}^2 + \dfrac{2T}{\rho A_d}}}{2} \tag{2.83}$$

And:

$$\eta_p = \frac{u_\infty}{u_d} = \frac{2u_\infty}{u_\infty + \sqrt{{u_\infty}^2 + \dfrac{2T}{\rho A_d}}} = \frac{2}{1 + \sqrt{1 + \dfrac{2T}{\rho A_d {u_\infty}^2}}} \tag{2.84}$$

At this point, since the required Thrust is calculated, and the propeller maximum diameter is fixed by the geometric limitation of the launching platform, it is possible to obtain the required propulsive efficiency of the propeller. It is important to note that the propeller

thrust depends on different parameters, such as the profile, the geometry, the lift and drag distribution, the angular velocity, etc. However, knowing the required propulsive efficiency, the disk diameter, and the steady flight speed it is possible to find a propeller since some manufacturers provide propeller charts.
From the launching platform setup, the maximum separation between the trailing edge and the rail is 210 mm, and keeping some margin,the propeller radius is assigned to be:

$$R_{p_{max}} = 200mm$$

- For the cruise flight conditions the propulsive Froude efficiency is:

$$\eta_p = 0.97$$

- For takeoff, the propulsive efficiency is:

$$\eta_{p_{T-O}} = 0.54$$

Finally, the required power for the takeoff that the motor should supply to the propeller, is:

$$P_m = \frac{P_{prop_{T-O}}}{\eta_{p_{T-O}}} \approx 880\ [W]$$

It is important to note that the motor should be working at this power for the launching time, which is 1.02 seconds.

2.4.12.2 Blade Element Method

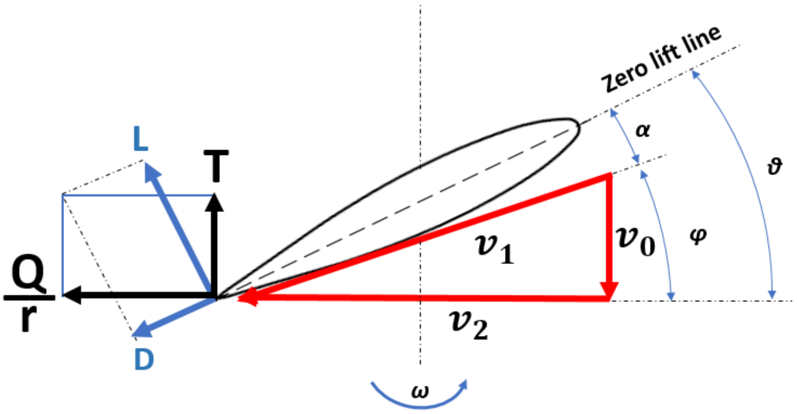

Figure 2.62: Force and speed components on a blade element

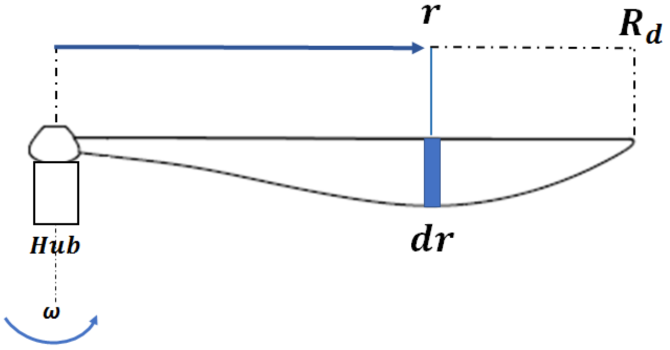

Figure 2.63: Blade element scheme

Considering $\theta(r)$ as the twist distribution along the propeller radius and velocity components as illustrated in Figure 2.62, where v_0 is the **axial flow at propeller disk** and v_2 is the **angular flow**, the angle of attack of each blade element can be written as:

$$\alpha(r) = \theta(r) - \phi(r) = \theta(r) - \arctan\left(\frac{v_0}{v_2}\right) \tag{2.85}$$

It is important to note that:

- 2D study is considered, so the induced velocity components are neglected along the blade radius
- for each blade, the angle of attack is measured regarding the airfoil zero lift line

Therefore, for a given **twist distribution** $\theta(r)$, the local angle of attack for each blade can be calculated, and from the airfoil polar graphs the corresponding c_l and c_d values can be found. Then, for each blade element, the total lift and drag forces can be determined, which should be projected on the axial and tangential axis, to determine thrust and torque components:

$$\Delta T = \Delta L \cos\phi - \Delta D \sin\phi \tag{2.86}$$

$$\frac{\Delta Q}{r} = \Delta L \sin\phi + \Delta D \cos\phi \tag{2.87}$$

where:

$$\Delta L = c_l \cdot \frac{1}{2} \cdot \rho \cdot {v_1}^2 \cdot c \cdot dr \tag{2.88}$$

and

$$\Delta D = c_d \cdot \frac{1}{2} \cdot \rho \cdot {v_1}^2 \cdot c \cdot dr \tag{2.89}$$

where

$$v_1 = \sqrt{{v_0}^2 + {v_2}^2} \tag{2.90}$$

Considering that the propeller has two blades:

$$\Delta T = \frac{1}{2}\rho {v_1}^2 c(c_l \cos\phi - c_d \sin\phi) dr \cdot 2 \tag{2.91}$$

$$\Delta Q = \frac{1}{2}\rho {v_1}^2 c(c_d \cos\phi + c_l \sin\phi) r \cdot dr \cdot 2 \tag{2.92}$$

Therefore, the design steps would be defined as:

- definition of the twist distribution $\theta(r)$
- discretization of the blade into N elements along the radius
- calculation of the angle of attack of each blade element $\alpha(r)$
- determination of c_l and c_d for each blade element
- determination of the local drag and lift, and then, local thrust and torque

2.4.12.3 BEM without inflow factors

At this section, the axial flow at propeller disk v_0 and the angular flow v_2 are calculated neglecting the inflow factors. Therefore, the axial flow can be considered approximately equal to the aircraft advance speed and the angular flow can be calculated considering only the blade rotation.

$$v_0 = u_\infty$$

$$v_2 = \omega \cdot r$$

$$v_1 = \sqrt{{v_o}^2 + {v_2}^2} = \sqrt{{u_\infty}^2 + \omega \cdot r^2}$$

According to [9] and Alfred Gessow studies (1948), the ideal twist can be calculated as:

$$\theta(r) = \frac{\theta_{tip}}{r} \tag{2.93}$$

Actually, the state of the art of the aircraft propellers suggests that the ideal theoretical twist is almost identical to the optimal twist, based on the wind tunnel analysis [9]. Furthermore, the Eppler E63 airfoil has been selected for the blade design, which is one of the most used airfoils for medium size propellers. The next calculations will be done for takeoff, since it is when the propulsive efficiency seems to be the lowest according to the previous chapter. For the next calculations, 6000 RPM will be considered. The blade tip angular flow is calculated with the next equation, for takeoff and cruise flight:

$$v_{1tip_{t-o}} = \sqrt{{u_\infty}^2 + \omega \cdot {R_d}^2} = \sqrt{9.84^2 + \left(6000 \cdot \frac{2\pi}{60} \cdot 0.2\right)^2} = 126.05\ [m/s]$$

$$\phi_{tip_{t-o}} = \arcsin \frac{u_\infty}{v_1} \rightarrow \phi_{tip} = 4.48°$$

and

$$v_{1tip_{cr}} = \sqrt{{u_\infty}^2 + \omega \cdot {R_d}^2} = \sqrt{16^2 + \left(6000 \cdot \frac{2\pi}{60} \cdot 0.2\right)^2} = 126.7\ [m/s]$$

$$\phi_{tip_{cr}} = \arcsin \frac{u_\infty}{v_1} \rightarrow \phi_{tip} = 7.25°$$

At cruise flight condition, the higher ϕ for the same twist distribution will decrease the angle of attack. Therefore, for the calculation of the θ_{tip}, $\phi_{tip_{cr}}$ will be considered as the reference value.

Considering the Eppler E63 airfoil c_l/c_d vs α graph for Reynolds numbers between 50,000 and 100,000, since the maximum Reynolds over the blade is around 77000, the optimal α value is obtained, which is around $\alpha_{opt} = 5°$. Therefore, the blade twist at the tip is:

$$\theta_{tip} = \alpha_{opt} + \phi_{tip} = 12.25°$$

Then, the blade has been divided into 100 elements. The twist distribution $\theta(r)$ for $0.14m < r < 0.2m$ has been calculated according to the ideal twist equation, while for

$0 < r < 0.14m$ linear twist distribution has been considered, which provides almost constant angle of attack distribution close to α_{opt}. For each blade element, C_l, C_d, ΔT and ΔQ have been calculated (see Report Attachment [1]).

- For **takeoff**, the total thrust and torque can be calculated, considering **two-blade propeller**:

  $$T = 2 \cdot \Delta T = 48.5\ N$$

  $$Q = 2 \cdot \Delta Q = 1.2\ N\ m$$

  At this point, the thrust and torque coefficients can be calculated:

  $$\begin{aligned} C_T &= \frac{T}{\rho n^2 {D_d}^4} = 0.1546 \\ C_Q &= \frac{Q}{\rho n^2 {D_d}^5} = 0.0096 \end{aligned} \tag{2.94}$$

  Then, the propeller efficiency can be calculated:

  $$\eta_{prop} = \frac{J\ C_T}{2\pi\ C_Q} \tag{2.95}$$

  where the advance ratio is defined as:

  $$J = \frac{u_\infty}{nD_d} = \frac{V_{T-O}}{nD_d} = 0.2460 \tag{2.96}$$

  $$\eta_{prop_{T-O}} = \frac{J\ C_T}{2\pi\ C_Q} = 0.63$$

  $$C_p = \frac{C_T \cdot J}{\eta_{prop}} = 0.0604$$

- The previous steps have been repeated for **cruise flight** conditions and the efficiency has been calculated:

  $$\eta_{prop_{cruise}} = \frac{J\ C_T}{2\pi\ C_Q} = 0.85$$

2.4.12.4 BEM with inflow factors

Blade Element Method (BEM) complexity begins when inflow factors are considered for the calculation of the local angle of attack.
The equation 2.4.12.1 can also be written as:

$$u_e = 2v_0 - u_\infty \tag{2.97}$$

For a streamtube, the axial flow and angular flow velocities can be considered of the form:

$$v_0 = u_\infty + a \cdot u_\infty \tag{2.98}$$

$$v_2 = \omega r - b \cdot \omega r \tag{2.99}$$

where **a** is the **axial inflow factor** and **b** is the **angular inflow factor**.
Therefore, u_e can be rewritten as:

$$u_e = 2v_0 - u_\infty = u_\infty + 2a \cdot u_\infty = u_\infty(1 + 2a) \tag{2.100}$$

Therefore, the thrust and angular momentum equations for each blade element can be written as:

$$\Delta T = 2\pi r\ dr\ \rho\ u_\infty(1 + a)(u_\infty(1 + 2a) - u_\infty) = 4\pi r \rho {u_\infty}^2(1 + a)a\ dr \tag{2.101}$$

and

$$\Delta Q = 2\pi r \rho u_\infty(1 + a)(2b\omega r)r\ \ dr = 4\pi r^3 \rho\ u_\infty(1 + a)b\omega\ dr \tag{2.102}$$

Summarizing all the previous steps and considering two-blade propeller, the next system of equations is obtained:

$$\begin{cases} \Delta T = \rho {v_1}^2 c(c_l \cos\phi - c_d \sin\phi)dr \\ \Delta Q = \rho {v_1}^2 c(c_d \cos\phi + c_l \sin\phi)r \cdot dr \\ v_1 = \sqrt{{v_0}^2 + {v_2}^2} \\ \alpha = \theta - \arctan\left(\dfrac{v_0}{v_2}\right) \\ \Delta T = 4\pi r \rho {u_\infty}^2(1 + a)a\ dr \\ \Delta Q = 4\pi r^3 \rho u_\infty(1 + a)b\omega\ dr \end{cases} \tag{2.103}$$

The system can be solved with an iterative method, supposing initial values for the inflow factors a and b. Then, through the equations 2.98 and 2.99 velocity components v_0 and v_2 can be calculated. This will allow the calculation of v_1, and α. Then, ΔT and ΔQ can be calculated. To end the iterative process, equations 2.101 and 2.102 can be used to recalculate inflow factors **a** and **b**. The process should be repeated until the desired tolerance is achieved.

After the final inflow parameters are obtained, ΔT and ΔQ can be calculated. Then, the total thrust and torque can be calculated from the following equations:

$$
\begin{aligned}
T &= \sum_{n=1}^{N} \Delta T \\
Q &= \sum_{n=1}^{N} \Delta Q
\end{aligned}
\tag{2.104}
$$

The same twist distribution will be used as in the simplified blade element method calculation, since it provides reasonably acceptable angle of attack distribution for cruise flight and for takeoff. The calculation is done by a script written in Python (see Report Attachment [1], following the next algorithm:

- introduction of twist (exponential function) and chord distribution (linear function)
- introduction of the number of blade elements
- introduction of initial inflow parameters **a** and **b**
- introduction of the advance speed, RPM and the desired tolerance

Step 1. Calculate v_0 and v_2 for each element

Step 2. Calculate v_1, ϕ and α for each element

Step 3. Calculate ΔT and ΔQ for each element

Step 4. Calculate **a** and **b** for each element using ΔT and ΔQ values

Step 5. Iterate the process until for each element the desired tolerance is met for **a** and **b**.

The script can be found attached in the "Extras" folder. At first, it has been used for cruise flight condition, and it and has shown total convergence. The results are illustrated in the following figures.

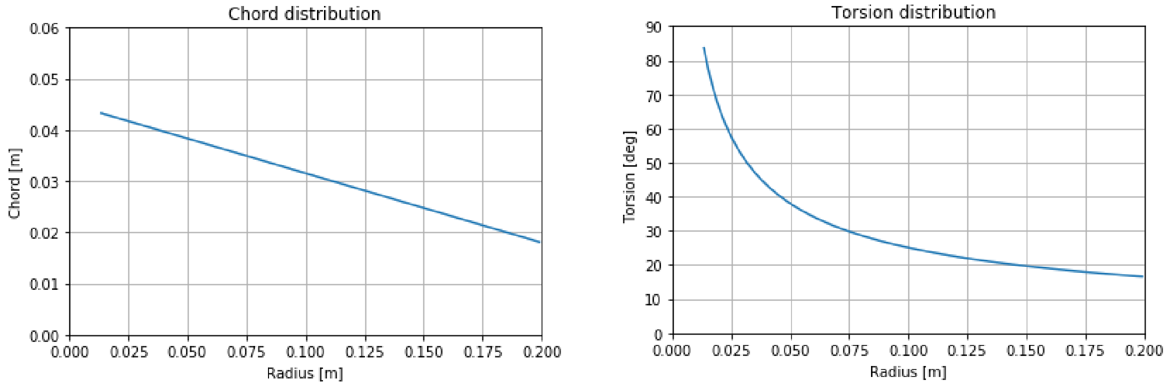

Figure 2.64: Propeller geometry: chord and twist distributions

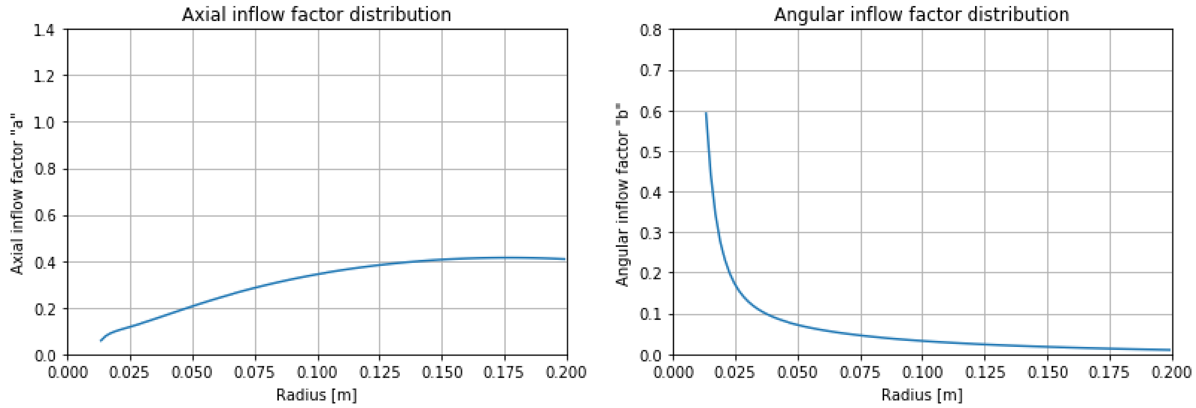

Figure 2.65: Inflow factors distribution for cruise flight

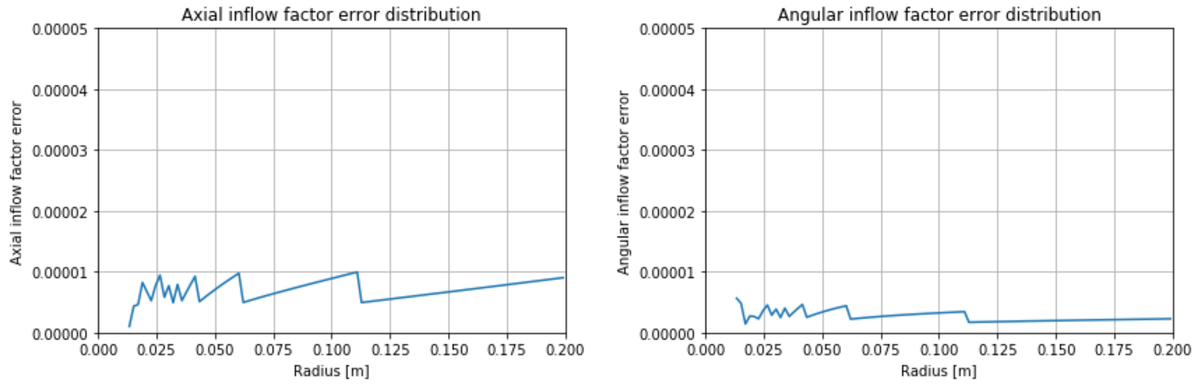

Figure 2.66: Inflow factors error distribution for cruise flight

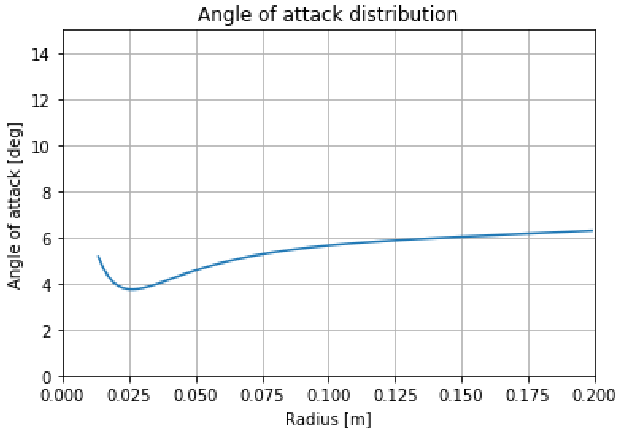

Figure 2.67: Angle of attack distribution for cruise flight

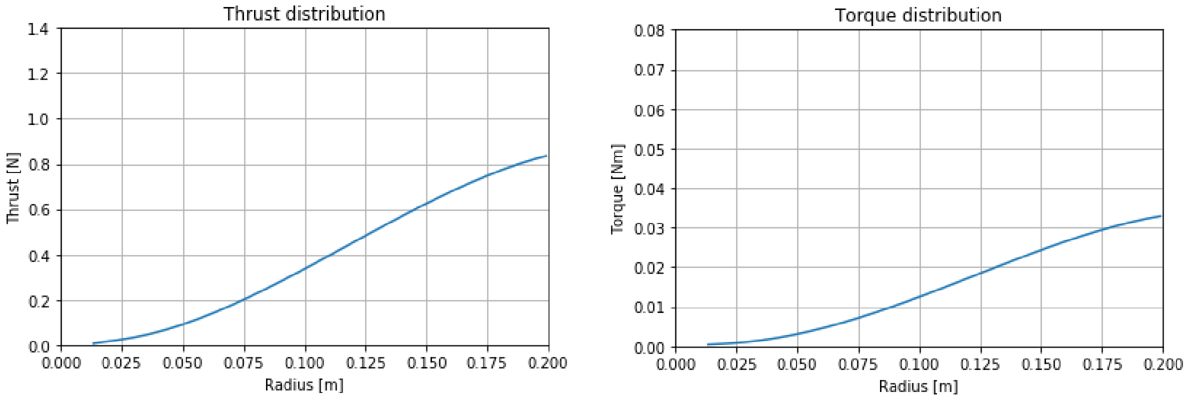

Figure 2.68: Thrust and torque distribution for cruise flight

The results for cruise flight are:

- **Advance ratio:** $J = 0.4$
- **Thrust coefficient:** $C_t = 0.12530$
- **Torque coefficient:** $C_q = 0.01202$
- **Efficiency:** $\eta_p = 0.6634$
- **Power coefficient:** $C_p = 0.0756$

The same methodology has been applied for takeoff, with the following results:

- **Advance ratio:** $J = 0.246$
- **Thrust coefficient:** $C_t = 0.15586$
- **Torque coefficient:** $C_q = 0.01284$
- **Efficiency:** $\eta_p = 0.4751$
- **Power coefficient:** $C_p = 0.0807$

The final conclusion is that the selected twist distribution provides almost constant angle of attack distribution, which fulfills the design requirement. Also it provides the required thrust for takeoff.

2.4.12.5 Propeller selection

Considering the previous calculations and propeller geometry, the **APC Thin Electric 16x10 E** propeller has been chosen. Based on the technical sheet provided by the manufacturer it satisfies the efficiency requirement [30]. The maximum diameter is 16 inches, and the pitch is 10 inches.

Figure 2.69: APC Electric 16x10 E propeller [30]

The data sheet provided by the manufacturer is summarized in the Report Attachment [1] and in the Technical Sheets Attachment [2].

2.4.12.6 Momentum Theory vs BEM vs Experimental data

The propeller design process involved different methods, and at this point, when the experimental data has been obtained, it seems reasonable to compare these results.

- At first place, Momentum Theory has been applied to calculate the efficiency for different thrust and advance speed values. The obtained values were: $\eta_{p_{T-O}} = 0.54$ and $\eta_{p_{cruise}} = 0.97$.
- At second place, Blade Element Method has been introduced, beginning with a simplified calculation, where inflow factors were neglected, thus, ignoring the induced velocity components from one blade element to the next(no induced axial and angular velocities). However, this method helped to determine an initial geometry (chord and twist distribution) for constant angle of attack distribution throughout the blade radius. The obtained efficiency values were: $\eta_{p_{T-O}} = 0.63$ and $\eta_{p_{cruise}} = 0.85$.
- At third place, Blade Element Method with Inflow Factors has been applied. This sophisticated method provides more realistic results through numerical simulation. $\eta_{p_{T-O}} = 0.4751$ and $\eta_{p_{cruise}} = 0.6634$.
- Finally, according to experimental results of a similar propeller (APC 16x10E), provided by the manufacturer, efficiency values are: $\eta_{p_{T-O}} \approx 0.44$ and $\eta_{p_{cruise}} =$

0.68.

The comparison confirms that, generally, Momentum Theory application is not enough, since the efficiency estimation is far from realistic. However, due to its simplicity, it provides a first guess. On the other hand,the Simplified Blade Element Method provides only a slight improvement over Momentum Theory. Finally, experimental confirm a reasonably acceptable approximation given by the Blade Element Method with Inflow Factors.

Considering a required power for takeoff of 475 W, and the experimental propulsive efficiency, the required power that the motor should supply to the propeller has been calculated:

$$P_{mT-O} = \frac{P_{prop_{T-O}}}{\eta_{p_{T-O}}} \approx 1080\ [W]$$

and for cruise flight:

$$P_{mcruise} = \frac{P_{prop_{cruise}}}{\eta_{p_{cruise}}} \approx 48\ [W]$$

2.4.13 Propulsion System

Considering power requirements and weight limitations, the brushless motor **A40-12L V4 14-Pole** has been selected, with a maximum power of 1100 W. Regarding the Electronic Speed Controller, **X-70 OPTO-Pro** has been selected, as it is the recommended one by the manufacturer. Specifications can be found in Technical Sheets Attachment[2] and in the Report Attachment[1].

Figure 2.70: Hacker A40-12L V4 motor [32]

Figure 2.71: ESC X-70 OPTO-Pro [32]

2.4.14 Energy Storage System

The energy storage system for small and medium size electric aircraft normally consists of Lithium-Ion or Lithium-Polymer batteries. The main reason Lithium is preferred over Alkaline and Nickel-Cadmium is due to its high energy density, providing relatively small size batteries, which is a great advantage.

Normally, the energy storage system is considered a big portion of the total weight, which, combined with the goal of having a mass-actuated control system, makes it the best candidate to be linked to the actuator. Also, having decided to control the center of gravity position on x-axis and y-axis independently, it seams reasonable to divide the energy supply of Avionics and Drive into two parts. The reason is that for electronic components a relatively low capacity battery should be enough, while a drive system normally requires a bigger battery. Then, electronic system components and their corresponding battery could be attached to the longitudinal control system, while the drive system batteries could be attached to the lateral control system. Another advantage is that having drive batteries isolated would provide a better estimation of the flight time, besides the benefits of simplified electronic system design and maintenance. The energy distribution scheme is illustrated in the Figure 2.72.

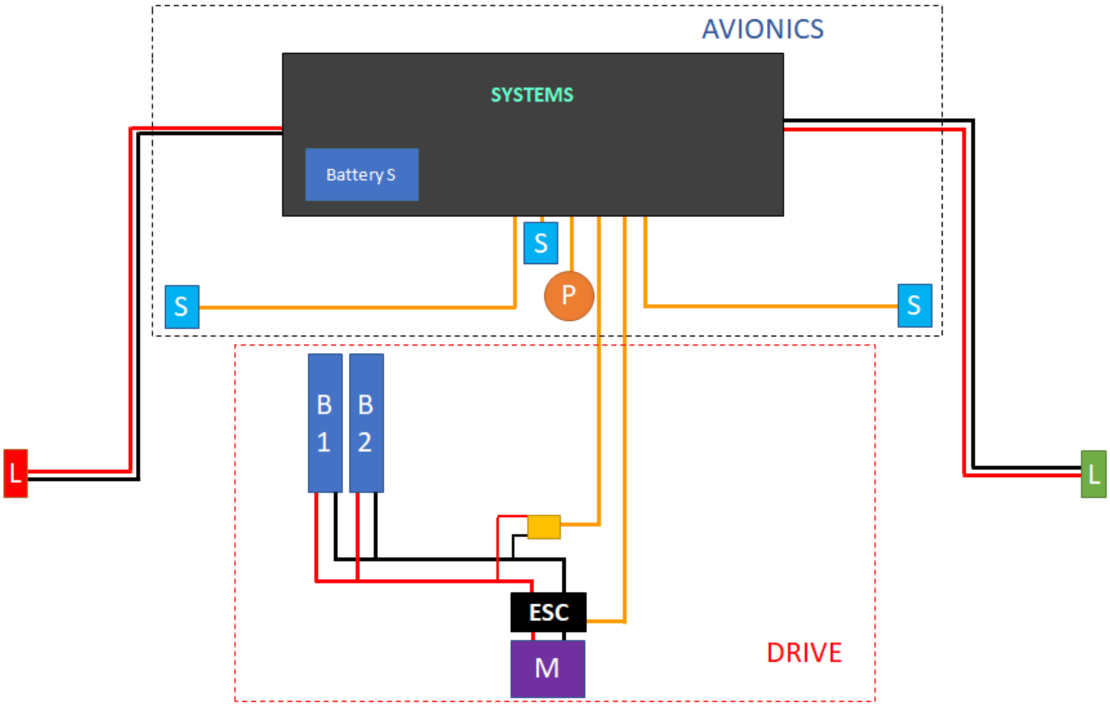

Figure 2.72: Energy distribution diagram

2.4.14.1 Energy Storage Capacity

Since the beginning of the Project a goal has been set regarding the endurance, which should be around 60 minutes. This would give an advantage against competing quadrotor drones, which normally have an endurance between 15 and 30 minutes at the current state of art (DJI Phantom, Mavic, etc.). The required battery capacity has been calculated according to this goal.

At cruise flight, where the required power and propulsive efficiency have already been calculated, the selected brushless motor operates at the next conditions:

- RPM: 1200 rev/min
- Voltage: 3.7 V
- The required power provided to the propeller, considering a cruise flight, is 35.3 W.
- The required current would be 9.5 Amperes.
- Considering voltage loses, motor wire resistance Ri, and idle current (zero torque current), the current has been approximated to 10 Amperes, which corresponds to the discharge rate.

The battery capacity for drive systems has been calculated for a 60 minutes cruise flight.

$$K_{B,drive} = I_{discharge} \cdot 1hour = 10000mAh$$

Normally it is highly recommended by Lithium-Polymer battery manufacturers to not discharge more than 85 % of the capacity. Considering also the energy consumed at takeoff at maximum Power, two batteries of 7500 mAh each have been selected for the propulsion system. Considering the motor manufacturer recommendation, the LiPo 5S type battery has been chosen.

The battery for the electronic system has been selected by the same methodology. Considering a discharge rate of 3 Amperes (defined by the power distribution board), a flight time of 1 hour, and a maximum battery capacity usage close to 85 %, the required capacity has been calculated:

$$K_{B,systems} = \frac{3000mA \cdot 1h}{0.85} \approx 3529mAh \tag{2.105}$$

The closest standard battery capacity is 3500 mAh. Considering the input voltage required for the power distribution board (between 5 and 12 V) a 2 cell LiPo battery is sufficient (7.2 V). The TopFuel LiPo 10C-ECO-X Light 3500mAh 2S battery has finally been selected.

Figure 2.73: Drive system battery [32]

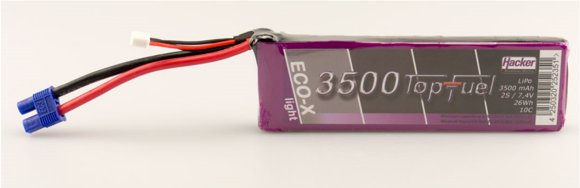

Figure 2.74: Electronic system battery [32]

Additionally, a current sensor has been added between the electronic systems battery and the power distribution board. The selected model is the FullSpeed FSD AMASS XT60 current sensor, which weights 5.2 grams, and its dimensions are 18.5 x 15.8 x 12mm. The sensor is compatible with LiPo 2-6S batteries, and accepts a maximum input current of 80 Amperes.

Specifications of the batteries can be found in the Technical Sheets Attachment[2] and in the Report Attachment[1].

Figure 2.75: Current Sensor [42]

Figure 2.76: ABSIMA GPS-1 charger [34]

2.4.14.2 Charging System

Since there are three LiPo batteries and they have different number of cells, a special multi-channel charging system has been selected, which is compatible with all the batteries and allows simultaneous charging. The selected charging system is the ABSIMA GPS-1, manufactured by Hacker-Motor GmbH [32]. One of the most important features that this system offers is the Individual cell balancing function, which guarantees safety and longevity to the Lithium batteries.

Secifications and other functionalities can be found in the Technical Sheets Attachment[2] and in the Report Attachment[1].

2.4.15 Electronic Systems

2.4.15.1 Requirements

According to the Legislative framework analysis and project requirements, a list of electronic systems has been defined for controllable and safe flight.

- The plane should have launching and landing systems.
- There should be an electronic system, linking power and signal connections between all the components.
- There should be a communication system, consisting of a Receiver and a Transmitter, providing communication between the ground unit and the unmanned aerial vehicle.
- There should be a navigation system, providing the required information regarding the flight altitude, vehicle location, speed, acceleration and other parameters.
- There should be a control system, providing control and stability to the aircraft for a defined trajectory.

2.4.15.2 Electronic System Diagram

All on-board electronic components form a complex system which is illustrated in the Figure 2.87. It is important to note that the diagram intention is to illustrate power and signal connections between components. Thus, the size and scale of those components of the diagram has no relationship with the real components. On the diagram below, there are three type of wires, where:

- Red wires represent power supply connection
- Black wires represent power ground connection
- Orange wires represent signal connection

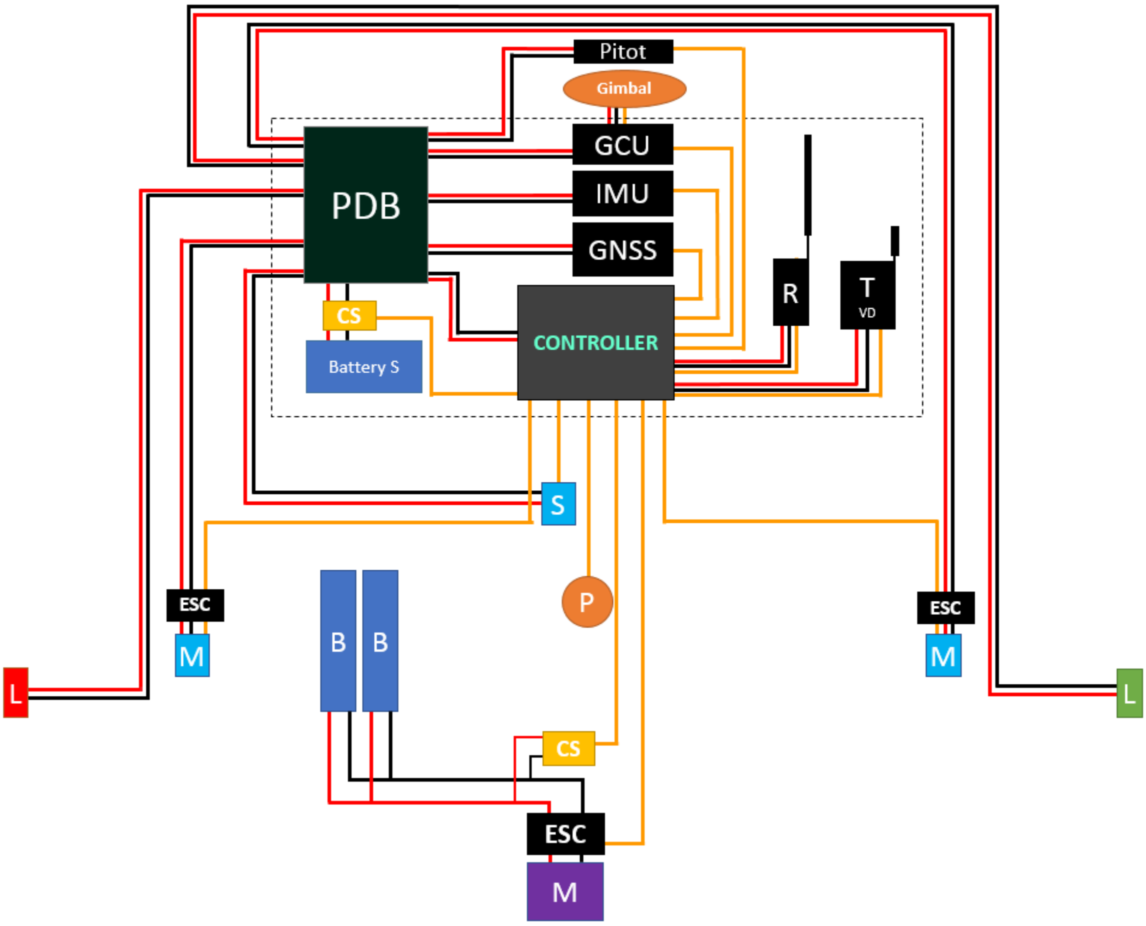

Figure 2.77: On-board electronics diagram

Components enclosed in the discontinuous line box are linked to the longitudinal control system. This group is powered by a separate LiPo battery. The battery is directly connected to the Power Distribution Board (PDB). The current sensor (yellow box) sends the battery status to the Controller. The power distribution board has at least 10 ports, where all the system components but the drive are connected. It should have one port for input power.

The Controller is the central box of the diagram, consisting of an internal memory and a central processing unit (CPU). It has, at least 13 channels or ports, for input/output signals. It is the brain of the unmanned aerial vehicle, and as such, it constantly calculates the required output values for a set of input parameters. The controller receives signals from the Pitot-Static tube, the Inertial Measurement Unit (IMU), the Global Positioning System (GPS), the Receiver and current sensors. Controller output channels are connected to the servos of the longitudinal and lateral control systems, the parachute releasing system, the electronic speed controller, the gimbal controller and the

Transmitter. The CPU internal programs and algorithms are discussed in the Flight Control chapter.
The Global Navigation Satellite System comes with integrated GPS and GLONASS, which provides a safer flight, since the number of available satellites to connect is increased.
The Inertial Measurement Unit consists of a three axis Gyroscope and three axis Accelerometer. Changes of angular velocity and acceleration are continuously sent to the Controller.
The Gimbal Control Unit is a simple one servo controller that provides the required tilt to the camera or thermal sensor.
The Receiver and Video-Data Transmitter form a communication system between the ground unit and the unmanned aerial vehicle. The Receiver delivers user-requests to the Controller, while the Transmitter provides First-Person-View of the camera and also sends information regarding location, battery voltage level, etc.
Additionally, there are 3 servos for the stabilization and control of the vehicle. There are also two navigation lights according to the normative.
The Pitot-Static tube is located on the vehicle nose and it provides the dynamic pressure, which is then used to determine the vehicle velocity.
The orange circle represents the landing system, which consists of a parachute.
The drive system, as explained previously, consists of two mobile batteries, a current sensor, an electronic speed controller and a brushless motor.

2.4.15.3 Lights and Warning Systems

Although, the Unmanned Aerial System (UAS) Draft does not clearly claim any requirement regarding external lights, it has been decided to follow the guideline of the CS-VLA and include navigation lights. Considering the weight limitations, the following lights have been selected:

- Left light - Red color (DS-30A-1 Red Magnum Strobe)
- Right light - Green color (DS-30A-1 Green Magnum Strobe)

The lights specifications, provided by the manufacturer [42], are available in the Technical Sheets Attachment[2]

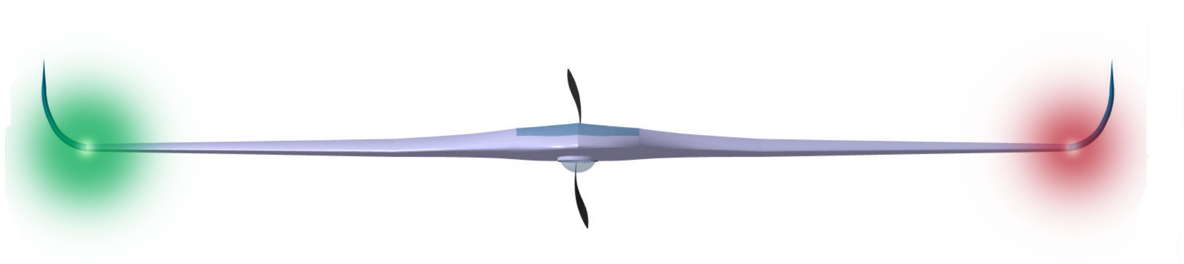

Figure 2.78: Navigation lights from the front view [42]

2.4.15.4 Communication Systems: On-board

The Communication System components are divided into two groups, depending on their location. On-board components main features include order receiving, order transferring (to the controller), and order transmitting (to the ground unit). On the other hand, the Ground Unit components have the functionality of transmitting signals according to the pilot orders and receiving data from the vehicle, which can be encrypted video or status information.

The on-board receiver should have at least 8 channels, since it receives the next signals:

- 1 channel for the Throttle
- 3 channels for the gimbal control (pitch, yaw and roll)
- 2 channels for the aircraft radio control on free flight mode (pitch and roll)
- 1 channel for the parachute launching order
- 1 channel for the coordinate data input (up to 5 points)

Flysky FS-iA10B PPM and IBUS protocol receiver has been selected, offering 10 channels. The extra 2 channels can be used for pre-programmed functions. Regarding the transmitter, it should be able to send analog or encrypted video to the ground unit for First Person View. Additionally, it should send information regarding the aircraft status, such as battery level, aircraft speed, altitude and position on Earth frame. The selected video and data transmitter is the model EST1 Transmitter by Advanced Microwave Products. On-board components specifications are available in the Technical Sheets Attachment[2]

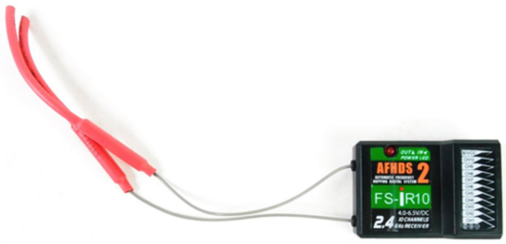

Figure 2.79: FlySky FS-iA10B Receiver [35]

Figure 2.80: AMP EST1 Transmitter [36]

2.4.15.5 Communication System: Ground Unit

The ground unit consists of a portable computer with a special software for the flight remote control. The software should provide information regarding the aircraft status as well as FPV window. The interface should also allow path definition, similar to a map-window where the aircraft position is shown in real-time. When in free flight mode, the user can use an external joystick to control remotely the aircraft throttle, camera tilt angle as well as the pitch and roll motions. The next figure illustrates the Graphical User Interface (GUI) of the software.

Safe Mode

Ready to launch

45°44′12.7″N 14°00′36.2″E

ELEVATION: 531m
DISTANCE: 21.0km
DURATION: 21:54
AREA: 67.4ha

Figure 2.81: Command control software GUI

The ground unit video-data receiver should be compatible with the on-board transmitter. Thus, the ESR1 Receiver has been selected, manufactured by Advanced Microwave Products. Regarding the ground unit Transmitter, it should have compatible channels and frequency with the on-board Receiver. It should allow the pilot to send orders for throttle, gimbal control, aircraft control, landing order and path coordinates. The selected model is the FS-i10 transmitter. Both components are connected to the ground unit computer, and data inputs-outputs are controlled by the software. The remote control can also be used in free flight mode (manual radio control). Specifications of the ground unit components are available in the Technical Sheets Attachment[2].

Figure 2.82: AMP ESR1 Receiver [36]

Figure 2.83: FlySky FS-i10 Transmitter [35]

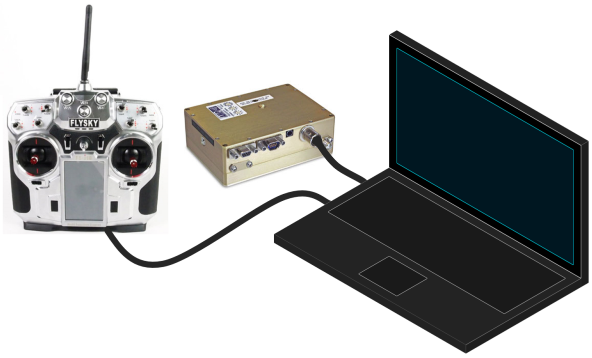

Figure 2.84: Ground Unit Setup

2.4.15.6 Navigation Systems and Sensors

2.4.15.6.1 Pitot-Static Tube

Since the fixed wing aircraft generated lift depends on the true airspeed, it is reasonable to have a dedicated airspeed sensor. Even though some controllers track the GPS coordinates and by the combination of the on-board accelerometer estimate the velocity, pitot-static airspeed sensors offer more precision and require less computation. For the current project the MPXV7002 airspeed kit has been selected, which is mounted on the aircraft nose. Specifications are available in the Technical Sheets Attachment[2].

2.4.15.6.2 Global Navigation Satellite System

The Matek Systems SAM-M8Q GNSS model has been selected, since it is one of the most complete satellite systems available considering its size and weight. It includes GPS, GLObal NAvigation Satellite System (GLONASS), Galileo, Quasi-Zenith Satellite System (QZSS), and also correcting systems such as the Satellite Based Augmentation System (SBAS). Specifications are available in the Technical Sheets Attachment[2].

Figure 2.85: Pitot-Static Airspeed Kit [42]

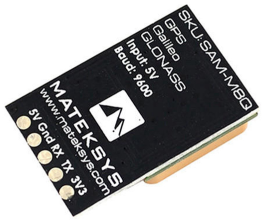

Figure 2.86: GNSS: Matek SAM-M8Qd [34]

2.4.15.6.3 Power Distribution Board

The selected Power Distribution Board is the Lantian PDB, which has 10 output and one input ports.

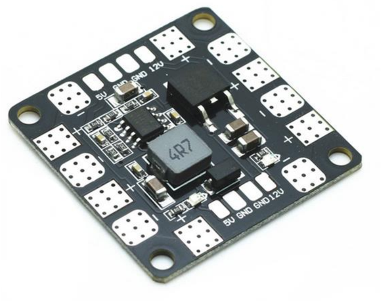

Figure 2.87: Power Distribution Board [42]

2.4.15.7 Control System

The main tasks of the Control System are:

- Speed control: regulated by the electronic speed controller (ESC), which changes the supplied voltage to the brushless motor, and therefore, changes the rotational speed. The ESC specifications are described in the Propulsion Appendix.
- Landing: controlled by the action of the parachute releasing system. The actuator is directly connected to the Controller, which orders the releasing action. The order

source can be the user (pilot) or the Controller itself if a dangerous condition is found (inevitable stall, on-board damage, no signal for an established period of time).

- Camera tilting: controlled by the gimball controller, which moves the 3 brushless servomotors. The gimbal controller is directly connected to the Flight Controller, and it tilts the camera according to the pilot indications.
- Longitudinal stability: includes the control of nose-up, nose-down movements and combined maneuvers. All the components and their functions are going to be discussed in this chapter, while the Controller Algorithm is going to be explained in the Performance Appendix.
- Lateral stability: includes turn at constant speed and combined maneuvers. In this chapter the required components are going to be listed. Again, the correspondent Controller Algorithm explanation can be found in the Performance Appendix.

2.4.15.7.1 Gimbal and Gimbal Controller

The 3-axis gimbal is made by the combination of the camera mounting and 3 brushless motors, which provide Pitch, Yaw and Roll control of the camera. The relatively small Tiger GB4106 Brushless Gimbal Motors have been chosen. The gimbal controller provides pitch, yaw and roll control. Three output ports send a direct signal to each of the servos of the gimbal, controlling the corresponding motion. The gimbal controller has a separate inertial measurement unit which should be mounted on the gimbal for higher precision. The 8-Bit Mini 3-Axis AlexMos Gimbal Controller has been selected, which specifications can be found in the Technical Sheets Attachment [2].

Figure 2.88: Tiger GB4106 Brushless Gimbal Motor [42]

Figure 2.89: 8-Bit Mini 3 Axis AlexMos Gimbal Controller [42]

2.4.15.8 Landing system: parachute characteristics

The landing system consists of a rapidly deployed parachute. The MARS 58 V2 parachute has been selected. According to the manufacturer (Mars Parachutes [28]), the design is compact (5.7 cm of diameter) and light weight (88.0 g). The parachute is compatible for fixed-wing vehicles as well as multi-rotor drones under 4.5 kg of total mass. The parachute is compressed in a vented canister and uses a high energy compression spring for the deployment, actuated by an analog servo (Hitec HS-82MG Metal Gear Servo). The parachute mounting is fixed on the front spar middle section, as illustrated in the Figure 2.91. The removable skin compartment is attached and pushed altogether with the parachute, when released (Figure 2.92). It is important to note that the total parachute system weight given by the manufacturer is around 260 g, which also includes the attachment joint. Since the prototype already has a parachute mounting fixed on the front spar, the parachute system has been simplified.

Figure 2.90: Parachute canister [28]

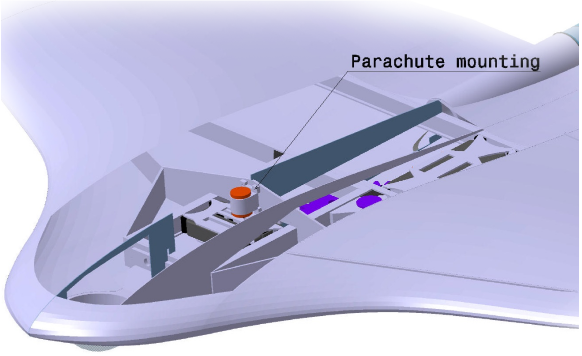

Figure 2.91: Parachute mounting (orange)

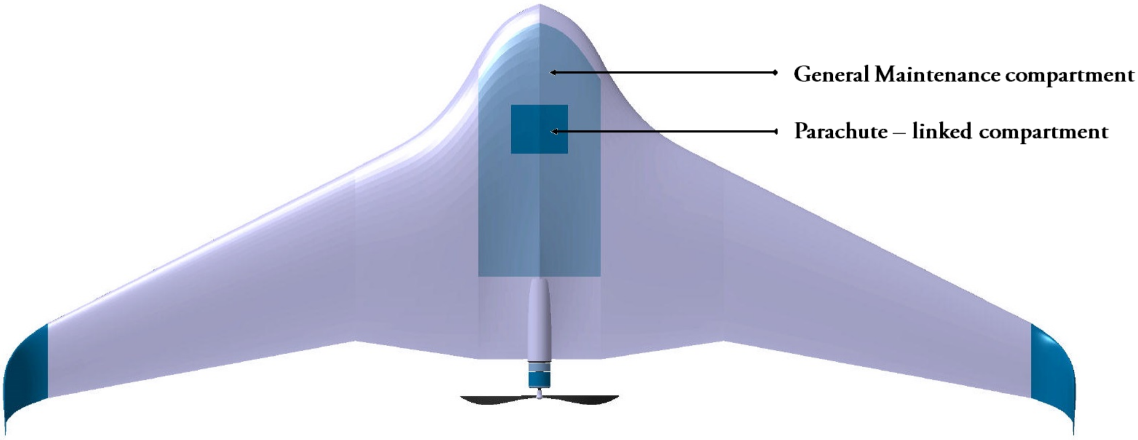

Figure 2.92: Skin removable compartments

2.4.15.9 Launching system: pneumatic catapult characteristics

The vehicle launching is provided by a pneumatic or counterweight catapult. There is a variety of launching systems compatible with the current prototype dimensions. From those, the Pneumatic Catapult PL-40 has been chosen as an example. Its specifications have been provided by the manufacturer [31]. The typical launch angle is 11°. The overall rail length when assembled is 5.0 *m*. Total weight of the catapult is around 56 *kg*, and the typical set-up time is 5 min. The maximum allowed plane mass is 45 *kg*, and the maximum allowed launch velocity 25 *m*/*s*.

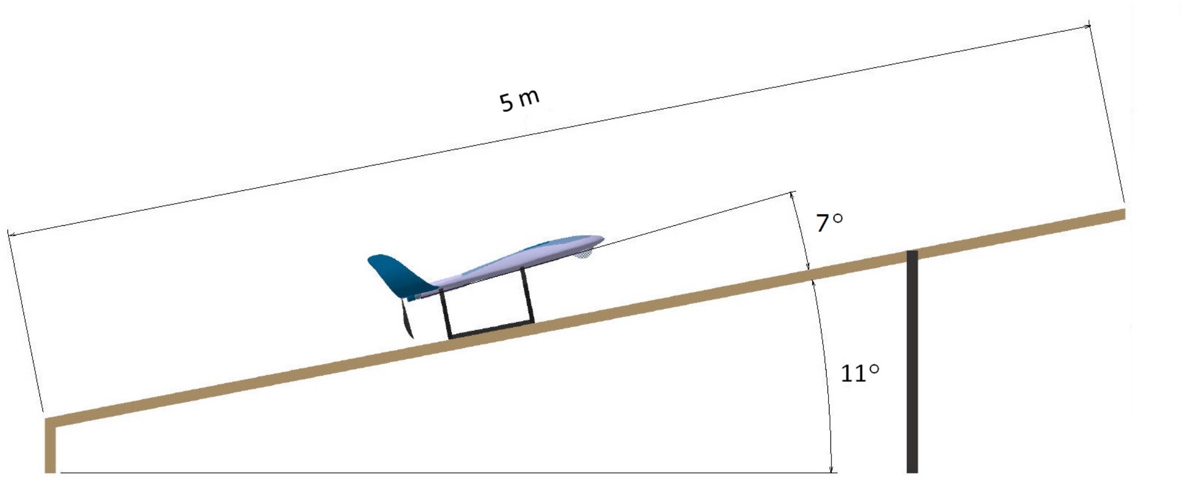

Figure 2.93: Launching configuration: side view

Figure 2.94: Assembled Pneumatic Catapult PL-40 [31]

2.4.15.10 Optional cameras and sensors

Since one of the main features of the designed unmanned aerial system is mapping, a list of some optional cameras and thermal sensors under 250 grams is included. Specifications provided by manufacturers could be found in the Report Attachment [1].
High Definition cameras

- **Sony FCB-H11**: a light camera with small form factor and great image quality.
- **Sony FCB-EX1020**: a color block camera with excellent picture quality and scan mode.
- **Panasonic GP-MH310**: a single chip full HD module camera, with superior color performance.
- **Hitachi DI-SC120R**: a compact chassis-type camera delivering unparalleled low light performance

Thermal sensors:

- **FLIR Tau 2**: a long-wave thermal imaging camera.
- **FLIR Tau SWIR**: a short-wave infrared camera.
- **NanoCore 640M 5000978-3**: a small size, light weight, and low power thermal sensor.
- **DRS Tamarisk 640**: a small size, low weight, and minimal power consumption thermal sensors.

2.4.16 Mass-Actuated Control System Design

Throughout this chapter, the mass-actuated control system design will be discussed. The control system design has been proposed according to the previously done aerodynamic and structural design, and taking into consideration the real size of the electronic components that can be integrated in the mass-actuated control system.

2.4.16.1 Longitudinal Stability Control System

The longitudinal stability control system, as introduced in the Systems Appendix, consists of a mobile box which contains systems components. The system is moved over the aircraft x_b axis, actuated by a rack and pinion mechanism. At the System Appendix, the servo motor specifications were listed.

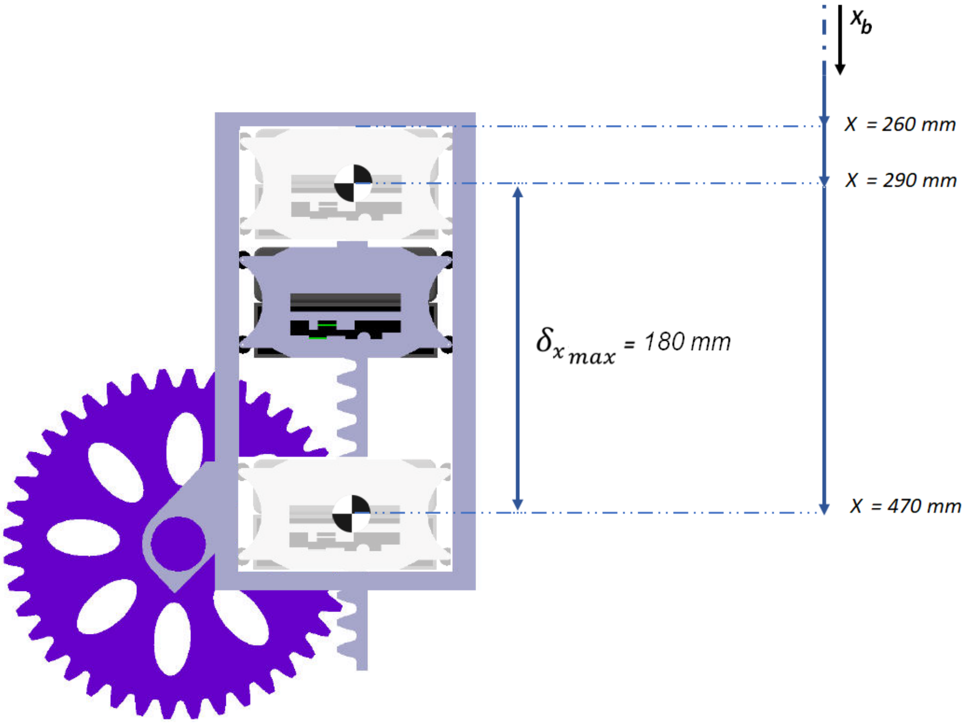

Figure 2.95: Longitudinal Control System

The mobile box movement is allowed in the range $290mm < x < 470mm$, calculated from the nose, which gives a maximum displacement of $\delta_{xmax} = 180mm$, as illustrated in the figure 2.95.

As a design criteria, few considerations have been established:

- The acceleration phase is neglected, due to relatively small displacement, speed and mass values.

- It is considered that the full motion is done in 2 seconds, which results in $\dot{\delta}_x = 90\ [mm/s]$.

Therefore, considering the reference on the aircraft nose, the displacement over the x_b axis can be written as:

$$\delta_x(t) = \dot{\delta}_x \cdot t + \delta_{x_0} = 0.09 \cdot t + 0.29$$

where δ_{x_0} is the position at which the control system movement starts, calculated from the nose.

Additionally, since the rack and pinion geometrical parameters have been set during the design process, with the requirement of being integrated in the structure, the pinion rotational speed can be calculated as:

$$\omega_p = \frac{\dot{\delta}_x}{R_p} \approx 9.5\ [RPM]$$

$$\frac{n_r^*}{n_t} = \frac{17-2}{40} = 3:8$$

The low gear ratio provides a smooth motion, since the servo is required to rotate at relatively low RPM.

The Longitudinal Stability Control System, as illustrated on the next diagram, consists of:

- **Rails** which allow a maximum displacement of 430 mm.
- **Box (with wheels)** that contains the Avionics and that moves along the rails.
- **Rack and Pinion** that move the box.
- **Continuous Servo** which allows a rotation up to 360 °. Since the pinion is mounted on the servo axis, its rotational movement is transferred to the pinion.

All the components but the servo are made of an ABS plastic. The blueprints of these components can be found in the Drawing Appendix.

The DITEX TD0606M continuous servo has been selected, which specifications [32] can be found in the Technical Sheets Attachment [2].

Figure 2.96: DITEX TD0606M Servo [32]

2.4.16.2 Pitching moment model

The center of gravity variation along the x_b axis, denoted as ΔX_{CG}, generates a pitching moment variation, due to the center of pressure distance variation. Since the center of pressure changes with the angle of attack, it has been decided to develop the analysis based on the pitching moment coefficients, as explained in the Aerodynamics Appendix. The XFLR5 analysis provided C_m vs α for different center of gravity configurations. The Pitching moment model, which is going to be developed throughout this chapter, is based on the XFLR5 results. It is important to note, that for the future development of the project, a wind tunnel analysis would provide more precise results, and the pitching moment model would be more reliable. This, however, is out of the scope of the project. Therefore, the proposed analysis is a reasonably acceptable approximation for the given circumstances.

At first, C_m vs α graphs analytic equations have been obtained, for the operational range of X_{CG}, achieved by the control system.

$$\begin{cases} C_m(\alpha)\big|_{X_{CG}=0.20} = -0.100 \cdot \alpha + 0.104 \\ C_m(\alpha)\big|_{X_{CG}=0.30} = -0.053 \cdot \alpha + 0.066 \\ C_m(\alpha)\big|_{X_{CG}=0.35} = -0.028 \cdot \alpha + 0.048 \\ C_m(\alpha)\big|_{X_{CG}=0.40} = -0.006 \cdot \alpha + 0.028 \\ C_m(\alpha)\big|_{X_{CG}=0.42} = \quad 0.005 \cdot \alpha + 0.020 \\ C_m(\alpha)\big|_{X_{CG}=0.44} = \quad 0.016 \cdot \alpha + 0.011 \end{cases}$$

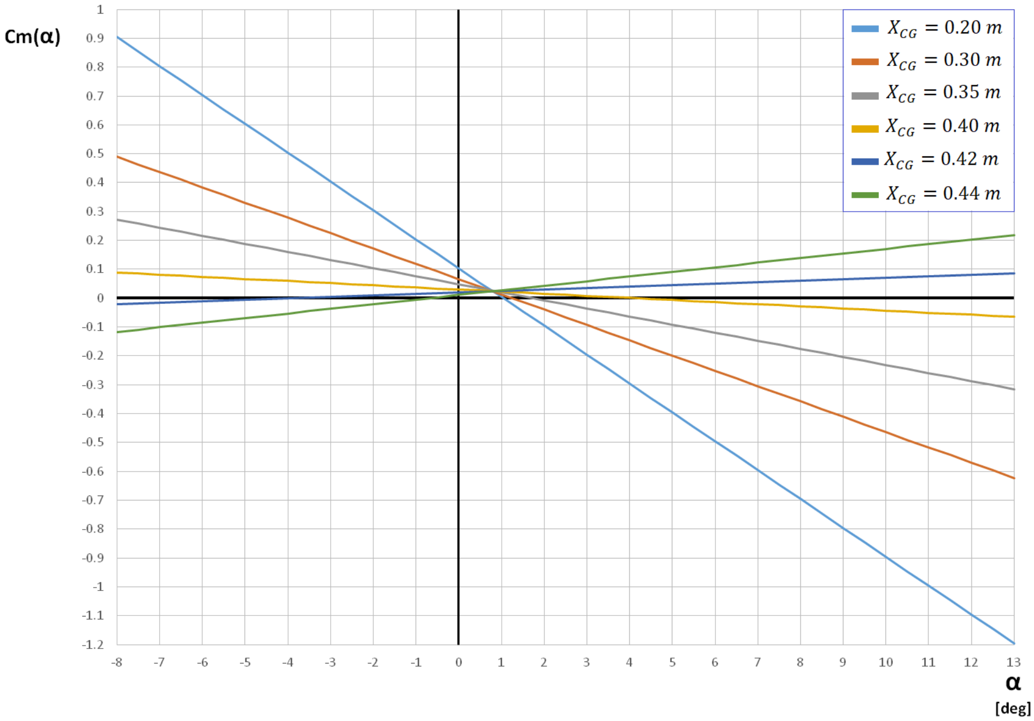

Figure 2.97: C_m vs α graphs for different X_{CG} positions, according to XFLR5 analysis

The previous linear equations can be generalized, if each equation slope and vertical intercept point are written as a function of X_{CG}. The resulting general form equation would be:

$$C_m(\alpha, x) = m(x) \cdot \alpha + n(x) \tag{2.106}$$

where $m(x)$ is the slope as a function of the center of gravity position, and $n(x)$ is the vertical intercept point as a function of the center of gravity position. Analyzing the previous equations, and plotting their slope and vertical interception point for each X_{CG}, the next graphs are obtained.

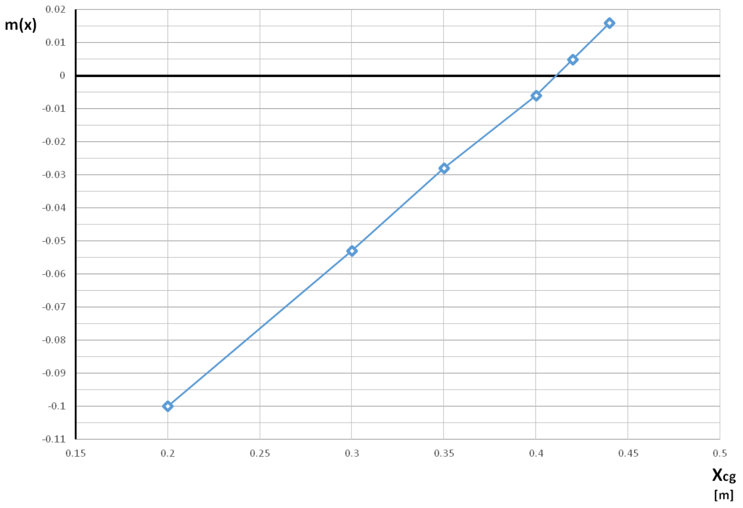

Figure 2.98: Slope versus center of gravity x_b component variation: $m(x)$ vs X_{CG}

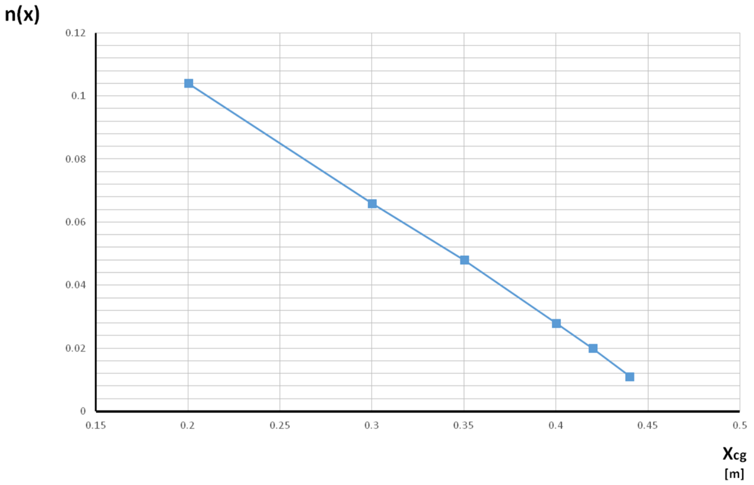

Figure 2.99: Vertical intercept versus center of gravity x_b component variation: $n(x)$ vs X_{CG}

Adjusting a tendency line to the obtained data provides the next results:

$$m(x) = 0.4796 \cdot x - 0.1963$$

and

$$n(x) = -0.3846 \cdot x + 0.1814$$

Therefore, the final equation for the pitching moment coefficient can be written as:

$$C_m(\alpha, x) = \Big((0.4796 \cdot x - 0.1963)\boldsymbol{\alpha} + (-0.3846 \cdot x + 0.1814)\Big) \tag{2.107}$$

and for $X_{CG} = x_s$ the pitching moment would be:

$$M\Big|_{X_{CG}=x_s} = \frac{\rho u_\infty^2 S\bar{c}}{2}\Big((0.4796 \cdot x_s - 0.1963)\boldsymbol{\alpha} + (-0.3846 \cdot x_s + 0.1814)\Big) \tag{2.108}$$

Therefore, for a given angle of attack, it is possible to determine the pitching moment depending on the center of gravity x_b component. Additionally, the flight controller can also calculate the required ΔX_{CG} according to the angle of attack and the pitch rate.

2.4.16.3 Lateral Stability Control System

The lateral stability control system, as introduced on the Systems Appendix, consists of a mobile box which contains the drive batteries. The system is moved over the aircraft y_b axis, when the box is pulled by one of the motors. At the System Appendix, the required power calculation is explained for the maximum load factor and at $\beta = 90°$. In this section, however, the moving box dynamics will be studied for steady conditions.
Considering $\beta = 0°$, and neglecting the box friction with the air (inside the aircraft), the Newton's law on the y_b can be written as:

$$-F_{fr} + F_m = m \cdot a_{y_{box}} \tag{2.109}$$

where F_{fr} is the friction force between the box and the plastic rails, F_m is the spindle pulling force or the string tension.
The first term can be rewritten as:

$$F_{fr} = \mu_{d_{ABS}} \cdot N = \mu_{d_{ABS}} \cdot m \cdot g \tag{2.110}$$

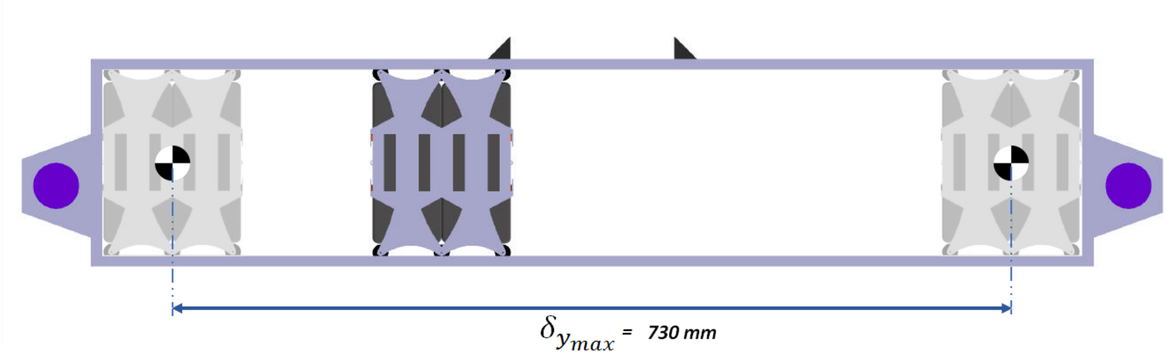

Figure 2.100: Lateral Control System

The mobile box movement is allowed in the range $-365mm < y < 365mm$, which equals to a maximum displacement of $\delta_{y_{max}} = 730mm$, as illustrated in the figure 2.100.
As a design criteria, few considerations have been established:

- The initial and final speed of the box is considered null. Even though this complicates the required power and acceleration calculation, it provides precise and safe control. Also, the system is unlikely to collapse when the movement direction is intended to change.
- The acceleration and deceleration process is considered to be for 0.5 seconds each.
- Acceleration stops when a speed of 0.2 $[m/s]$ is reached.

According to the previous conditions, the resulting acceleration is $a_{y_{box}} = \ddot{\delta}_{y_{acc}} = 0.4\ [m/s^2]$. The displacement over time can be calculated by the next equation:

$$\delta_y = \delta_{y0} + \dot{\delta}_{y0} \cdot t + \frac{1}{2}\ddot{\delta}_{y_{acc}} \cdot t_{acc}^2 + \frac{1}{2}\ddot{\delta}_{y_{dec}} \cdot t_{dec}^2 + \dot{\delta}_{y_{ct}} \cdot (t - t_{acc}) \tag{2.111}$$

which can be simplified to:

$$\delta_{y_{max}} = \frac{0.4}{2}t_{acc}^2 - \frac{0.4}{2}t_{dec}^2 + 0.2(t - t_{acc}) = 0.2(t - t_{acc})$$

Therefore, there are two cases to consider:

- If $\delta_y > 50mm$:
  - there is an acceleration phase of 0.5 seconds and $\ddot{\delta}_{y_{acc}} = 0.4\ [m/s^2]$
  - there is a uniform linear motion at $\dot{\delta}_{y_{ct}} = 0.2\ [m/s]$, during $t_{ct} = t - 2t_{acc}$
  - there is a deceleration phase of 0.5 seconds and $\ddot{\delta}_{y_{acc}} = 0.4\ [m/s^2]$

  Such a case is when $\delta_y = \delta_{max} = 710mm$. The previous equation gives the next result:

  $$t = 4.05\ [s];\quad t_{acc} = t_{dec} = 0.5\ [s];\quad t_{ct} = 3.05\ [s];$$

- If $\delta_y \leq 50mm$, there are only acceleration and deceleration phases, and the corresponding times are calculated according to the next equation:

$$t_{acc} = t_{dec} = \sqrt{\frac{\delta_y}{|\ddot{\delta}_{y_{acc}}|}} = \sqrt{\frac{\delta_y}{0.4}} \tag{2.112}$$

At this point, when mobile box acceleration is defined, the dynamics equation can be used to calculate the required torque to pull the box.

$$-\mu_{d_{ABS}} \cdot m \cdot g + F_m = m \cdot \ddot{\delta}_{y_{acc}}$$

$$F_m = 1.5 \cdot 0.4 + 0.4 \cdot 1.5 \cdot 9.81 = 6.49\ [N]$$

The required torque can be calculated as:

$$Q_m = F_m \cdot r_{spindle} = 0.032 \ [N \cdot m]$$

and the required power at 382 RPM (according to the advance speed) is:

$$P_m = F_m \cdot r_{spindle} \approx 1.3 \ [W]$$

The Lateral Stability Control System, illustrated on the next diagram, consists of:

- **Rails** which allow a total displacement of 730 mm.
- **Box (with wheels)** that contains the two batteries of the drive system.
- **One brushless motor** on each side that pulls the box to the corresponding direction.
- **One string spindle** mounted on each motor axis, that spins the string when pulled.

The brushless motors for the control system have been selected based on the required power calculation. Each motor should be able to pull the box of a mass equal to 1.5 kg. At the worst case scenario, when the aircraft is at $\beta = 90°$ and maximum load factor, the string tension is:

$$T_{string} = m \cdot g_{max} = m \cdot n_{max} \cdot g = 1.5 \cdot 7.04 \cdot 9.81 = 103.6 \ [N] \qquad (2.113)$$

The maximum displacement along the rails is:

$$\delta_{y,max} = 730mm \qquad (2.114)$$

The standard shaft diameter of the small brushless motors is considered 3mm. Considering a spindle of a radius of 5mm mounted on the motor, the required torque to pull the string can be calculated:

$$Q_m = T_{string} \cdot r_{spindle} = 0.518 \ [N \cdot m] \qquad (2.115)$$

It seams reasonably acceptable to consider that a displacement speed of 200 mm/s, so the total displacement of 730 mm can be done in less than 5 seconds. This allows to calculate the motor RPM.

$$V_{box} = \omega_m \cdot r_{spindle} \longrightarrow \omega_m = \frac{0.200}{5.0 \cdot 10^{-3}} = 40.0 \ [rad/s] \ = \ 382RPM \qquad (2.116)$$

Then, the required power can be calculated as:

$$P_m = Q_m \cdot \omega_m = 20.72 \ [W] \qquad (2.117)$$

Since the previous calculations were done without considering the surface friction between the wheels and the rails, the A20-34 S EVO motor has been selected, with a nominal power almost three times the required one. The model belongs to the smallest motor family, and weights around 29 grams.
The electronic speed controller recommended by the manufacturer is the X-7-Pro.

Figure 2.101: Hacker A20-34 S motor [32]

Figure 2.102: X-7-Pro Speed Controller [32]

2.4.16.4 Rolling moment model

The center of gravity variation along the y_b-axis, denoted as ΔY_{CG}, generates a rolling moment, denoted as ΔL, due to the lift distribution imbalance. From the XFLR5 analysis, the next figure was been obtained, which illustrates lift distribution along the y_b axis. In order to establish an analytical or numerical relation between ΔY_{CG} and ΔL, some hypothesis have been considered:

- C_L vs α is approximated by a linear function for $-8° < \alpha < 13°$, which covers the operational range of angle of attack.
- The lift distribution $C_L(y)$ for a given angle of attack is considered to be of the same form as the one obtained by the XFLR5 analysis for $\alpha = 4°$. This hypothesis can be accepted since the twist distribution is relatively small.
- The lift distribution $C_L(y)$ will be approximated by a polynomial function, to simplify the computation by an analytical model.

Combining the previous hypothesis, the next equations can be obtained:

$$\begin{cases} C_L(\alpha, y) = h(\alpha) \cdot g(y) \\ C_L(\alpha) = k_1 \cdot \alpha + k_2 \\ C_L(y) \approx p_6 \cdot x^6 + p_5 \cdot x^5 + p_4 \cdot x^4 + p_3 \cdot x^3 + p_2 \cdot x^2 + p_1 \cdot x + p_0 \end{cases} \tag{2.118}$$

At first, the approximated lift distribution function for $C_L(y)$ coefficients are found by discretization, and then a tendency function is adjusted. The result is illustrated by the figure 2.103.

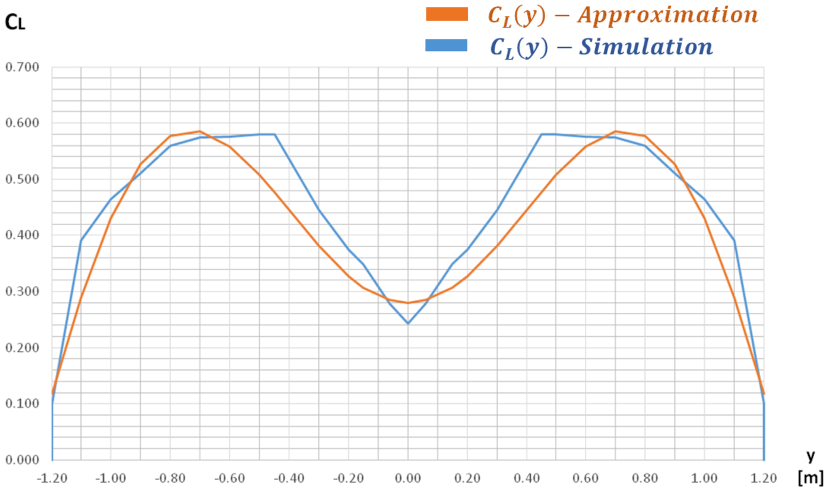

Figure 2.103: Lift distribution: simulation vs approximation

The equation of the lift distribution at $\alpha = 4°$ can be written as:

$$C_L(y)_{4°} = 0.35 \cdot y^6 - 1.45 \cdot y^4 + 1.25 \cdot y^2 + 0.28$$

The next integration provides the total C_L, which is known from the CFD analysis.

$$C_{L4°} = \frac{1}{b} \int_{-\frac{b}{2}}^{\frac{b}{2}} C_L(y)_{4°} dy = 0.3691$$

The next step consists in defining a **general form function** of the $C_L(y)$, which integral is equal to the unit. This can be achieved by dividing the $C_L(y)_{4°}$ by $C_{L4°}$.

$$g(y) = C_L(y)_u = \frac{C_L(y)_{4°}}{C_{L4°}} = 0.95 \cdot y^6 - 3.93 \cdot y^4 + 3.39 \cdot y^2 + 0.76 \qquad (2.119)$$

which verifies:

$$\frac{1}{b} \cdot \int_{-\frac{b}{2}}^{\frac{b}{2}} C_L(y)_u dy = 1$$

Therefore, considering the previous result the next equation has been obtained:

$$h(\alpha) = C_L(\alpha) = k_1\alpha + k_2 = 4.76\alpha + 0.0189 \;\; [\alpha \; in \; rad] \qquad (2.120)$$

where k_1 and k_2 are defined according to the CFD analysis.

Finally, the general lift coefficient equation can be written as:

$$C_L(\alpha, y) = h(\alpha) \cdot g(y) = (4.76\alpha + 0.0189) \cdot (0.95y^6 - 3.93y^4 + 3.39y^2 + 0.76) \qquad (2.121)$$

Now the rolling moment ΔL can be calculated depending on the ΔY_{CG}. For the general calculation, it will be supposed that the center of gravity has been moved to a new point, where $Y_{CG} = y_s$, and $\Delta Y_{CG} = |y_s|$.

- L_{RW} is defined as the rolling moment generated on the right wing side of the Y_{CG}
- L_{LW} is defined as the rolling moment generated on the left wing side of the Y_{CG}

Therefore, the ΔL can be written as:

$$\Delta L = L_{LW} + L_{RW} \tag{2.122}$$

and each term can be calculated as:

$$L_{RW}\big|_{Y_{CG}=y_s} = -\frac{\rho S u_\infty^2}{2b} \cdot \int_{y_s}^{\frac{b}{2}} C_L(\alpha, y)(y - y_s)dy =$$

$$= -\frac{\rho S u_\infty^2}{2b} \cdot \int_{y_s}^{\frac{b}{2}} (4.76\alpha + 0.0189) \cdot (0.95y^6 - 3.93y^4 + 3.39y^2 + 0.76)(y - y_s)dy =$$

$$\cdots$$

$$= -\frac{\rho S u_\infty^2}{2b}(4.76\alpha + 0.0189) \cdot \big(0.218 + 0.0169{y_s}^8 - 0.131{y_s}^6 + 0.2825{y_s}^4 + 0.38{y_s}^2 - 0.6428y_s\big) \tag{2.123}$$

Analogically, the L_{LW} moment can be calculated:

$$L_{LW}\big|_{Y_{CG}=y_s} = -\frac{\rho S u_\infty^2}{2b} \cdot \int_{-\frac{b}{2}}^{y_s} C_L(\alpha, y)(y - y_s)dy =$$

$$= -\frac{\rho S u_\infty^2}{2b} \cdot \int_{-\frac{b}{2}}^{y_s} (4.76\alpha + 0.0189) \cdot (0.95y^6 - 3.93y^4 + 3.39y^2 + 0.76)(y - y_s)dy =$$

$$\cdots$$

$$= -\frac{\rho S u_\infty^2}{2b}(4.76\alpha + 0.0189) \cdot \big(-0.218 - 0.0169{y_s}^8 + 0.131{y_s}^6 - 0.2825{y_s}^4 - 0.38{y_s}^2 - 0.6428y_s\big) \tag{2.124}$$

Therefore, the net rolling moment, ΔL, is:

$$\Delta L\Big|_{Y_{CG}=y_s} = \frac{\rho S u_\infty^2}{2b}(4.76\alpha + 0.0189) \cdot 1.2856 y_s \tag{2.125}$$

This means that given the angle of attack and the center of gravity displacement over the y_b axis, the processor can determine the generated rolling moment. What is even more important, is that the flight controller can also calculate the required ΔY_{CG} according to the angle of attack and the desired roll rate.

In the next chapters, the Center of Gravity and Inertia Tensors variations will be studied, with the objective of obtaining their relationship to the mass-actuator displacements δ_x and δ_y.

2.4.17 Center of Gravity Variation

2.4.17.1 X_{CG} variation

The variation of the center of gravity x_b component will be studied considering the movement of the longitudinal control system box. The system consists of the system components (400g), plastic box(28.7g), rack (12.7g) and wheels (4.8g), which make a total mass of approximately 450 grams. The center of gravity of the fixed components does not change. Also, the center of gravity of the lateral control system only changes on the y_b axis, which does not affect on the X_{CG}. Therefore, the $X_{CG} = x_s$ can be calculated:

$$X_{CG} = x_s = \sum_{n=1}^{\infty} \frac{m_i \cdot x_i}{m_t} = \frac{3550 \cdot X_{CG_{fix}} + 450 \cdot (\delta_x + \delta_{x_0})}{4000} \tag{2.126}$$

It is important to note that all the distances over the x_b axis are going to be calculated from the aircraft nose.

$X_{CG_{fix}}$ is determined by the CATIA V5 software. During the design process, some components size, weight and position has been adjusted with to objective of getting the $X_{CG_{fix}}$ close to the desired 0.4 m (see Aerodynamics Appendix). Finally, $X_{CG_{fix}} = 0.403\ m$ was achieved.

The control system rails begin at $X = 260mm$, however the initial position of the control system center of mass starts at $\delta_{x_0} = 290mm$.

$$X_{CG} = x_s = \frac{3550 \cdot 403 + 450 \cdot (\delta_x + 290)}{4000} = 390.3 + 0.1125 \cdot \delta_x$$

Considering that $\delta_{x_{min}} = 0mm$ and $\delta_{x_{max}} = 180mm$, the next results are obtained:

$$X_{CG_0} = 390.3 + 0.1125 \cdot \delta_{x_{min}} \approx 390.3\ [mm]$$

$$X_{CG_{max}} = 390.3 + 0.1125 \cdot \delta_{x_{max}} \approx 410.6 \ [mm]$$

Therefore, the maximum variation of the center of gravity on the x_b axis is:

$$\Delta X_{CG} = X_{CG_{max}} - X_{CG_0} = 20.3 \ [mm]$$

It is important to note that, according to the previous analysis of the C_m vs α graphs, the X_{CG} variation seems to be enough for the control, since it allows to move the center of gravity from the statically stable domain to the statically unstable domain, through the neutral point, and vice-verse. Throughout the next chapters, a deeper static stability and control analysis will be discussed, which will confirm, precisely, whether the ΔX_{CG} is enough or not.

2.4.17.2 Y_{CG} variation

The symmetrical distribution of all the components, besides the lateral control system mobile box, makes the center of gravity to be on the symmetry plane. Thus, $Y_{CG_0} = 0$ on the y_b axis. The lateral control system mobile box, which includes two batteries (1500g), plastic box (32g) and wheels (14g), has a total mass of 1546 grams. Therefore, the $Y_{CG} = y_s$ can be calculated as:

$$Y_{CG} = y_s = \sum_{n=1}^{\infty} \frac{m_i \cdot y_i}{m_t} = \frac{2454 \cdot 0 + 1546 \cdot \delta_y}{4000} = \frac{1546 \cdot \delta_y}{4000} = 0.3865 \cdot \delta_y \qquad (2.127)$$

and

$$\Delta Y_{CG} = Y_{CG} - Y_{CG_0} = 0.3865 \cdot \delta_y \qquad (2.128)$$

Since $\delta_{y_{max}} = 365mm$ and $\delta_{y_{min}} = -365mm$, the maximum variation on the center of gravity y_b coordinate is:

$$\Delta Y_{CG_{max}} = 0.3865 \cdot \delta_{y_{max}} = 141 \ [mm]$$

2.4.18 Inertia Tensor Variation

The majority of studies regarding the inertia tensor variation involve slight and symmetrical change in the mass distribution, which makes reasonable to consider a fixed center of gravity. This enables straightforward solutions my analytic or numerical methods. However, the current project is not compatible with such hypothesis and simplifications. Once Y_{CG} is moved out of the symmetry plane, the components J_{xy} and J_{yz} can not be neglected, and the Steiner theorem is not applicable for these components. Therefore, there are two possibilities for the inertia tensor calculation:

- The most precise approach would be to obtain the inertia tensor and its variation by an experimental method, which consists in suspending the aircraft by two strings, applying a moment on the axis of consideration and analyzing the oscillation period. Then, the next equation can be used to calculate the moment of inertia on that axis:

  $$I = \frac{mgd^2}{4\pi^2 l} T^2 \tag{2.129}$$

  where T is the period of oscillation, l is the length of the string, and $d = 2R$ is the separation between the parallel strings. The setup is illustrated on the Figure 2.104 Obviously, this process requires the construction of a prototype, which is out of the scope of the current project.

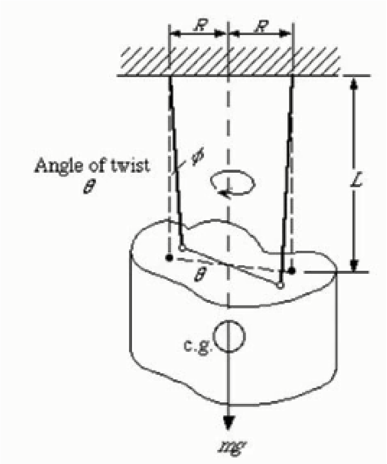

Figure 2.104: Bifilar pendulum method for experimental determination of moment of inertia

- The other alternative consists in a numerical analysis, by a computer aided design software, which in this case has been the CATIA V5. Once all the components of the assembly are designed and the corresponding weight is assigned, the software provides the inertia tensor components regarding the axis system based on the center of gravity. The process consists in registering all the components of the inertia tensor in a spreadsheet for a given center of gravity position. The process should be repeated for different positions of the center of gravity. Additionally, and with the objective of having an analytical model of the inertia tensor, the obtained results should be plotted and a tendency function should be obtained, such as:

  $$I_i = f_i(x_s, y_s)$$

  where x_s and y_s are the coordinates of the center of gravity.

At first place, the required data has been obtained and populated in a spreadsheet, as shown in the following table. In total five tables have been generated (see Report Attachment [1] [$X_{CG} = 0.390m$, $X_{CG} = 0.395m$, $X_{CG} = 0.400m$, $X_{CG} = 0.405m$, $X_{CG} = 0.410m$]. Inertia tensor components have been analyzed one by one.

$X_{CG} = 0.390m$						
Y_{CG}	I_x	I_y	I_z	I_{xy}	I_{xz}	I_{yz}
0.000	0.354	0.151	0.498	0	-0.023	0
0.015	0.355	0.151	0.499	8.61E-04	-0.023	1.14E-04
0.030	0.36	0.151	0.504	0.0015	-0.023	2.28E-04
0.045	0.368	0.151	0.512	0.0025	-0.023	3.43E-04
0.060	0.378	0.151	0.522	0.003	-0.023	4.57E-04
0.075	0.392	0.151	0.536	0.004	-0.023	5.72E-04
0.090	0.409	0.151	0.553	0.005	-0.023	6.86E-04
0.105	0.429	0.151	0.573	0.006	-0.023	8.01E-04
0.120	0.451	0.151	0.595	0.007	-0.023	9.15E-04
0.141	0.481	0.151	0.625	0.008	-0.023	0.001

Table 2.12: I vs Y_{CG} at $X_{CG} = 0.390m$

2.4.18.1 I_x analysis

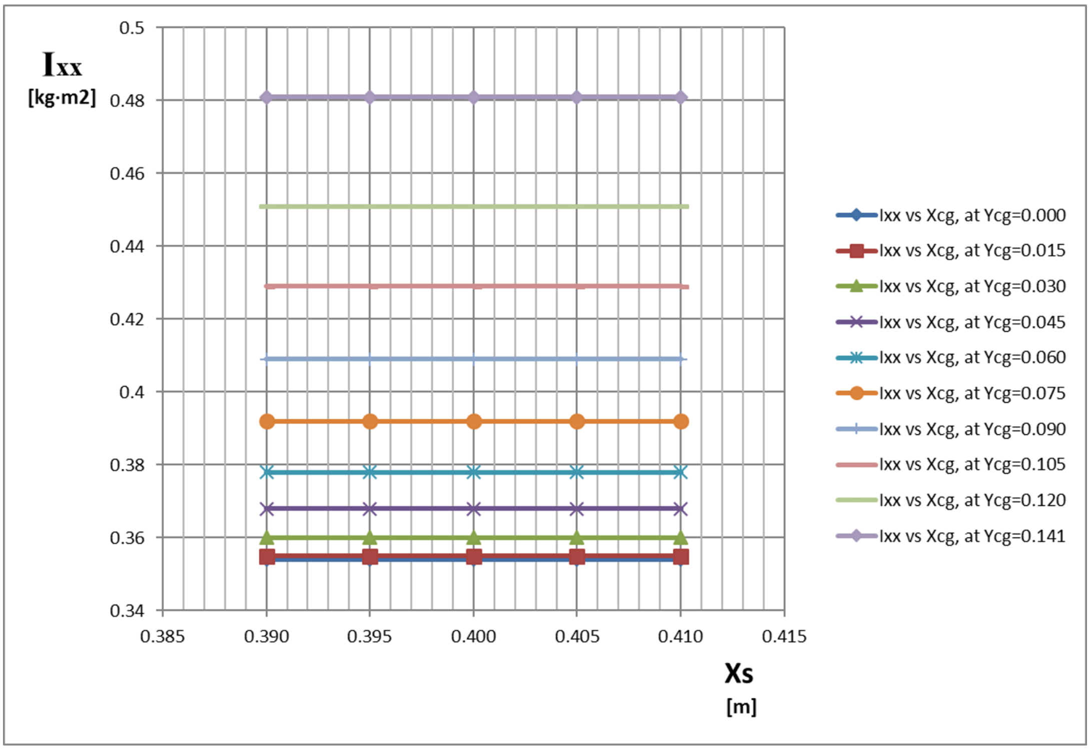

Figure 2.105: I_x variation versus X_{CG}, for different Y_{CG} positions

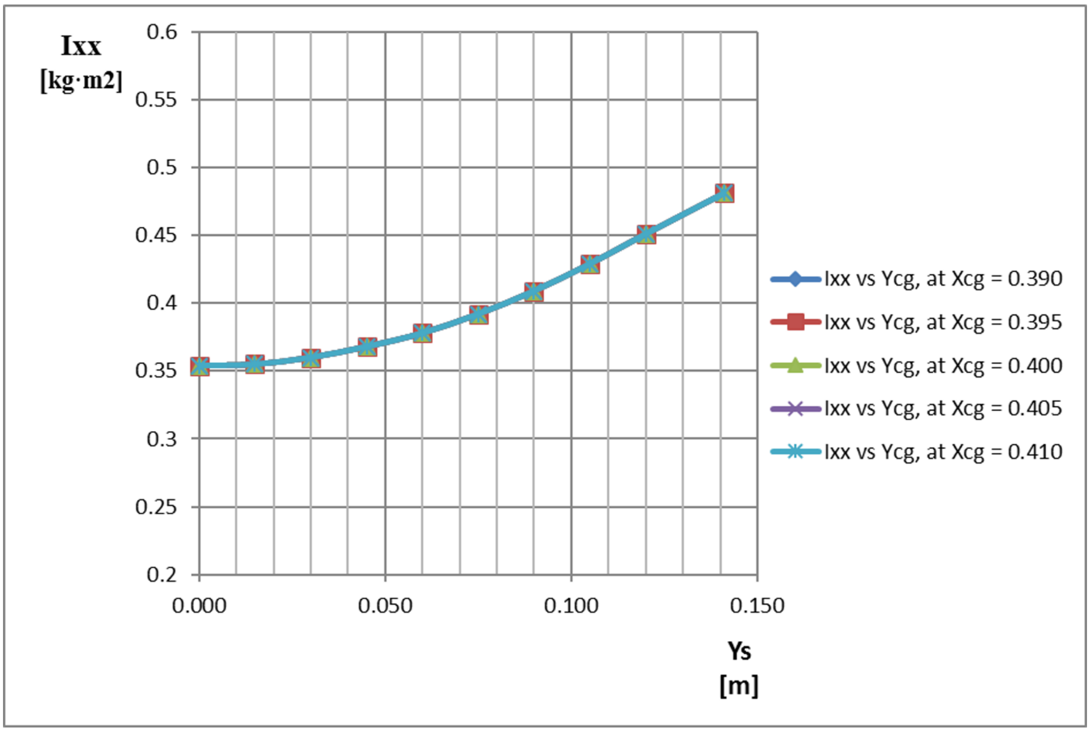

Figure 2.106: I_x variation versus Y_{CG}, for different X_{CG} positions

The analysis of the previous plots shows that, as expected, I_x remains constant against X_{CG} variations. On the contrary, it changes when Y_{CG} is changed. This permits to adjust a tendency polynomial function to the I_x vs Y_{CG} graph:

$$I_x = f(\cancel{x_s}, y_s) = 5.9826 \cdot y_s^2 + 0.0819 \cdot y_s + 0.3528 \quad [kg \cdot m^2]$$

for

$$-0.141m < y_s < 0.141m$$

2.4.18.2 I_y analysis

The analysis of figures 2.107 and 2.108 shows that I_y remains constant against Y_{CG} variations, which is as expected. On the contrary, it changes when X_{CG} is changed. This permits to adjust a tendency polynomial function to the I_y vs X_{CG} graph:

$$I_y = f(x_s, \cancel{y_s}) = 28.571 \cdot x_s^2 - 24.857 \cdot x_s + 5.4996 \quad [kg \cdot m^2]$$

for

$$0.390m < x_s < 0.410m$$

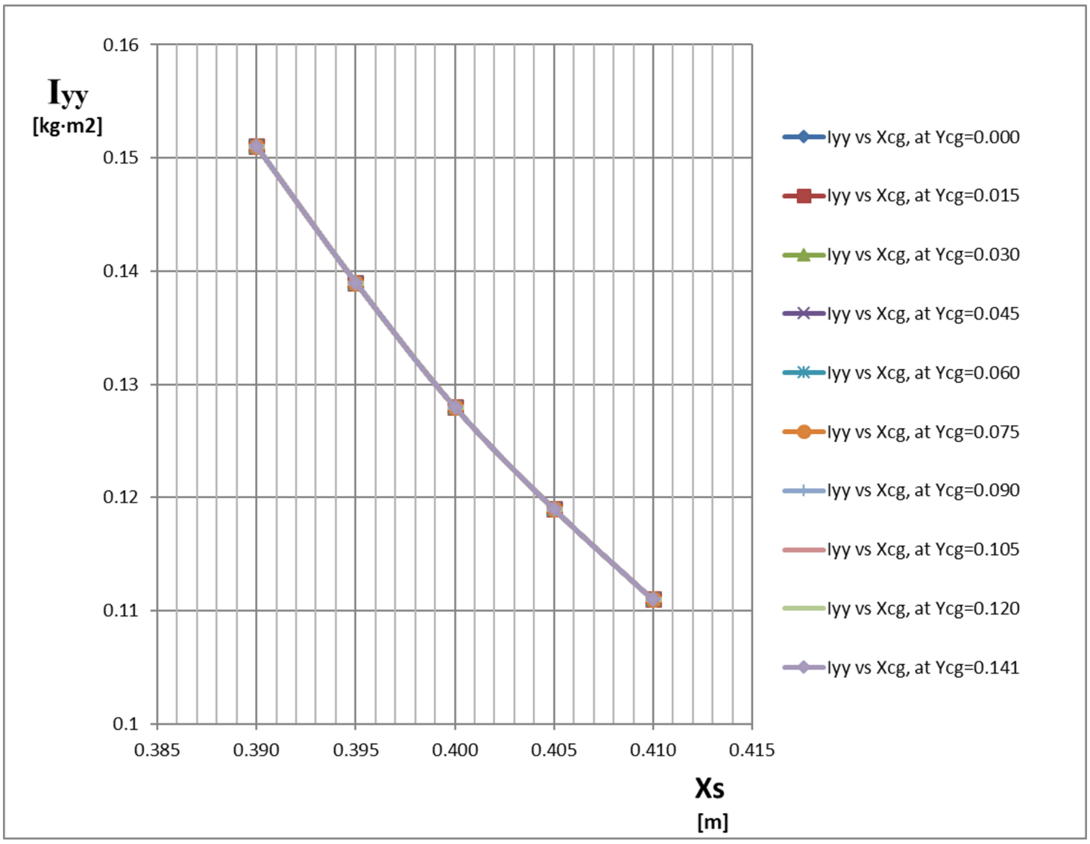

Figure 2.107: I_y variation versus X_{CG}, for different Y_{CG} positions

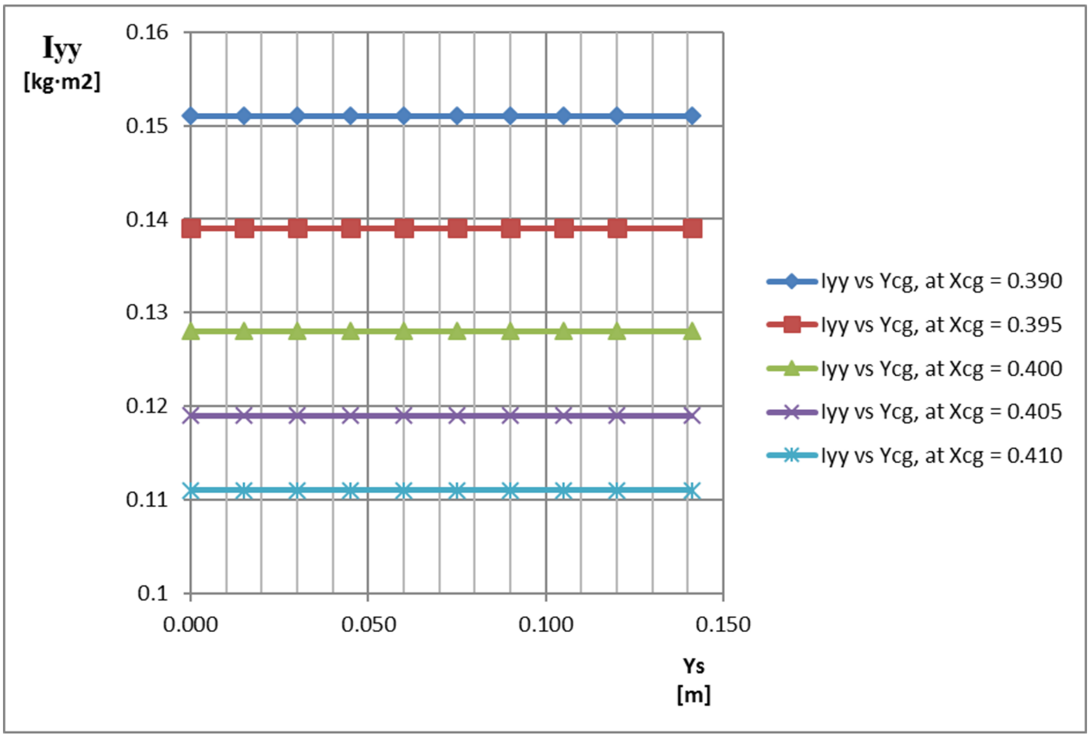

Figure 2.108: I_y variation versus Y_{CG}, for different X_{CG} positions

2.4.18.3 I_z analysis

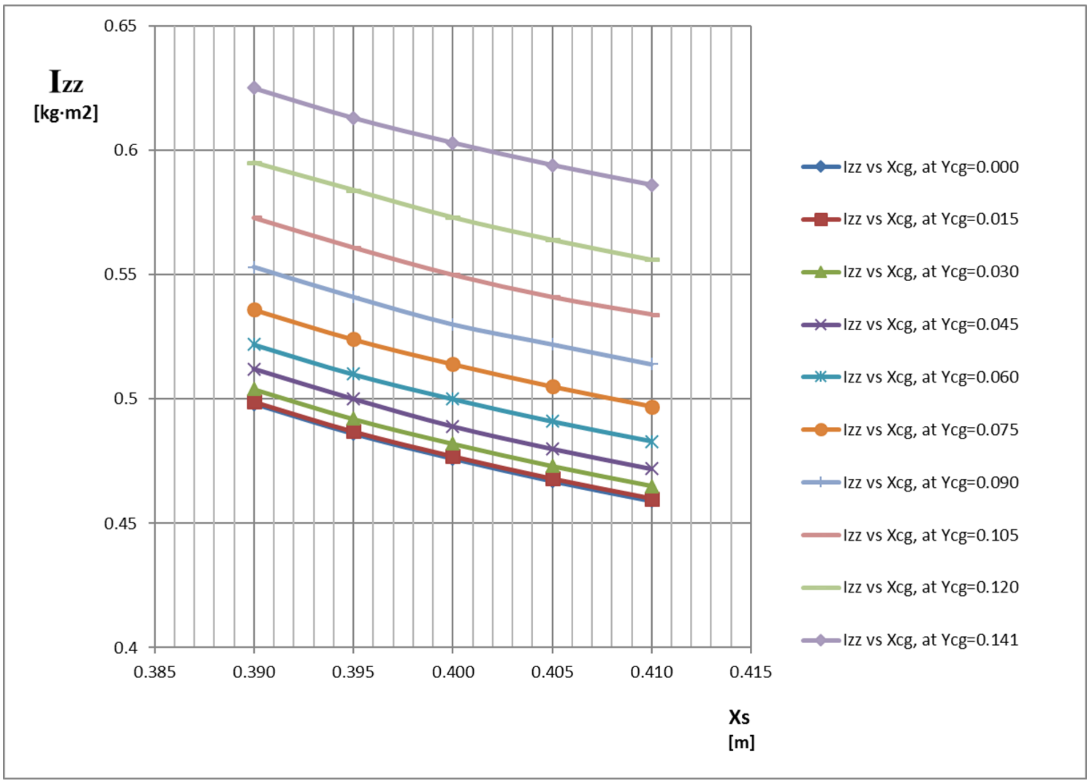

Figure 2.109: I_z variation versus X_{CG}, for different Y_{CG} positions

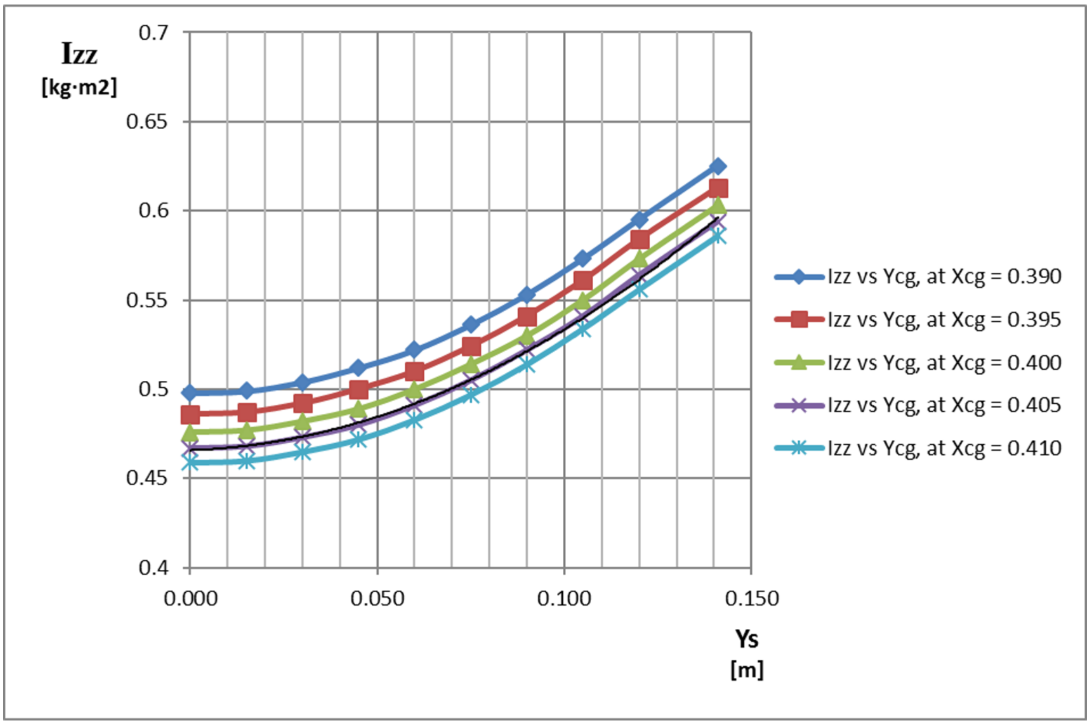

Figure 2.110: I_z variation versus Y_{CG}, for different X_{CG} positions

The analysis of the previous plots shows that I_z changes against X_{CG} and Y_{CG} variations, and therefore the tendency function should be multi-variable. The I_z variation against the changes on the center of gravity x_b coordinate seems to be close to linear, for a constant Y_{CG}. On the other hand, I_z versus Y_{CG} shows quadratic function behavior, for a constant X_{CG}. The analysis is centered on the I_z versus X_{CG} graphs, which are close to linear, and the next equation is considered:

$$I_z = f(x_s, y_s) = m(y_s) \cdot x_s + n(y_s)$$

where $m(y_s)$ is the slope of each line, depending on the Y_{CG}, and $n(y_s)$ is the vertical intercept point of each line. Then, for each line a tendency function is traced, and the correspondent m and n values are registered. The slope of each line seems constant regardless of the Y_{CG}, and it is considered to be $m \approx -1.940$. Therefore, only n vs y_s plot has been generated.

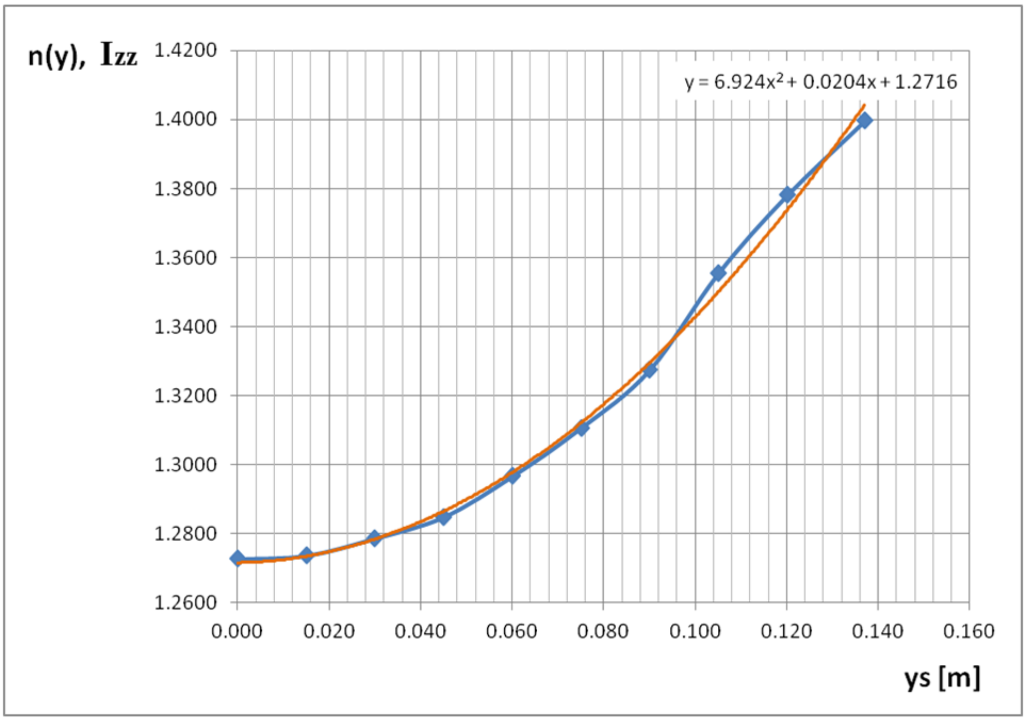

Figure 2.111: I_z analysis: $n(y_s)$, as a vertical interception point function, versus Y_{CG}

The adjusted tendency function to the $n(y_s)$ vs y_s plot is a second order polynomial:

$$n(y_s) = 6.924 \cdot y_s^2 + 0.0204 \cdot y_s + 1.2716$$

Therefore, the final equation for the I_z can be written as:

$$I_z = f(x_s, y_s) = m(y_s) \cdot x_s + n(y_s) = -1.904 \cdot x_s + 6.924 \cdot y_s^2 + 0.0204 \cdot y_s + 1.2716$$

$$x_s \in \big[0.390m; 0.410m\big] \qquad y_s \in \big[-0.141m; 0.141m\big]$$

which also matches the I_z vs y_s quadratic behavior as illustrated in the Figure 2.110.

2.4.18.4 I_{xy} analysis

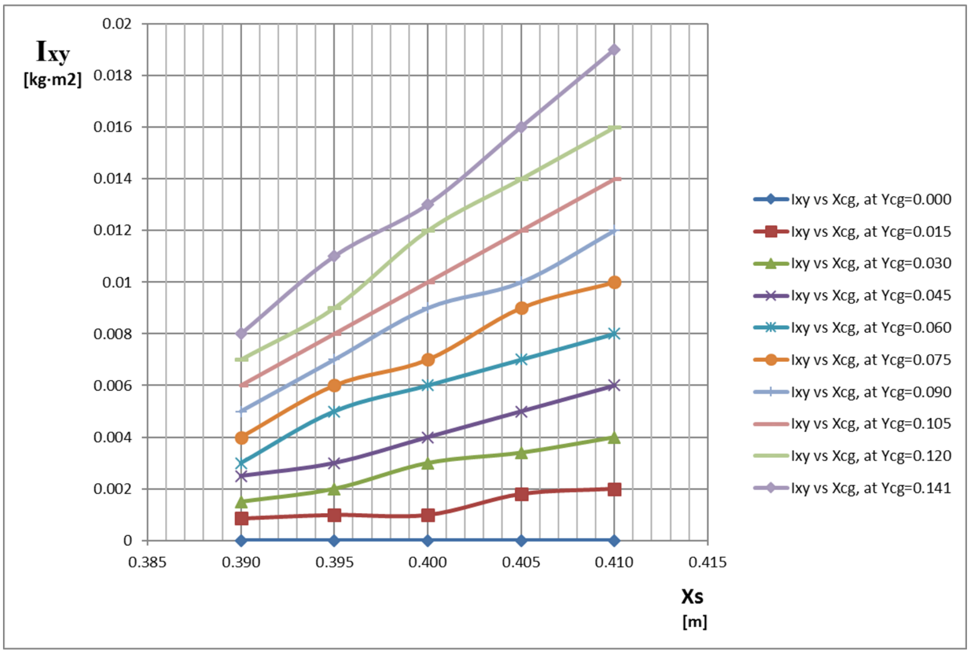

Figure 2.112: I_{xy} variation versus X_{CG}, for different Y_{CG} positions

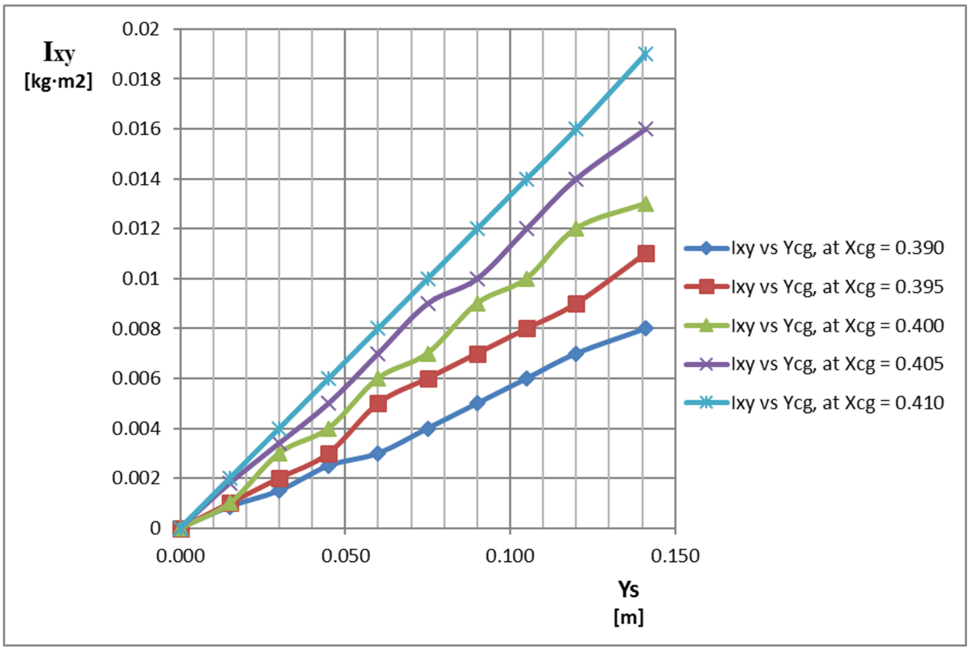

Figure 2.113: I_{xy} variation versus Y_{CG}, for different X_{CG} positions

The analysis of the previous plots shows that, I_{xy} changes regarding X_{CG} and Y_{CG}variations. The plots have a linear behavior, including a slight oscillation around a tendency line. For a convenience in the calculations, the I_{xy} versus Y_{CG} plots are considered, where the tendency lines pass through $O(0.0)$. The next equation is considered:

$$I_{xy} = f(x_s, y_s) = m(x_s) \cdot y_s + \cancel{n(x_s)} = m(x_s) \cdot y_s$$

Then, for each line a tendency function is traced, and the correspondent m values are registered. It is important to note, that since the tendency lines pass through $O(0.0)$, $n(x_s)$ is neglected. Then, m vs x_s plot has been traced, as shown on the next figure:

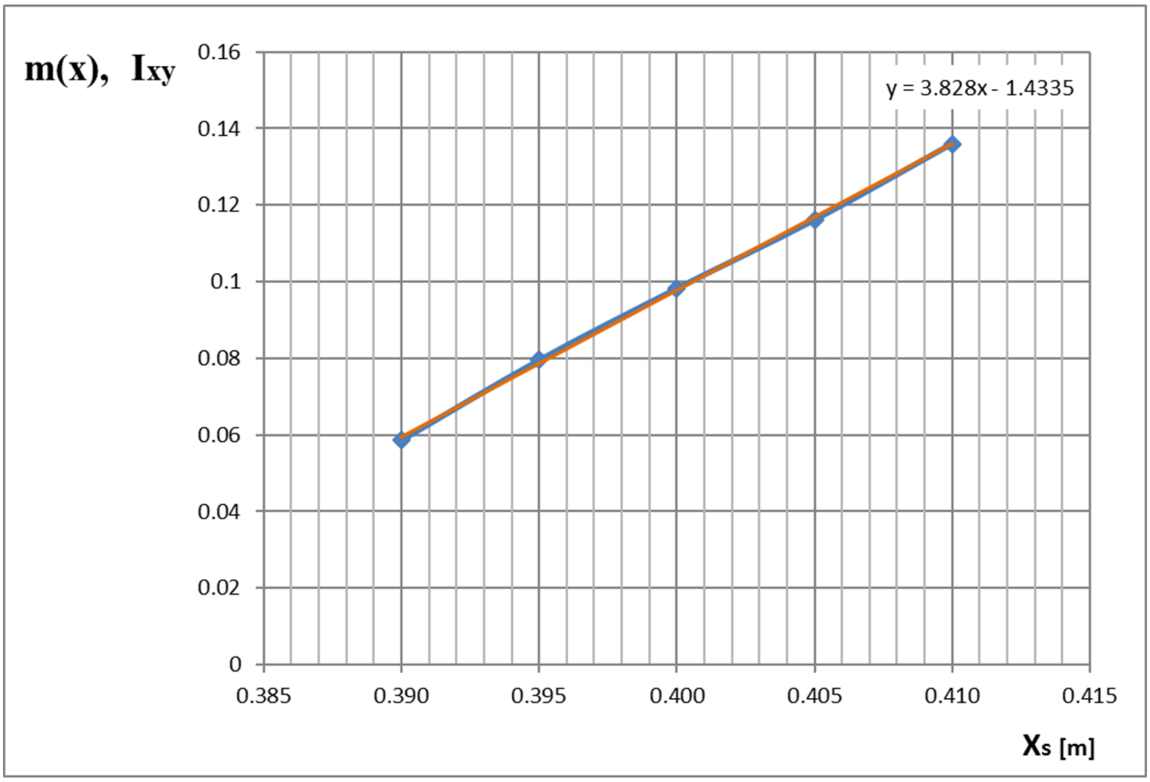

Figure 2.114: I_{xy} analysis: slope variation versus X_{CG}

From the plot it can be concluded that:

$$m(x_s) = 3.828 \cdot x_s - 1.4335$$

And the final function for the I_{xy} can be written as:

$$I_{xy} = f(x_s, y_s) = m(x_s) \cdot y_s = \big(3.828 \cdot x_s - 1.4335\big) \cdot y_s \quad [kg \cdot m^2]$$

$$x_s \in \big[0.390m; 0.410m\big] \qquad y_s \in \big[-0.141m; 0.141m\big]$$

2.4.18.5 I_{xz} analysis

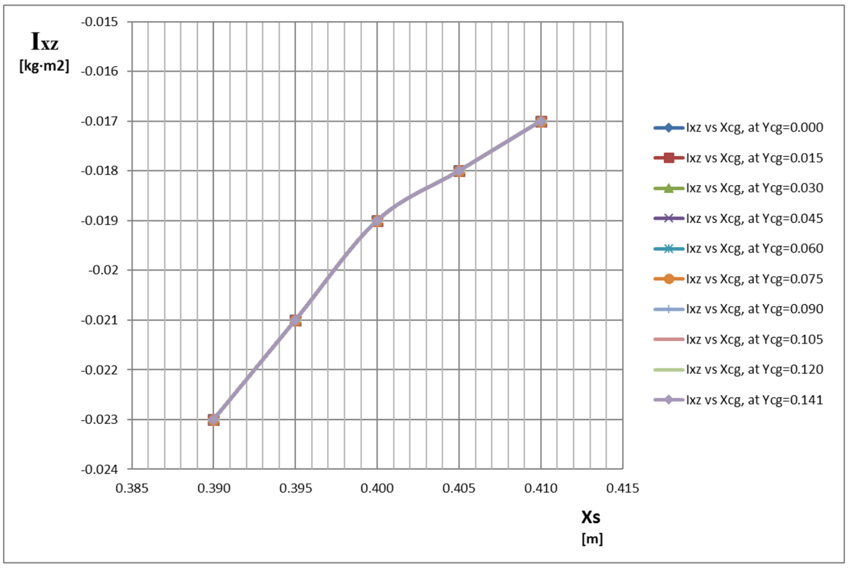

Figure 2.115: I_{xz} variation versus X_{CG}, for different Y_{CG} positions

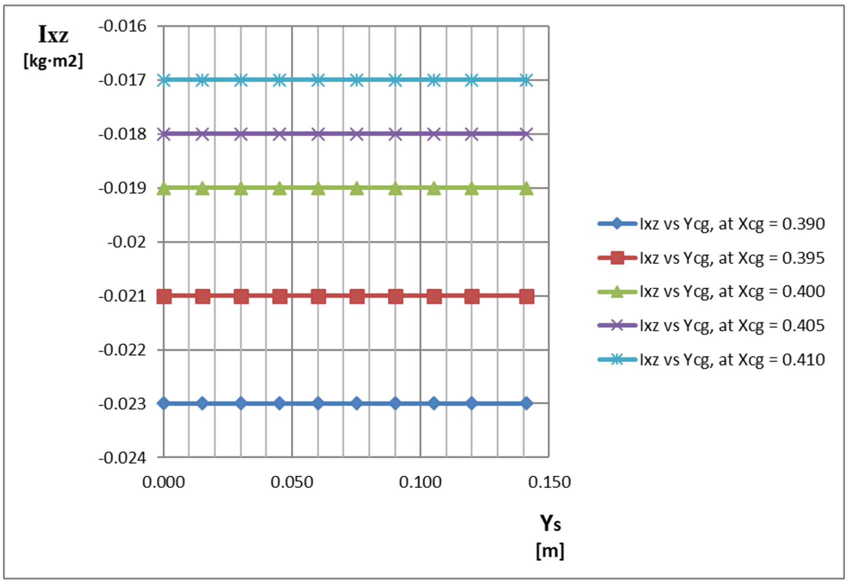

Figure 2.116: I_{xz} variation versus Y_{CG}, for different X_{CG} positions

The analysis of the previous plots shows that, as expected, I_{xz} changes only against X_{CG} variations. This permits to adjust a tendency polynomial function to the I_{xz} vs X_{CG} graph:

$$I_{xz}(x_s, y_s) = f(x_s, \cancel{y_s}) = -8.5714 \cdot x_s^2 + 7.1571 \cdot x_s - 1.5106 \quad [kg \cdot m^2]$$

for

$$0.390m < x_s < 0.410m$$

2.4.18.6 I_{yz} analysis

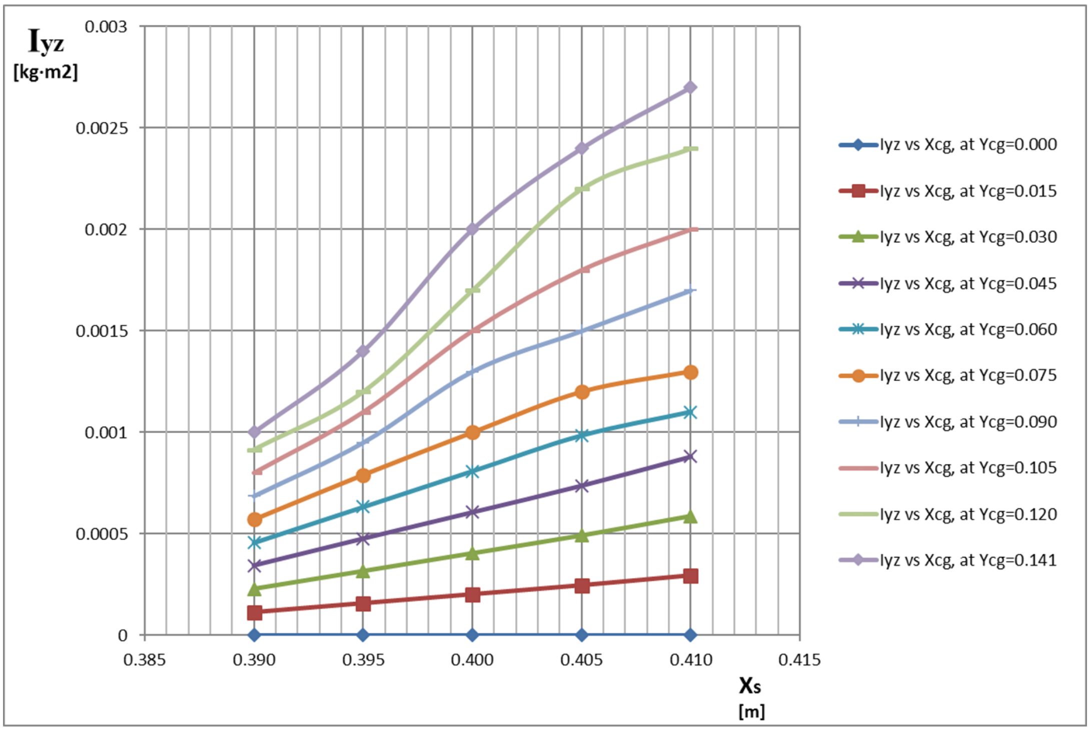

Figure 2.117: I_{yz} variation versus X_{CG}, for different Y_{CG} positions

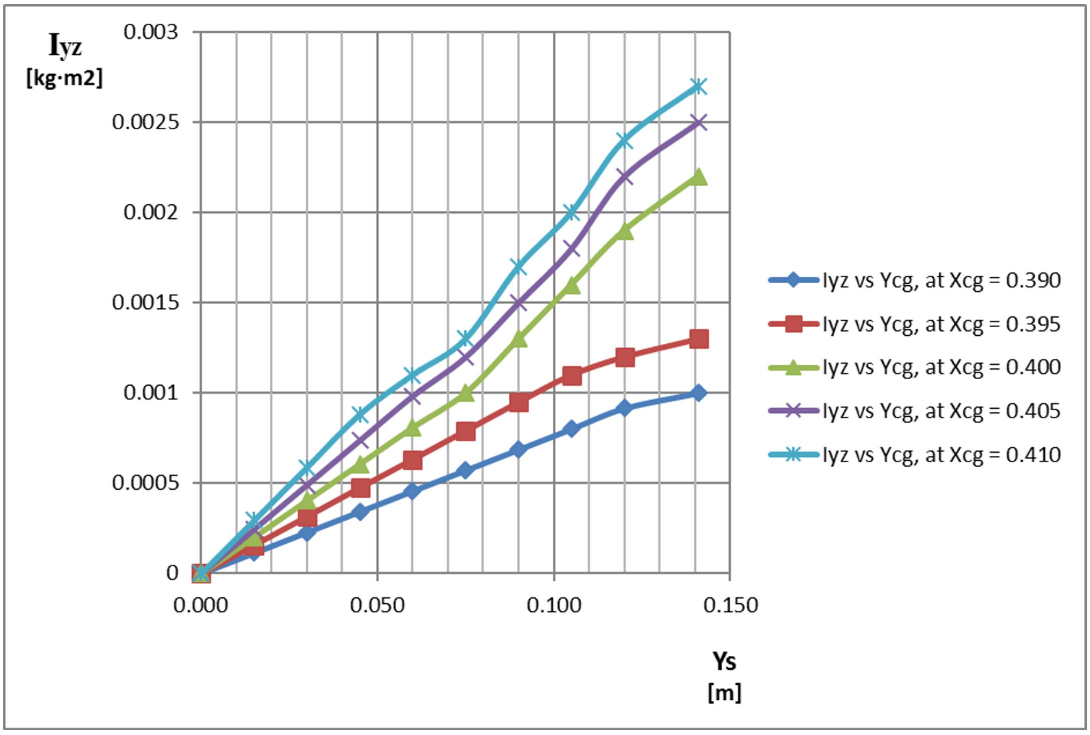

Figure 2.118: I_{yz} variation versus Y_{CG}, for different X_{CG} positions

The analysis of the previous plots shows that, I_{yz} changes regarding X_{CG} and Y_{CG}variations. The plots have approximately linear behavior regarding the Y_{CG}, however regarding the X_{CG} variations it seems unclear. Therefore, mainly the I_{yz} versus Y_{CG} plots are considered. The next equation is considered:

$$I_{yz} = f(x_s, y_s) = m(x_s) \cdot y_s + \cancel{n(x_s)} = m(x_s) \cdot y_s$$

Then, for each line a tendency function is traced, and the correspondent m values are registered. It is important to note, that since the tendency lines pass through $O(0.0)$, $n(x_s)$ is neglected. Then, m vs x_s plot has been traced, as shown on the next figure:

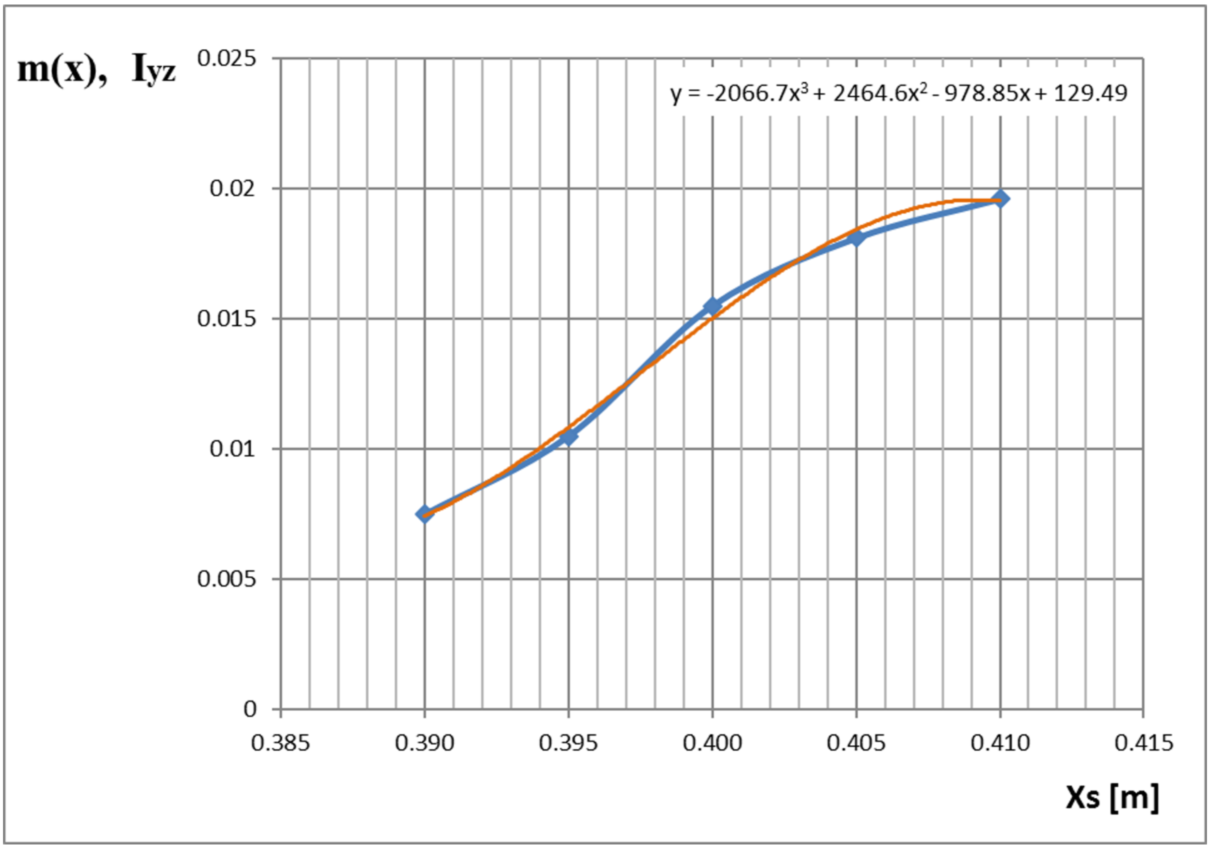

Figure 2.119: I_{yz} analysis: slope variation versus X_{CG}

From the plot it can be concluded that:

$$m(x_s) \approx -2066.7 \cdot x_s^3 + 2464.6 \cdot x_s^2 - 978.85 \cdot x + 129.49$$

And the final function for the I_{yz} can be written as:

$$I_{yz} = f(x_s, y_s) = m(x_s) \cdot y_s = \big(-2066.7 \cdot x_s^3 + 2464.6 \cdot x_s^2 - 978.85 \cdot x + 129.49\big) \cdot y_s \quad [kg \cdot m^2]$$

$$x_s \in \big[0.390m; 0.410m\big] \qquad y_s \in \big[-0.141m; 0.141m\big]$$

which also may explain the behavior of I_{yz} vs X_{CG} as illustrated in the Figure 2.117.

2.4.19 Control System: summary of results

- Longitudinal stability control system

$$\begin{cases} \delta_x(t) = 0.09 \cdot t + 0.29 \\ 0.0m < \delta_x < 0.180m \\ X_{CG} = x_s = 390.3 + 0.1125 \cdot \delta_x \\ 0.390m < x_s < 0.410m \\ M\Big|_{X_{CG}=x_s} = \dfrac{\rho u_\infty^2 S\bar{c}}{2}\Big((0.4796 \cdot x_s - 0.1963)\boldsymbol{\alpha} + (-0.3846 \cdot x_s + 0.1814)\Big) \end{cases}$$

- Lateral stability control system

$$\begin{cases} \delta_{y_{max}} = \pm 0.2(t - t_{acc}) \\ -0.365m < \delta_y < 0.365m \\ Y_{CG} = y_s = 0.3865 \cdot \delta_y \\ -0.141m < y_s < 0.141m \\ \Delta L\Big|_{Y_{CG}=y_s} = \dfrac{\rho S u_\infty^2}{2b}(4.76\alpha + 0.0189) \cdot 1.2856 y_s \end{cases}$$

- Inertia tensor components variation

$$\begin{cases} I_x = 5.9826 \cdot y_s^2 + 0.0819 \cdot y_s + 0.3528 \\ I_y = 28.571 \cdot x_s^2 - 24.857 \cdot x_s + 5.4996 \\ I_z = -1.904 \cdot x_s + 6.924 \cdot y_s^2 + 0.0204 \cdot y_s + 1.2716 \\ I_{xy} = \big(3.828 \cdot x_s - 1.4335\big) \cdot y_s \\ I_{xz} = -8.5714 \cdot x_s^2 + 7.1571 \cdot x_s - 1.5106 \\ I_{yz} = \big(-2066.7 \cdot x_s^3 + 2464.6 \cdot x_s^2 - 978.85 \cdot x + 129.49\big) \cdot y_s \end{cases}$$

2.4.20 Static Stability and Control

At this chapter the aircraft stability and control will be studied, which includes the study of its behavior as a rigid body and its changes around the center of gravity. Since the study is for steady flight, the problem can be divided into two independent cases, where the longitudinal and lateral stability are discussed separately.

2.4.20.1 Static Longitudinal Stability and Control

For the Static longitudinal stability and control analysis all the lateral-directional variables are considered null $(\beta, \phi, p, r, \delta_y)$, therefore the three dynamics equations (force on the y_b axis, moment around x_b and z_b axis) are identically zero. This means that only the other three dynamics equations must be considered, which are the force equation on the x_b axis, force equation on the z_b axis, and the moment equation around the y_b axis. Furthermore, the general equation of the total pitching moment can be written, for a **conventional airplane**:

$$C_m = C_{m_0} + C_{m_\alpha} \cdot \alpha_{wb} + C_{m_{\delta_e}} \cdot \delta_e \tag{2.130}$$

where δ_e is the deflection of the elevator. For a steady and linear uniform motion at some angle of attack, it is required to set the total pitching moment to zero. Therefore:

$$C_m = C_{m_0} + C_{m_\alpha} \cdot \alpha_{wb} + C_{m_{\delta_e}} \cdot \delta_e = 0$$

which provides a combination of δ_e and $\alpha_{wb} = \alpha_{wb_{eq}}$ as a solution. The longitudinal control study consists in the analysis of the relationship between these two variables. If the flight conditions are required to be changed (normally, the angel of attack or the speed), it is important to evaluate the previous equation according to the new $\alpha_{wb_{eq}}$. Generally, there are three longitudinal control methods:

- **Vertical intercept point change**: C_{m_0} can be changed on the conventional aircraft by flap deflection, which changes the $C_{m_{ac}}$. Therefore, the $\alpha_{wb_{eq}}$ is changed.
- **Center of gravity position change**: this changes the C_{m_α} coefficient, which changes the $\alpha_{wb_{eq}}$ and also the stability index.
- **Elevator deflection**: this changes $C_{m_{\delta_e}} \cdot \delta_e$ term, which also changes the $\alpha_{wb_{eq}}$.

Conventional aircraft normally use the third control method, according to [11]. At the current project only the second method is acceptable. Therefore, the total pitching moment will be considered as:

$$C_m = C_{m_0} + C_{m_\alpha} \cdot \alpha_{wb} = 0 \tag{2.131}$$

In the second chapter, the pitching moment model was discussed, based on the total pitching moment plots obtained from the XFLR5 software, and the linearization of the C_{m_α} as a function of x_s, where x_s represents the instantaneous position of the center of gravity over the x_b axis.

$$M\big|_{X_{CG}=x_s} = \frac{\rho u_\infty^2 S\bar{c}}{2}\Big((0.4796 \cdot x_s - 0.1963)\boldsymbol{\alpha} + (-0.3846 \cdot x_s + 0.1814)\Big)$$

which can be written as:

$$C_m\big|_{X_{CG}=x_s} = (0.4796 \cdot x_s - 0.1963)\boldsymbol{\alpha} + (-0.3846 \cdot x_s + 0.1814)$$

Since $C_m = 0$ is one of the conditions for steady and linear motion, the next results can be obtained:

$$\Big((0.4796 \cdot x_s - 0.1963)\boldsymbol{\alpha} + (-0.3846 \cdot x_s + 0.1814)\Big) = 0$$

and

$$x_s = \frac{0.1963\alpha - 0.1814}{0.4796\alpha - 0.3846}$$

The next plot illustrates the x_s versus α_{eq} graph, where the operational range of x_s given by the longitudinal control system has been marked.

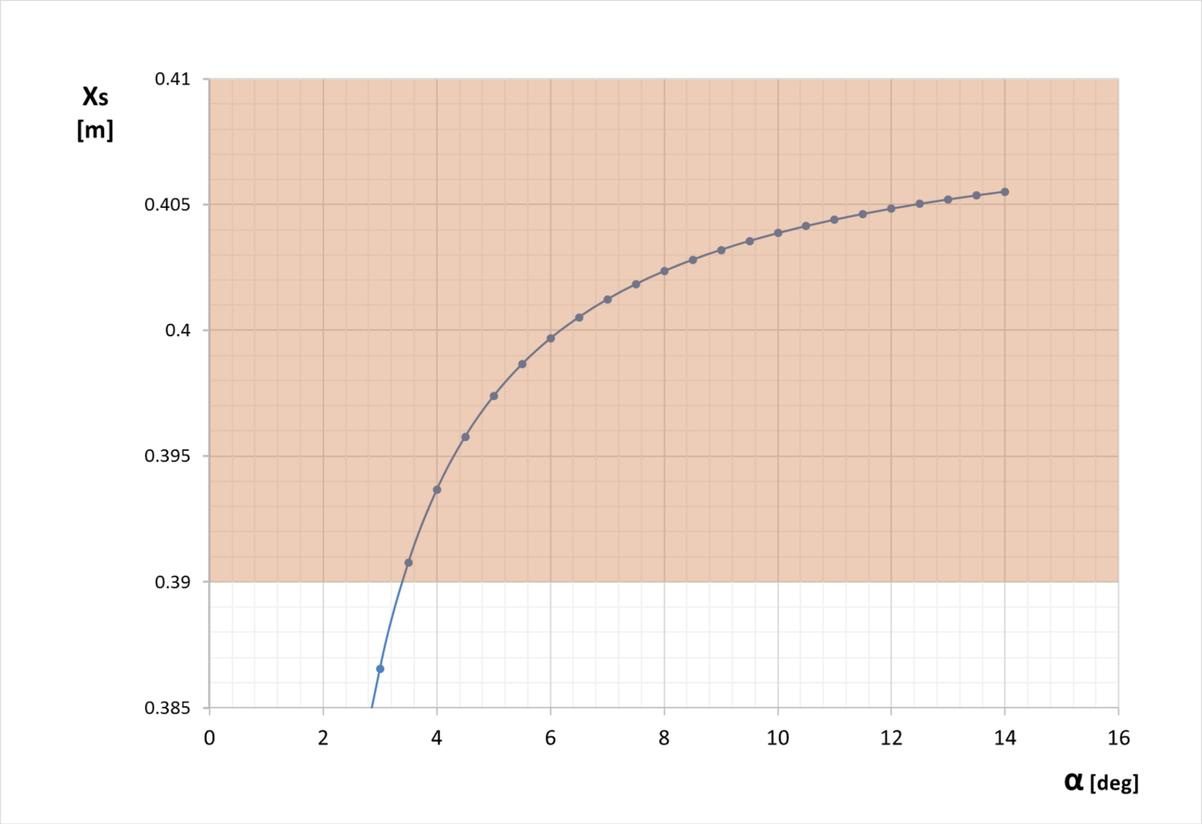

Figure 2.120: Center of gravity X_{CG} position versus equilibrium angle of attack

Based on the previous plot, the conclusion is that the $X_{CG} \in [0.390m, 0.410m]$ covers the equilibrium angle of attack range, from $\alpha_{eq} \approx 3.5°$ to the maximum operational angle of attack $\alpha_{eq} = 13°$. It is important to note that for higher values of X_{CG} it is possible to obtain higher α values, which are not considered due to stall. Furthermore, for $X_{CG} > 0.408m$ the aircraft enters longitudinally unstable phase, which provides extra maneuverability to the aircraft. This, however, will be discussed in the "Flight control algorithms" chapter.

Finally, it is important to calculate the longitudinal stability derivative, for which $C_m(\alpha, x_s)$ function has been rewritten as a function of only α, using the relationship of $x_s(\alpha)$.

$$C_m = \left(0.4796 \cdot \left(\frac{0.1963\alpha - 0.1814}{0.4796\alpha - 0.3846}\right) - 0.1963\right) \boldsymbol{\alpha} - 0.3846 \cdot \left(\frac{0.1963\alpha - 0.1814}{0.4796\alpha - 0.3846}\right) + 0.1814 \tag{2.132}$$

Now it is possible to calculate the pitching moment derivative regarding the angle of attack:

$$\frac{dC_m}{d\alpha} = \frac{0.1963\alpha^2 - 0.1963\left(\alpha - 0.8019\right)^2 - 0.3147\alpha + 0.1262}{\left(\alpha - 0.8019\right)^2} \tag{2.133}$$

The previous equation plot is illustrated below. As it can be observed, it always has a negative value, which is the main requirement for stability:

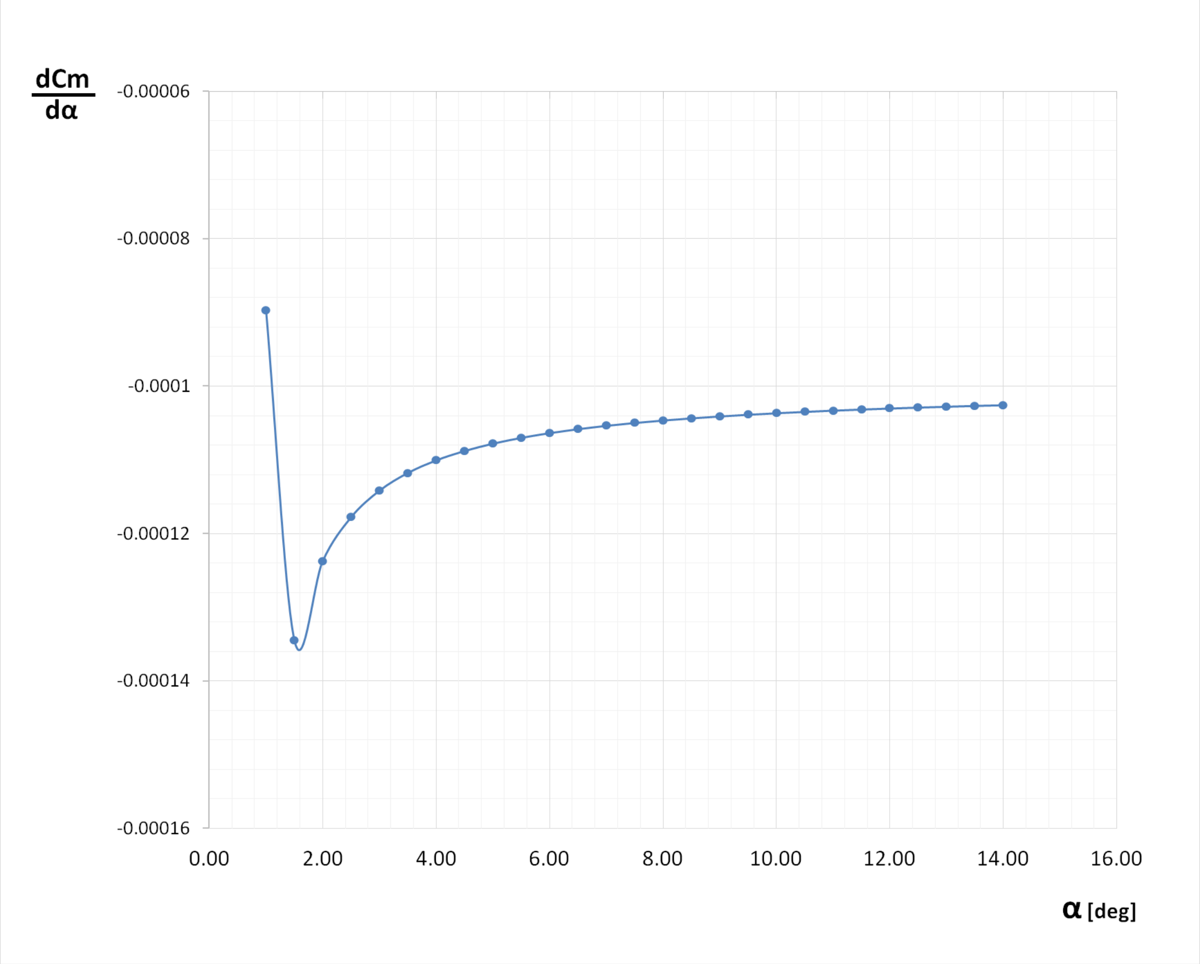

Figure 2.121: Longitudinal stability derivative versus angle of attack

2.4.20.2 Static Lateral Stability and Control

In the previous chapter the rolling moment equation was obtained.

$$\Delta L\big|_{Y_{CG}=y_s} = \frac{\rho S u_\infty^2}{2b}(4.76\alpha + 0.0189) \cdot 1.2856 y_s \tag{2.134}$$

Analyzing the rolling moment equation it is possible to confirm that in real flight situation the aircraft can not achieve equilibrium of moments for $Y_{CG} \neq 0$. This is due to the fact that there are no ailerons to compensate the lift imbalance. The only way to get a $\Delta L = 0$ for $Y_{CG} \neq 0$ is for a negative α, which is not realistic.

This means that for a turn maneuver on a horizontal plane, the aircraft should increase the bank angle until a certain value and then decrease until equilibrium at $\beta = 0$. During this transition, the aircraft should have completed the required turn, which obviously, can not be considered at a constant bank angle. In the following chapters, the required algorithm will be discussed, which permits to solve numerically the turn maneuver problem for a set of parameters.

2.4.21 Flight Control

2.4.21.1 Flight Control Algorithm

The flight control algorithm which has been implemented in the processing unit is a closed loop control system, where different sensors provide feedback signal of different physical properties and depending on the set point, the control system is actuated displacing the center of gravity over x and y axis. The algorithm should be capable of handling situations of steady cruise flight and sudden gusts (mainly affecting longitudinal dynamic stability), bank angle correction and banked control turns. The simplified diagram illustrates the procedure to calculate required δ_x and δ_y deflections, depending on the current state of the aircraft and the set point. For the X_{CG} position the current angle of attack is the key factor considered to determine the δ_x deflection. As explained before, X_{CG} position changes the slope of the pitching moment coefficient versus alpha.

For the Y_{CG} position, the current bank angle is considered to calculate the required δ_y. Y_{CG} position, obviously, generates an imbalance in the rolling moment, changing asymmetrically the bank angle. Since it is not possible to achieve equilibrium for a bank angle $\beta \neq 0$, it is important to have a controlled banked turn, where the bank angle is not constant, but calculated during each step according to the radius, the current bank angle and the amount of turn angle left to complete the set point angle.

Regarding the thrust control, the motor works at full throttle when sudden gusts increase the angle of attack over α_{stall}. This, naturally, combined with the pitching moment damping decreases the angle of attack trying to reach the set point.

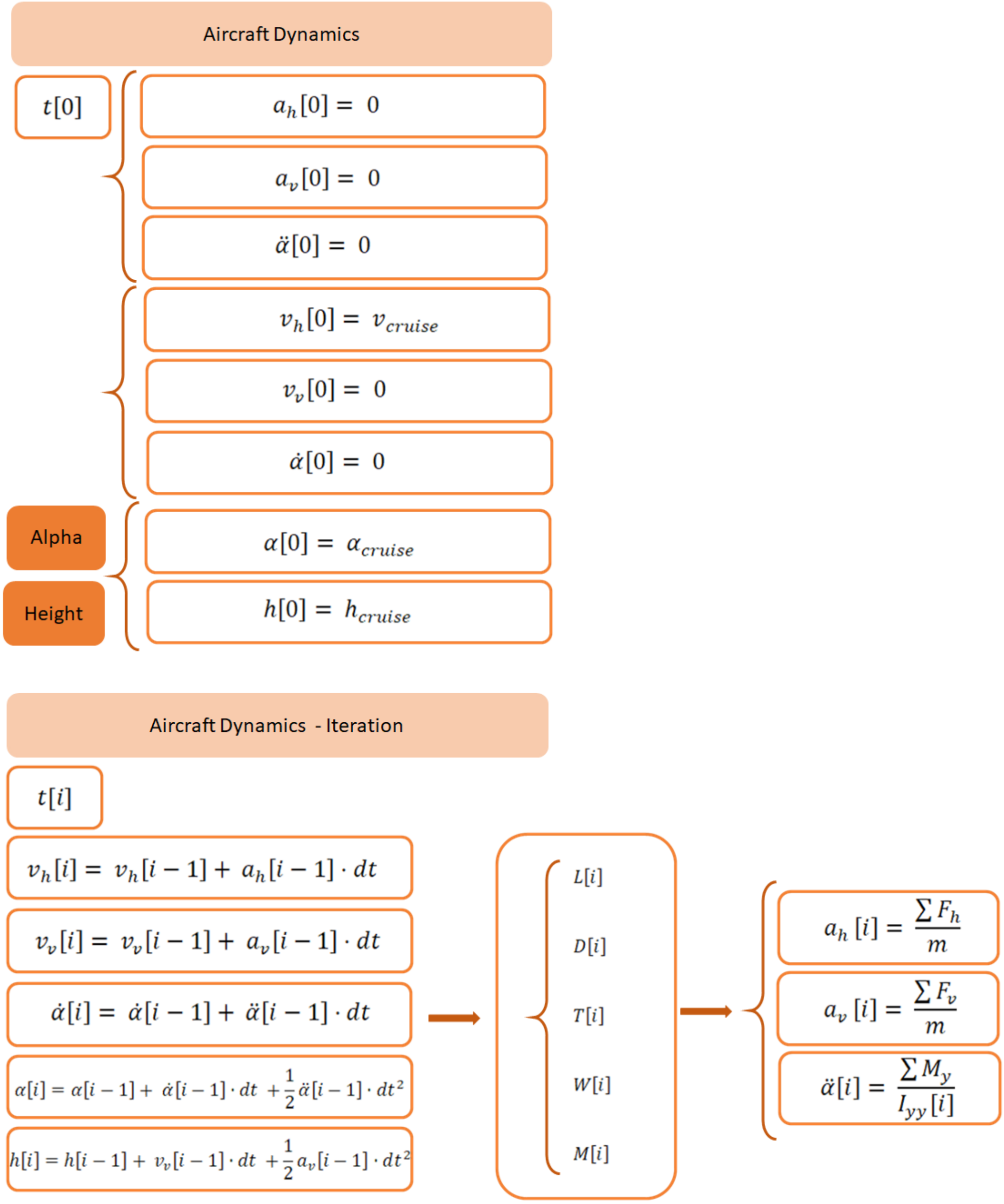

Figure 2.122: Flight Control Algorithm Diagram - initial step and iterable block

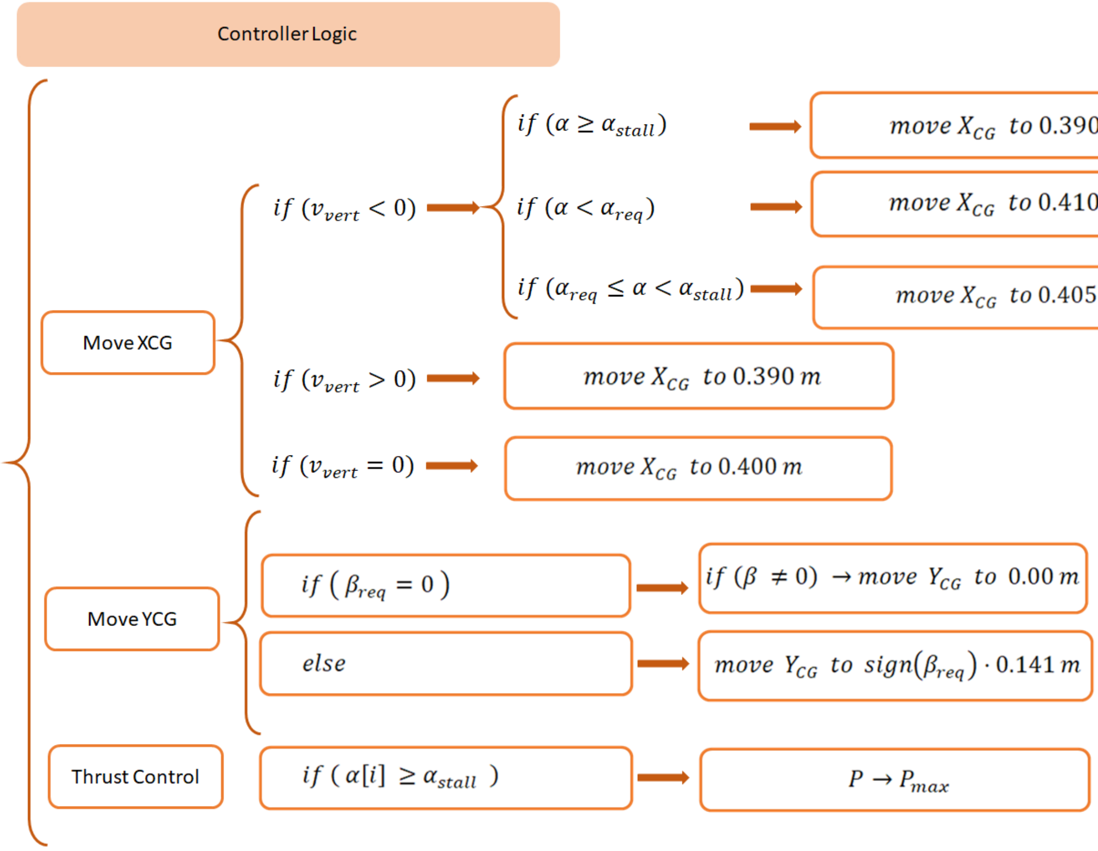

Figure 2.123: Flight Control Algorithm Diagram - recursive block

2.4.21.2 Flight Controller

According to the project requirements, the most adequate flight controller, which is also widely used in the current UAV market, is the ArduPilot Mega (Arduino-Autopilot). One of the main advantage of this controller is the number of input and output ports: 8 of each. Also it has special ports for GNSS, Transmitter and Receiver units. The controller's CPU runs mainly C and C++ programming languages, or adapted Python code. The last language has been chosen for the flight control algorithm development, since Python syntax allows faster code prototyping. However, it is highly recommended to convert the final code to C or C++ for faster execution. This part, however, is out of the project scope, even though it is quite straightforward.

The flight control algorithm described above should be implemented on the ArduPilot. It is important to note that the ArduPilot Mega has an integrated 3-axis Gyro, 3-axis Accelerometer and a high resolution Altimeter. Therefore, no external Inertial Measurement Unit is needed. This gives certain advantages, such as a more compact system, less weight and free input ports, which can be used in the future for upgrades and modifications. The controller also has a 4 MegaByte Dataflash chip for automatic datalogging. ArduPilot specifications can be found in the Technical Sheets Attachment [2], based on the manufacturer's description [33].

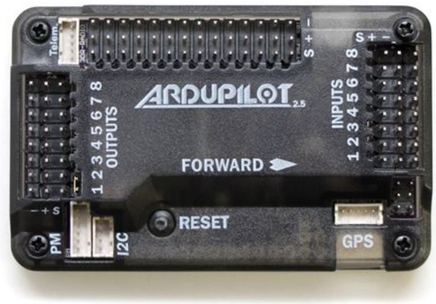

Figure 2.124: ArduPilot Mega 2.8 flight controller [33]

2.4.22 Flight Simulation and Validation: Dynamic Load Cases

2.4.22.1 Dynamic Longitudinal Stability

For the analysis of the dynamic longitudinal stability, a Python script has been written implementing the algorithm mentioned above. First of all, the time domain has been defined, where the time step is set to 0.05 seconds, and the total simulation time to 600 seconds. Other parameters related to the aircraft geometry, aerodynamics (polar curves) and controller functions are defined as well.

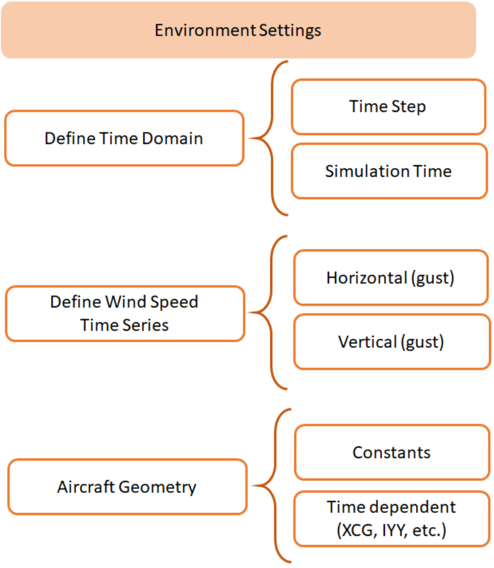

Figure 2.125: Simulation environment settings

Then, two simulations have been done considering vertical wind gusts according to the normative.

2.4.22.2 Vertical moderate gust without reaching stall

According to the Legislative framework, the maximum vertical gust does not exceed $15.74m/s$. Obviously, during a cruise flight at $16m/s$ a sudden vertical gust would increase the angle of attack over the stall angle. For instance, a moderate wind gust has been considered, according to which the vertical wind speed time series has been defined as:

$$w_v(t) = \begin{cases} 0\ m/s, & t < 50s \\ 6.00\ m/s, & 50s \leq t \leq 120s \\ 0\ m/s, & t > 120s \end{cases}$$

The next figures illustrate flight altitude, angle of attack and center of gravity on x-axis position evolution over time.

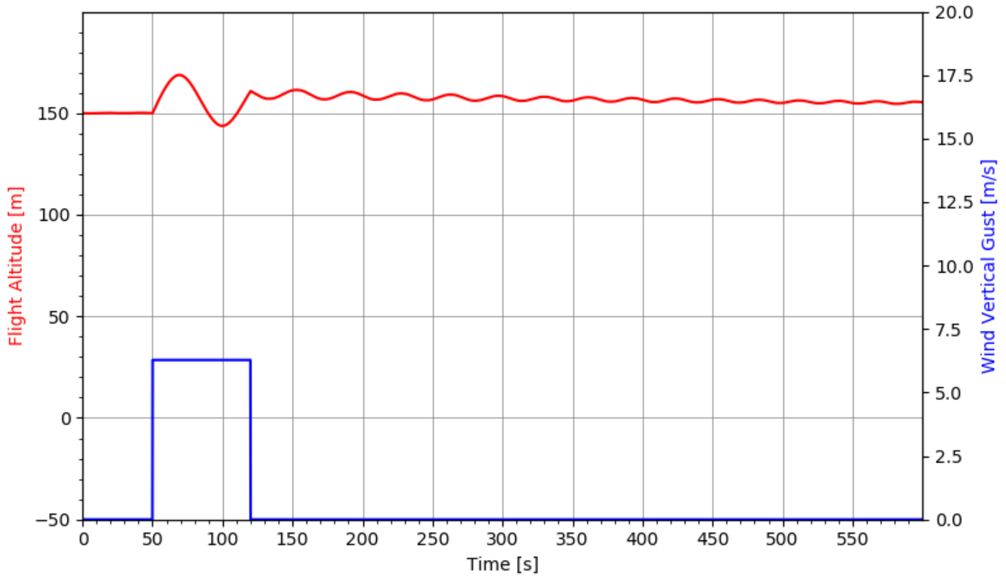

Figure 2.126: Moderate wind gust: flight altitude over time.

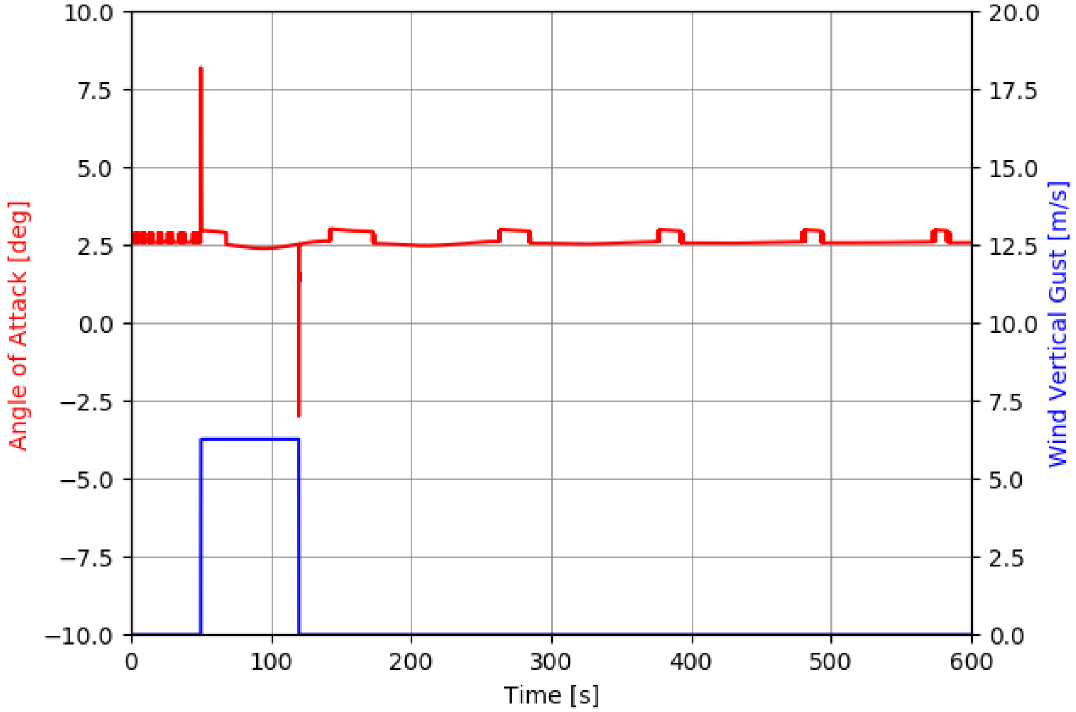

Figure 2.127: Moderate wind gust: angle of attack over time.

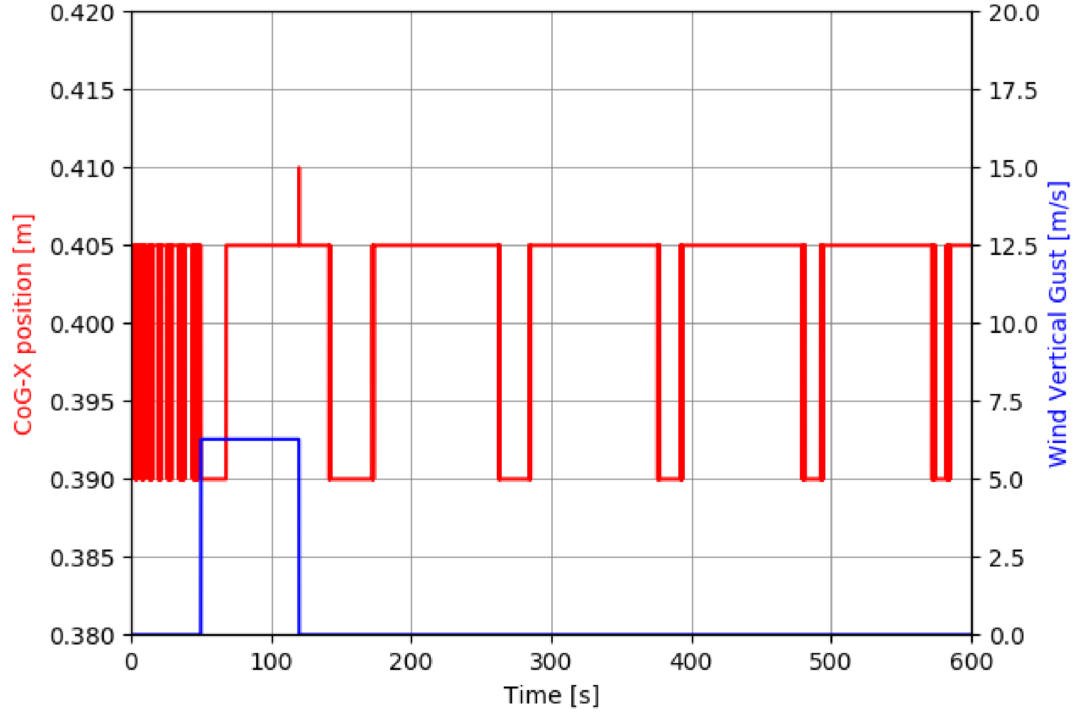

Figure 2.128: Moderate wind gust: center of gravity position on x-axis over time.

From the altitude time series it is possible to observe that the sudden wind gust increases the angle of attack (without over-passing stall angle), increasing Lift to Weight ratio. Therefore, the aircraft starts to climb, while the pitching moment keeps reducing the angle of attack. The controller, at the same time, moves the center of gravity position towards the nose in order to increase the pitching moment versus alpha slope. After leaving the wind gust zone, the aircraft stabilizes at a certain height, and there is a small, damped oscillation.

From the angle of attack versus time plot it is possible to observe the sudden increase of the angle of attack and the drastic response due to the pitching moment, reducing it. Also, at the end of the wind gust, there is a sudden decrement of the alpha (since the vertical wind gust disappears). However, the controller moves X_{CG} towards the trailing edge (0.410 m), where the pitching moment versus alpha has a positive slope, and the angle of attack starts increasing.

There is some minor oscillation after the wind gust, which has a minor impact in height, angle of attack and center of gravity. However, this behavior can be tuned with more advanced controller logic.

2.4.22.3 Vertical strong gust with stall

After the first successful simulation where stall was not reached, it was important to check the aircraft stability during a stronger wind gust. Therefore, the objective of the following analysis was to see the aircraft performance during the maximum wind gust according to the normative, and to check if the flight controller implementation has been correctly set up.

The wind vertical speed has been defined as:

$$w_v(t) = \begin{cases} 0\ m/s, & t < 50s \\ 15.74\ m/s, & 50s \leq t \leq 120s \\ 0\ m/s, & t > 120s \end{cases}$$

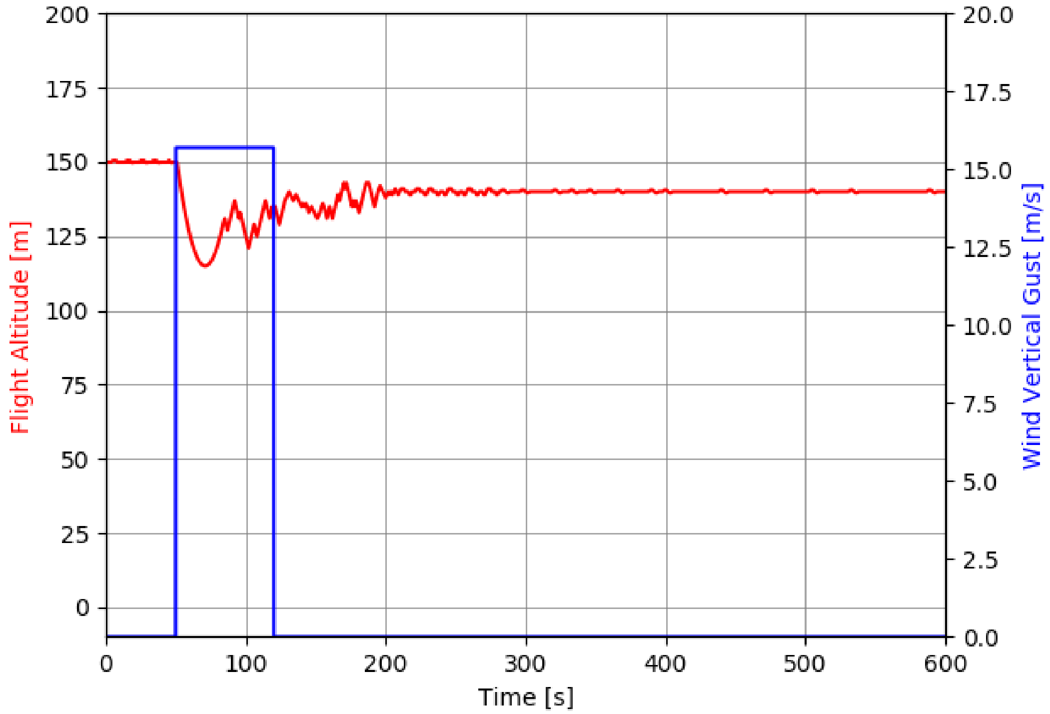

Figure 2.129: Strong wind gust: flight altitude over time.

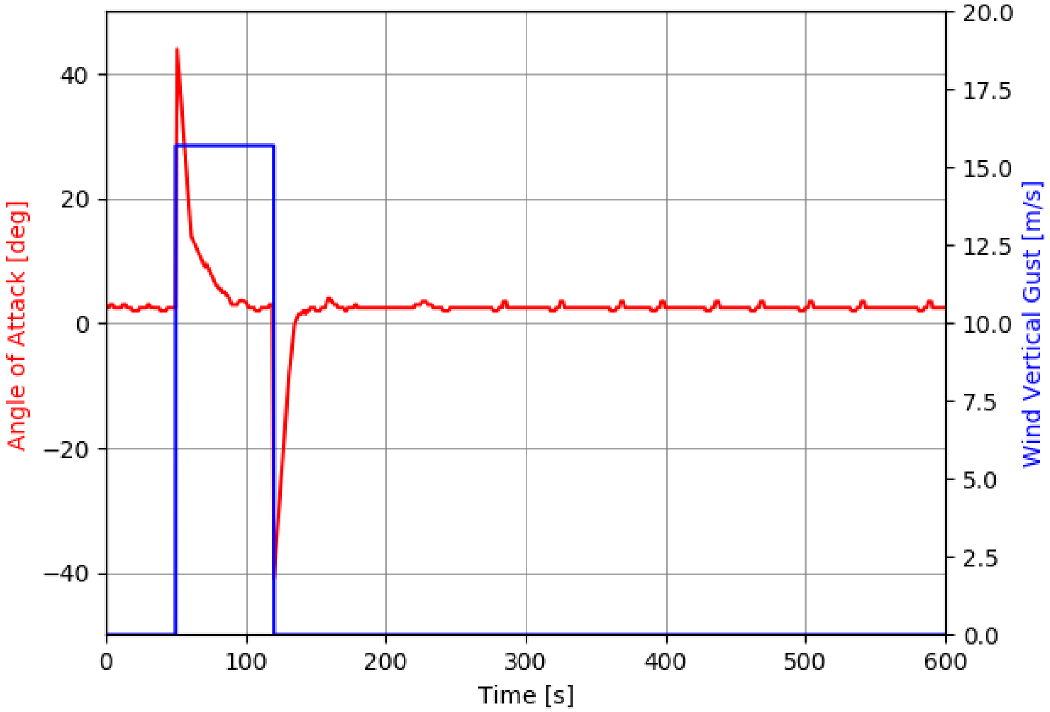

Figure 2.130: Strong wind gust: angle of attack over time.

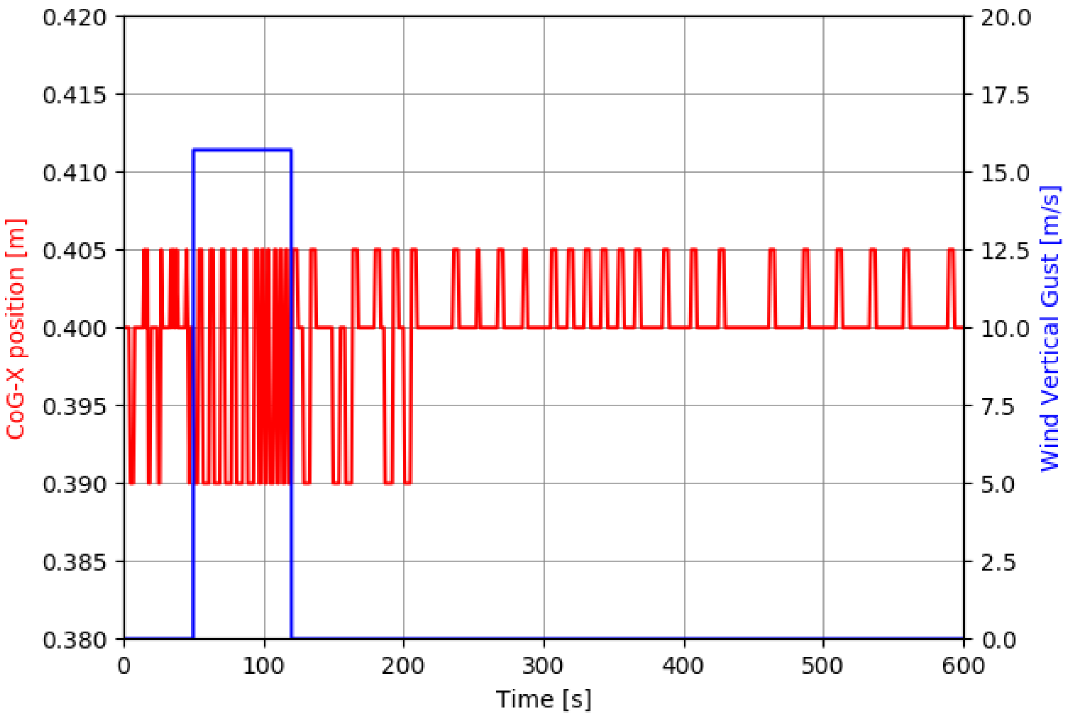

Figure 2.131: Strong wind gust: center of gravity position on x-axis over time.

- From the angle of attack time series it is possible to observe that the wind gust suddenly increases the angle of attack to a very high, 44.4°. Immediately, the pitching moment damping reduces the angle of attack, combined with the controller actuation, moving X_{CG} from 0.40 m to 0.39 m. Therefore, the pitching moment coefficient versus angle of attack slope is decreased, accelerating the recovery of the angle of attack to the set point angle. At some point the gust disappears and the angle of attack drops significantly. Therefore, X_{CG} is pushed backwards, getting into an unstable pitching moment versus angle of attack condition, which is intended. The goal is to increase the angle of attack until the cruise angle is reached, and then move X_{CG} to 0.40 m (stable position).

- Regarding the flight altitude, it drops significantly during the first 5 seconds, since the aircraft is in stall. However, when the aircraft reaches operable range of angle of attack, lift to weight ratio increases significantly and the aircraft starts climbing. After exiting wind gust zone, the aircraft reaches steady flight condition at a certain height, with minor transitory oscillations.

.

Summary of Results

3.1 Economic Study

As part of the economic study, the cost of different parts of the project have been calculated, and potential markets have been analyzed.

3.1.1 Project Development Cost

The cost of the project development has been calculated considering an average salary per hour equal to 25 €/H, and a total of 715 work hours. The average salary has been determined based on the tasks involved during the development of the project. Therefore, the estimated project development cost is around 17875 €.

3.1.2 Market Study: Potential Markets and Competitor

Fixed wing, small and medium scale unmanned aerial vehicles' versatility creates a competitive market for professional and recreational uses. Some of the most demanded uses include search and rescue, mapping, landscape scanning, fire fighting zone scanning, surveillance, cargo transportation in trouble zones, scientific research, etc. Fixed wing drones provide relatively high autonomy and moderate flight speed. This enables to scan larger areas optimally.

On the other hand, multi-rotor, and specially quad-rotor drones are quite popular nowadays. Their application, however, is limited by the relatively small autonomy, although their importance has grown due to their high quality shooting and precision. This market, however, is going to be discarded.

Since the payload enables the possibility to incorporate a thermal sensor or a high definition camera, the main market the project will be targeting will be the one for mapping, landscape scanning and surveillance.

A brief research regarding these markets has been done, and a list of competitors has been created. The information obtained from each manufacturer's Sales department is summarized in the following table.

Characteristics	**FeiYu X8**	**Conyca Geodrone**	**C-Astral Atlas**	**Eleron 3SV**	**Eleron 10SV**
Wingspan [m]	2.12	1.55	1.55	1.47	2.2
MTOW [kg]	5.0	2.0	2.0	5.5	15.5
PL [kg]	0.6	0.5	0.3	ND	2.5
Cruise Speed [m/s]	65	72	58	70	75
Endurance [h]	0.6	1.0	1.0-1.2	1.6	2.5
Approximate price [EUR] (without optical sensor)	7,500	20,000	22,500	18,000	28,000

Table 3.1: Characteristics and approximate price of competitors

3.1.3 Business Plan

As part of the Business Plan, the fabrication costs and the final price have been estimated, and also a lost pf post-sell services has been determined.

3.1.3.1 Fabrication Costs

In this chapter the fabrication cost will be calculated. It is important to note that the goal is to estimate a competitive price to begin with. Therefore, the analysis is done superficially, and the fabrication cost is just an approximation. The process is divided into three groups, where the corresponding costs have been calculated.

- The total price of required electronic components and systems has been estimated to be around **€2,879.00**.
- The total cost of required materials according to the structural design has been estimated to be around **€135.00**.
- The main manufacturing processes involved in the structural construction consist in: The required machinery and fabrication cost is estimated to be of the 30 % of the total cost.

Therefore, the total fabrication cost per unit can be considered around **€4,306.00**.

An additional 20 % has been considered for Marketing, making total unitary cost equal to **€5,167.00**.

3.1.3.2 Post-Sell Services

One of the most important goals is to create in the market a technologically advanced and reliable brand. For this reason, it is important to supply high quality products as well as post-sell services. This, additionally, can provide a decent income over the years, and also create a trustworthy customer-brand relationship. The post-sell services can be divided into three groups:

- **Maintenance:** it would include regular inspection and repairing services, as well as some parts substitution, if required and depending on the warranty policy. Depending on the further development of the project, there can be different options of maintenance. One option would be to offer a fixed-price per service, if out of warranty. Another option would be to have a annual plan which covers any kind of maintenance services within a year.
- **Upgrades:** it is important to constantly provide upgrades, both, for the flight control software and on-board hardware, if required. The first one could be done by the customer, and free of cost. The hardware upgrades would be adapted to customers' needs.
- **Optional sensors:** Additionally, it is important to offer a variety of thermal sensors and high definition cameras, and constantly update the compatible components list, in order to match existing and future customers' needs.

3.1.3.3 Price

Based on the previous analysis regarding the potential markets, competitors and fabrication cost, a competitive price has been calculated.

- The average price of similar unmanned systems oscillates around €20,000.00.
- The estimated fabrication cost is around €5,167.00 per unit.
- A profit margin of 50% has been considered.
- The project development cost has been considered to be amortized over time and covered by the profit margin. This approach helps to keep a competitive price.

Finally, the starting price is set to **€10,000.00** per unit.

It is important to note, that for the further development of the project it would be necessary to analyze inversion and manufacturing costs in more detail, which would result in a complete Economic Evaluation.

3.2 Environmental Impact

Based on a global analysis of the project, it is safe to say that the environmental impact is positive. Main reasons for such a statement are:

- Fully electrical vehicle, with rechargeable batteries, which means zero emission. Following the provided best-practices guide, the selected batteries will have long lifespan.
- Robust model. The elimination of external movable parts improves the structural integrity, and raises the life-span of structural elements such as ribs and spars. These means less replacements over time.

3.3 Conclusions and recommendations

This project aimed to study the viability of an unmanned aerial vehicle without ailerons, elevators and vertical stabilizer, and to identify if a mass-actuated control system can offer the desired stability and control. Based on the project results it can be concluded that such a solution is possible and viable.

To get into this point different branches of Aerospace Engineering have been touched, including Aerodynamics, Structures, Propulsion, Avionics and Flight Mechanics. It is important to note that the aircraft plan-form and airfoil distribution have had considerable contribution on the achievement of the necessary pitching moment versus angle of attack behavior, which raises the overall efficiency since the geometric twist is small. From the structural point of view, advanced computer aided design and analytical calculations combined with simulations provided a robust model, while being compatible with the movable mass system implementation. Regarding the propulsion system, a complete analysis helped to identify the most suitable brushless motor and propeller combination, as well as the most adequate battery, according to capacity and desired autonomy. Systems design concluded with a list of essential components for safe and controllable flight, with specifications provided by the corresponding manufacturers.

More emphasis has been done on flight mechanics and control system design, where accurate relationships have been obtained regarding the center of gravity variation, inertia tensor variation, control derivatives and their relationship to stability derivatives.

Furthermore, simulation results for dynamic cases provided expected time series regarding flight altitude and angle of attack, which has been considered adequate for the validation of the flight control algorithm. Additionally, a brief analysis regarding economic aspects was concluded with an estimated initial and competitive price of the product. Market study and fabrication costs calculation have been done, and a list of post-sell services has also been provided.

Throughout the development of the project some difficulties have been found and solved. The methodology of combining analytical calculations with numerical simulations has been the key, specially for Aerodynamics and Structures, to achieve the desired results. Some of the most important contributions of this project can be considered the fact that an innovative solution for the control system is viable, and it offer simplicity and advantages, such as structural integrity, robustness and efficiency, contrasted with what traditional aerodynamic control surfaces offer.

For scalability of the proposed solution and application to heavier unmanned aerial systems additional topics should be studied, such as directional control and stability. This topic was out of the scope of the project, however, a possible solution for further development would be to have twin motors (on wings) and use differential thrust to generate a yawing moment.

For further development it is highly recommended to focus on the validation of the aerodynamic model by a design of experiments, and thereof, improve the physical model of the vehicle dynamics. Additionally, it is recommended to focus on building a Simulink model, to launch multiple simulations, to calibrate and improve the control system and flight algorithms.

3.4 Further development proposal

A brief list of tasks is proposed for further in-depth development of the solution.

- Regarding Aerodynamics: a prototype could be built to be tested in a wind tunnel. This could improve the aerodynamic model and provide a better approximation of the vehicle dynamics.
- Regarding Performance and Flight Control: an advanced Simulink model could be created (with improved aerodynamic data), to simulate the model for diverse scenarios. Additional flight tests could improve calibration and help to adjust stability derivative functions which are implemented in the control loop.
- Regarding Systems: user experience could be improved developing a graphical user interface for the remote control device. Additionally, in-depth analysis of the state of the art could help to replace some components and reduce costs.
- Regarding Computational design: enhanced manufacturing-ready blueprints could be provided with tolerance analysis.

3.5 Normative

For the development of the project European Aviation Safety Agency guidelines have been followed. Due to the lack of a final normative, two proposed drafts have been studied, such as the “Notice of Proposed Amendment 2017-05 (A)” and the“Notice of Proposed Amendment 2017-05 (B)”[12]. For design criteria and technical aspects, CS-VLA (Very Light Airplanes)[12] and CS-23 (Normal, Utility, Aerobatic and Commuter Airplanes)[12] have been analyzed and followed, as explained previously.

Bibliography

[1] Report Attachment *Design of an Unmanned Aerial Vehicle with a Mass-Actuated Control System*

[2] Technical Sheets *Design of an Unmanned Aerial Vehicle with a Mass-Actuated Control System*

[3] Nickel, K., Wohlfahrt, M. *Tailless Aircraft in Theory and Practice,* Amer Inst of Aeronautics, (September 1, 1994), AIAA Education Series, Book

[4] Guglielmo, J., Selig, M. *Spanwise Variations in Profile Drag for Airfoils at Low Reynolds Numbers,* University of Illinois at Urbana-Champaign, (July-August, 1996), Journal of Aircraft, Vol. 33, No. 4,

[5] Ira Abbott, H., Albert Von Doenhoff, E. *Theory of wing sections,* Dover Publications, Inc. New York, (1959), Dover, Book

[6] V. I. Feodosiev. *Resistencia de materiales* Mir Publishers, Moscow, (1980), Book

[7] Stephen P. Timoshenko and James M.Gere. *Theory of Elastic Stability,* Dover Publications, New York, (2009), Book

[8] E. F. Bruhn. *Analysis and Design of Flight Vehicle Structures,* Jacobs Publications, USA, (1973), Book

[9] Leishman, J. Gordon. *Principles of Helicopter Aerodynamics* Cambridge Cambridge Aerospace Series, 2000 Book

[10] Sebastin, Franchini; scar, Lpez Garcia. *Introduccin a la Ingeniera Aeroespacial* Madrid Editorial Garceta, 2012 Book

[11] Miguel Ángel, Gómez Tierno; Manuel, Pérez Cortés; César, Puentes Márquez. *Mecánica del vuelo* Madrid Editorial Garceta, 2012 Book

[12] European Aviation Safety Agency *EASA,* European Union 2018, Organization Official Website. Retrieved from https://www.easa.europa.eu

[13] Airfoil Tools. *Airfoil database,* 2018, Online Airfoil Database
Retrieved from http://airfoiltools.com

[14] Aerodynamics Tools. *Aerodynamics database and Tools,* 2018, Online Aerodynamics Database and Tools
Retrieved from https://www.mh-aerotools.de/airfoils/

[15] Wikipedia. *Aircraft principal axis,* 2019, Aircraft principal axis figure source
Retrieved from https://en.wikipedia.org/wiki/Aircraft_principal_axes/

[16] UIUC Airfoil Data Site. *Airfoil database,* UIUC Applied Aerodynamics Group 2018, University of Illinois at Urbana-Champaign, Dept of Aerospace Engineering
Retrieved from https://m-selig.ae.illinois.edu/

[17] Nostromo, LLC. *Nostromo-Group,* Spacir Designs 2018, Manufacturer's Official Website.
Retrieved from http://nostromo-group.com/product-sets/uav-engineering-products/

[18] Ministry of Defense of Republic of Armenia. *Engineering Department,* 2018, Official Website.
Retrieved from http://www.mil.am/en

[19] Aeronautics. *Aeronautics-Systems,* AERONAUTICS 2015, Manufacturer's Official Website. Retrieved from
https://aeronautics-sys.com/home-page/page-systems/page-systems-orbiter-2-mini-uas/

[20] C-Astral d.o.o. *C-Astral,* C-Astral 2017, Manufacturer's Official Website.
Retrieved from http://www.c-astral.com/

[21] Conyca S.L. *Conyca,* Geomax Espaa 2018, Manufacturer's Official Website.
Retrieved from http://www.conyca.es/

[22] Primoco UAV SE. *Primoco UAV - Unmanned Aerial Vehicles and Systems,* 2018, Manufacturer's Official Website.
Retrieved from http://uav-stol.com/

[23] Enics UAV JSC. *Unmanned Aerial Vehicles, Target Systems,* ACTIX studio 2018, Manufacturer's Official Website.
Retrieved from http://www.enics.ru/

[24] Leonardo SPA. *Leonardo - Aerospace, Defence and Security,* Leonardo 2018, Manufacturer's Official Website.
Retrieved from http://www.leonardocompany.com/en/-/falco

[25] Military Technical Institute. *Military Technical Institute, Belgrad,* 2018, Manufacturer's Official Website.
Retrieved from http://www.vti.mod.gov.rs

[26] FeiyuTech. *FeiyuTech,* 2018, Manufacturer's Official Website.
Retrieved from http://www.feiyu-tech.com/uav/

[27] Toray Industries, INC. *Toray,* Japan 2018, Manufacturer's Official Website.
Retrieved from https://www.toray.com/

[28] ASM Aerospace Specification Metals, Inc. *Mars Parachutes,* US 2018, Manufacturer's Official Website.
Retrieved from http://www.aerospacemetals.com/contact-aerospace-metals.html

[29] MonoKote *MonoKote* 2018, Manufacturer's Patent.
Retrieved from http://www.freepatentsonline.com/3388651.pdf
and from http://www.monokote.com/

[30] APC Propellers *APC,* 2018, Technical Data sheet from the manufacturer's Official Website.
Retrieved from https://www.apcprop.com/files/PER3_16x10E.dat

[31] Eli Airborne Solutions *Eli Estonia,* 2019, Manufacturer's Official Website.
Retrieved from http://www.uav.ee/

[32] Hacker Motor GmbH *Hacker Motor,* 2019, Manufacturer's Official Website.
Retrieved from https://www.hacker-motor-shop.com/

[33] ArduPilot *ArduPilot Developer,* 2019, Manufacturer's Official Website.
Retrieved from http://ardupilot.org/

[34] Matek Systems *Matek Systems,* 2019, Manufacturer's Official Website.
Retrieved from http://www.mateksys.com/

[35] FlySky RC *FlySky Systems,* 2019, Manufacturer's Official Website.
Retrieved from http://www.flyskyrc.com/

[36] Advanced Microwave Products *Advanced Microwave Products* 2019, Manufacturer's Official Website.
Retrieved from https://www.advmw.com/

[37] Sony Corporation *Sony* 2019, Manufacturer's Official Website.
Retrieved from https://www.sony.com/

[38] Panasonic *Panasonic* 2019, Manufacturer's Official Website.
Retrieved from https://www.panasonic.com

[39] Hitachi Ltd. *Hitachi* 2019, Manufacturer's Official Website.
Retrieved from https://www.hitachi.com/

[40] Flir Systems Inc. *Flir* 2019, Manufacturer's Official Website.
Retrieved from https://www.flir.com/

[41] Leonardo DRS Inc. *Leonardo DRS* 2019, Manufacturer's Official Website.
Retrieved from http://www.drsinfrared.com/Home.aspx

[42] North American Survival Systems *NA Survival Systems* 2019, Manufacturer's Official Website. Retrieved from https://northamericansurvivalsystems.com

[43] L3 Technologies Inc. *L3 Warrior Sensor Systems* 2019, Manufacturer's Official Website.
Retrieved from http://www.l3warriorsystems.com/ nanocore